University of Calgary

PRISM Repository **https://prism.ucalgary.ca**

The Vault Open Theses and Dissertations

2016-01-15

Brain Development During Childhood and Adolescence

Mah, Alyssa

Mah, A. (2016). Brain Development During Childhood and Adolescence (Master's thesis, University of Calgary, Calgary, Canada). Retrieved from https://prism.ucalgary.ca. doi:10.11575/PRISM/25160 http://hdl.handle.net/11023/2748

Downloaded from PRISM Repository, University of Calgary

UNIVERSITY OF CALGARY

Brain Development During Childhood and Adolescence

by

Alyssa Mah

A THESIS

SUBMITTED TO THE FACULTY OF GRADUATE STUDIES

IN PARTIAL FULFILMENT OF THE REQUIREMENTS FOR THE

DEGREE OF MASTER OF SCIENCE

GRADUATE PROGRAM IN BIOMEDICAL ENGINEERING

CALGARY, ALBERTA

January, 2016

© ALYSSA MAH 2016

Abstract

Brain development is a combination of complex physiological changes, and various magnetic resonance imaging (MRI) techniques can help explain observed changes during development *in vivo*. Building upon observations from post-mortem studies, advancements in imaging and modelling techniques provide new means to further interpret the understanding of healthy brain development during childhood and adolescence. It is, however, a challenge to capture specific physiological changes, such as myelination, using MRI. This thesis uses MRI techniques – neurite orientation dispersion and density imaging (NODDI), inhomogenous magnetization transfer (ihMT), and multi-component driven equilibrium single pulse observation of T1 and T2 (mcDESPOT) – that further characterize development in white and subcortical grey matter regions in the brain by improving specificity of the MRI signal compared to conventional techniques. Measures from NODDI, ihMT, and mcDESPOT suggest an increase in myelination and/or axonal packing during development from 0-13 years.

Acknowledgements

First and foremost, I would like to thank my supervisor, Dr. Catherine Lebel, for her guidance and support throughout my time as a graduate student.

I am thankful for current and former students, post-docs, and scientists at the University of Calgary (Mark Krongold, Estee Lee, Manu Schuetze) and members of the Child and Adolescent Imaging Research Program (CAIR) for their contributions to my project, providing mentorship, and friendly support.

I am thankful for the study period I spent at University of Colorado Denver and Brown University. Special thanks to my study exchange supervisor, Dr. Sean Deoni, and his team members that welcomed me to their lab spaces.

My project was made possible with the funding provided by the National Sciences and Engineering Research Council of Canada (NSERC), the Faculty of Graduate Studies and the Biomedical Engineering Graduate Program (University of Calgary).

Lastly, I would like to thank my family and friends for their continued support.

Table of Contents

Abstract ii
Acknowledgements iii
Table of Contents iv
List of Tables vii
List of Figures and Illustrations viii
List of Symbols, Abbreviations and Nomenclature x

CHAPTER ONE: INTRODUCTION 1
1.1 Introduction 1
1.2 Hypotheses 3
1.3 Objective 3
1.4 Overview of thesis structure 3
1.5 Subject information 4

CHAPTER TWO: BACKGROUND MATERIAL AND LITERATURE REVIEW 6
2.1 White and grey matter microstructure 6
2.2 MRI background 8
2.2.1 History 8
2.2.2 Nuclear magnetization 9
2.2.3 Net magnetization 9
2.2.4 Main Magnetic Field 10
2.2.5 MR Signal 10
2.2.6 RF Energy 10
2.2.7 Bloch equation 11
2.3 T1-weighted imaging 12
2.4 Diffusion imaging 13
2.5 Magnetization transfer imaging 16
2.6 Inhomogeneous magnetization transfer imaging 18
2.7 Multi-component analyses 18
2.7.1 NODDI 19
2.7.2 mcDESPOT 20
2.8 Susceptibility-weighted imaging 22
2.9 Quantitative susceptibility mapping 23
2.10 Image registration 23
2.11 Study rationale 24

CHAPTER THREE: CHILDHOOD AND ADOLESCENCE DEVELOPMENT USING NODDI 25
3.1 Introduction 25
3.2 Methods 28
3.2.1 Subject demographics 28
3.2.2 MRI Acquisition 29
3.2.3 Image analysis 29
3.2.4 Registration 30
3.2.5 Regions of interest 30

3.2.6 K-means clustering 31
3.3 Results 32
3.3.1 Changes with age 32
3.3.2 K-means clustering 38
3.4 Discussion 44

CHAPTER FOUR: DEVELOPMENTAL CHANGES BETWEEN PRESCHOOL CHILDREN AND ADOLESCENTS USING IHMT 51
4.1 Introduction 51
4.2 Methods 53
4.2.1 Subjects 53
4.2.2 MRI acquisition 54
4.2.3 Image analysis 55
4.2.4 Regions-of-interest 56
4.2.5 Registration 58
4.3 Results 58
4.3.1 Age analysis 62
4.4 Discussion 63
4.4.1 Group differences 63
4.4.2 Age analysis 64
4.4.3 Limitations 65
4.5 Conclusion 65

CHAPTER FIVE: MYELIN WATER FRACTION AND G-RATIO MEASUREMENTS DURING BRAIN DEVELOPMENT 66
5.1 Introduction 66
5.2 Methods 68
5.2.1 Subject demographics 68
5.2.2 MRI acquisition 68
5.2.3 Image analysis 70
5.3 Results 72
5.4 Discussion 77
5.5 Conclusion 79

CHAPTER SIX: FUTURE DIRECTIONS AND SUMMARY 80
6.1 Future directions 80
6.2 QSM preliminary data 83
6.2.1 Introduction 83
6.2.2 Methods 85
6.2.3 Results 87
6.2.4 Discussion 89
6.3 Thesis summary 90

REFERENCES 92

APPENDIX A: COPYRIGHT PERMISSIONS 103

APPENDIX B: RESULTS FROM MD, AD AND RD.....107
APPENDIX C: RESULTS FROM QMT AND QIHMT.....112
APPENDIX D: BROWN MRI ACQUISITION PARAMETERS.....114

List of Tables

Table 1. Subject demographics used throughout this thesis. 5

Table 2. Subject demographics of the 8 to 13 year old subjects throughout this thesis. 5

Table 3. Linear fitting results of NDI (neurite density) vs. age. The p-values were corrected for multiple comparisons using the false discovery rate method. 37

Table 4. Linear fitting results of FA (fractional anisotropy) vs. age. The p-values were corrected for multiple comparisons using the false discovery rate method. 37

Table 5. Means of NDI-slope and ODI in each cluster from k-means clustering for k=4. 40

Table 6. Means of NDI-slope and ODI in each cluster from k-means clustering for k=6. 40

Table 7. Means of NDI-slope in each cluster from k-means clustering for k=4. 40

Table 8. Means of ODI-mean in each cluster from k-means clustering for k=4. 40

Table 9. Percent differences in qMT and qihMT in each grey and white matter region. Asterisks indicate $p<0.05$ from t-tests. The differences were calculated as the difference divided by the measure in the young cohort (Equation 12). 62

Table 10. R^2 and p values from each MWF linear fit in white matter regions after linearization and adjustment using a mixed-effects model for sites. Fits before the data was adjusted were also significant ($p < 0.001$). CC = corpus callosum 76

Table 11. R^2 and p values from each g-ratio linear fit in white matter regions after linearization and adjustment using a mixed-effects model for sites. Fits before the data was adjusted were also significant ($p < 0.001$). CC = corpus callosum 76

Table 12. List of sub-tests in WASI-II, WIAT-III, and NEPSI-II that compose the full cognitive assessment. 83

Table 13. Fitting results of linear fits for susceptibility. The p-values were corrected for multiple comparisons using the false discovery rate method. 89

Table 14. Linear fitting results of MD (mean diffusivity) vs. age. The p-values were corrected for multiple comparisons using the false discovery rate method. 110

Table 15. Linear fitting results of RD (radial diffusivity) vs. age. The p-values were corrected for multiple comparisons using the false discovery rate method. 110

Table 16. Linear fitting results of AD (axial diffusivity) vs. age. The p-values were corrected for multiple comparisons using the false discovery rate method. 111

List of Figures and Illustrations

Figure 1. Ellipsoid characterized by 3 eigenvectors. 14

Figure 2. The absorption lines of macromolecular and liquid pools. The macromolecular pool has a broader lineshape; it can be saturated with an off-resonance RF pulse. Reprinted with permission from John Wiley and Sons (Henkelman, Stanisz et al. 2001) (Fig 1b). Copyright permissions are in Appendix A. 17

Figure 3. The components of red voxel (on the left) may contain multiple anatomical regions. The 3-pool model (on the right) contains intra/extra cellular, myelin-bound, and free water compartments. Exchange is shown between the intra/extra cellular and myelin-bound water compartments. Figure is reprinted under the Creative Commons Attribution License (CC BY) from (Deoni, Dean et al. 2012) (Fig 1). 21

Figure 4. Neurite density index trajectories in white (A, B) and grey (C) matter volumes-of-interest. Significant lines of fit ($p<0.05$) are plotted on the graphs. 34

Figure 5. Orientation density index trajectories in white (A, B) and grey (C) matter volumes-of-interest. No regressions were signficiant. 35

Figure 6. Fractional anisotropy trajectories in white (A, B) and grey (C) matter volumes-of-interest. Additionally, significant lines of fit ($p<0.05$) are plotted. 36

Figure 7. Within groups sum of squared error as a function of number of clusters. 38

Figure 8. Clusters defined by k-means clustering of NDI and ODI with k=4. 41

Figure 9. Clusters defined by k-means clustering of NDI and ODI with k=6. 42

Figure 10. Clusters defined by k-means clustering of only NDI with k=4. 43

Figure 11. Clusters defined by k-means clustering of only ODI with k=4. 44

Figure 12. Grey matter regions segmented by FreeSurfer. Amygdala (AMYG), caudate (CAUD), hippocampus (HIPP), pallidum (PALL), putamen (PUTA), thalamus (THAL) 57

Figure 13. White matter tracts delineated by FreeSurfer. Anterior thalamic radiation (ATR), cingulum (CG), cortical spinal tract (CST), forceps major & minor (FMAJ, FMIN), inferior longitudinal (ILF), superior longitudinal (SLF), and uncinate fasciculi (UNC) 57

Figure 14. Typical T1-weighted (left), qMT (middle), and qihMT (right) images from a 9-year-old. 59

Figure 15. qMT in grey and white matter regions. Asterisks indicate $p<0.05$ from t-tests. 60

Figure 16. qihMT in grey and white matter regions. Asterisks indicate p<0.05 from t-tests. 61

Figure 17. A, B & C: Myelin water fraction trajectories (using parameters from the linear model after adjustment using a mixed-effects model) in white matter volumes-of-interest determined by MNI152 regions. Logarithmic fits are plotted. A: white matter lobes, B: white matter tracts, C: parts of the corpus callosum (CC) 74

Figure 18. A, B & C: g-ratio trajectories (using parameters from the linear model after adjustment using a mixed-effects model) in white matter volumes-of-interest determined by MNI152 regions. Logarithmic fits are plotted. A: white matter lobes, B: white matter tracts, C: parts of the corpus callosum (CC) 75

Figure 19. Susceptibility trajectories in white (A, B) and grey (C) matter volumes-of-interest. Significant lines of fit ($p < 0.05$) are plotted on the graphs. 88

Figure 20. Mean diffusivity trajectories in white (A, B) and grey (C) matter volumes-of-interest. Significant lines of fit ($p<0.05$) are plotted on the graphs. 107

Figure 21. Radial diffusivity trajectories in white (A, B) and grey (C) matter volumes-of-interest. Significant lines of fit ($p<0.05$) are plotted on the graphs. 108

Figure 22. Axial diffusivity trajectories in white (A, B) and grey (C) matter volumes-of-interest. Significant lines of fit ($p<0.05$) are plotted on the graphs. 109

Figure 23. Mean qMT trajectories in white (A, B) and grey (C) matter volumes-of-interest. No regressions were significant. 112

Figure 24. Mean qihMT trajectories in white (A, B) and grey (C) matter volumes-of-interest. No regressions were significant. 113

List of Symbols, Abbreviations and Nomenclature

Symbol	Definition
ACH	Alberta Children's Hospital
DTI	Diffusion tensor imaging
ihMT	Inhomogeneous magnetization transfer
mcDESPOT	Multi-component driven equilibrium single pulse observation of T1 and T2
MRI	Magnetic resonance imaging
MT	Magnetization transfer
MWF	Myelin water fraction
NODDI	Neurite orientation dispersion and density imaging
QSM	Quantitative susceptibility mapping

Chapter One: **Introduction**

1.1 Introduction

The human brain is a complex organ that is responsible for coordinating sensory inputs, motor outputs, and higher order cognitive and behavioural abilities. Two broad tissue classes of the brain are white and grey matter; white matter facilitates communication within the brain, and grey matter is composed of regions that are involved in sensory perception, muscle control, and mental actions such as learning and memory processing. The characterization of structural growth trajectories during healthy development in white matter connections and grey matter regions can help identify deviations that occur in neurological disorders.

Various magnetic resonance imaging (MRI) techniques, such as T1-weighted imaging, diffusion tensor imaging (DTI), and magnetization transfer (MT) imaging have been used to study healthy white matter and grey matter development during childhood and adolescence (Yoshida et al. 2013, Paus et al. 1999, Leppert et al. 2009). These imaging techniques are, however, sensitive to multiple processes. For example, the signal acquired from these techniques is unable to differentiate the effects of myelination and axonal packing or differentiate between myelin membranes and other membranes/macromolecules.

The human brain has biphasic development from birth to adulthood: rapid and dynamic development in the first five years of life, especially from birth to two years of age (Yoshida

et al. 2013, Leppert et al. 2009), followed by slower, more subtle changes through childhood and adolescence (Deoni et al. 2012). Myelination is an important process that allows for synchronized communication to enable higher order behavioural and cognitive functioning. Disruption in normal myelination can lead to impaired cognitive development. Impairments have been assessed in areas such as fine motor coordination, visuomotor integration, and speeded information processing (Julian et al. 2013). Quantitative measurements of myelin, and white and grey matter microstructure allow for trajectories of healthy regional growth to be established. As brain maturation trajectories can be a sensitive marker of abnormalities (Giedd et al. 2008), the information provided by this research may be useful for early identification of neurological disorders, and evaluation of interventions during treatment and during follow-up. Advancing knowledge of healthy brain changes in children will aid in characterizing structural and functional brain development from birth to adulthood. The analysis tools developed here can be applied to a wider age range in the future and used in other clinical and research applications such as determining the relationship between cognitive abilities and white matter development.

Imaging techniques more specific to myelin, such as myelin water fraction (MWF) imaging, have been used in very young children (Deoni et al. 2011) to show exponential growth in the first two years of life, followed by slower gradual growth. Much more can be added to our understanding in late childhood and adolescence neurodevelopment as there is a lack of studies that focus on this age group.

1.2 Hypotheses

Advanced MRI techniques – specifically neurite orientation dispersion and density imaging (NODDI), inhomogeneous magnetization transfer (ihMT), multi-component driven equilibrium single pulse observation of T1 and T2 (mcDESPOT), and quantitative susceptibility mapping (QSM) – can be used to image and model changes in myelin content and neurite morphology that are able to capture developmental changes in white matter and grey matter. Increases in neurite (axons and dendrites) density, fractional anisotropy, quantitative MT, quantitative qihMT, myelin-water fraction will occur during childhood and adolescence development. Susceptibility will increase in grey matter while susceptibility in white matter will decrease during development. Diffusivity measurements and the g-ratio will decrease during development.

1.3 Objective

The objective is to assess regional trajectories of white matter development delineating regional changes of physiological processes. This will be done by measuring neurite (axons and dendrites) density and orientation, myelination, and macromolecular content using anatomical MRI and DTI, along with NODDI, ihMT, mcDESPOT and QSM.

1.4 Overview of thesis structure

Chapter One contains the introduction of the work presented here. It outlines the motivation, hypothesis, and objective of this research. Chapter Two provides an understanding of the concepts used in the methods and background of the work that has already been established in the field of neurodevelopment relating to MRI. Chapters Three

to Five are broken into distinct foci of work. Chapter Three describes correlations between NODDI parameters and age during childhood and adolescence. Chapter Four explores differences in brain structure between preschoolers and adolescents using ihMT, including material from posters that were presented at the International Society for Magnetic Resonance in Medicine and Organization for Human Brain Mapping in June 2015. Chapter Five contains an analysis of myelin water fraction and g-ratio changes with age during childhood and adolescence. Chapter Six finishes this work with future directions, including preliminary results from QSM changes with age, and overall conclusions.

1.5 Subject information

27 healthy subjects aged 8-13 years were recruited for this study at the Alberta Children's Hospital. Posters and word of mouth were used to recruit subjects. Data from all 27 subjects were all used in Chapter 3. Out of the 27 subjects, 23 subjects were used in Chapter 4, 13 subjects in Chapter 5, and 20 subjects in Chapter 6. Additional data from another study at the Alberta Children's Hospital was used in Chapter 4 (19 subjects, 2-5 years) and from another study at Brown University was used in Chapter 5 (18 subjects, 0-7 years). Demographics of all subjects are shown in Table 1, and demographics of subjects 8-13 year old subjects included in each chapter are shown in Table 2.

Table 1. Subject demographics used throughout this thesis.

	Alberta Children's Hospital		Brown University
Age range	8-13 years	2-5 years	0-7 years
# of subjects	27	19*	18**
Female/male	12/15	8/11	5/13
Mean ± sd	11.3 ± 1.9	3.6 ± 0.5	2.5 ± 2.5

*: used only in Chapter 4

**: used only in Chapter 5

Table 2. Subject demographics of the 8 to 13 year old subjects throughout this thesis.

Alberta Children's Hospital (8 – 13 years)				
Analysis	**NODDI (Ch. 3)**	**ihMT (Ch. 4)**	**MWF & g-ratio (Ch. 5)**	**QSM (Ch. 6)**
# of subjects	27	23	13	20
Female/male	12/15	10/13	4/9	8/12
Mean ± sd	11.3 ± 1.9	11.2 ± 1.9	11.5 ± 1.8	11.3 ± 1.9

Chapter Two: **Background material and literature review**

2.1 White and grey matter microstructure

Structural brain development during childhood and adolescence was initially understood via post-mortem studies that demonstrated brain volume increases (Dekaban 1978), cortical growth and pruning (Landing et al. 2002), and myelination (Benes 1989, Yakovlev and Lecours 1967, Brody et al. 1987). While MRI studies of healthy brain development cannot provide the microscopic detail available by post-mortem methodologies, they are able to study large populations of children longitudinally, and thus have been able to characterize brain and tissue volume changes in detail.

The central nervous system (CNS) allows humans to perceive sensory inputs, control motor movements, and enable cognitive abilities, such as attention and reasoning skills. The CNS consists of the brain and spinal cord that contains neurons. Neurons are cells that receive stimulation from its dendrites resulting in nerve impulses originating from the cell body propagating along the axon and terminating at synapses. The synaptic junctions allow neurons to communicate with each other and muscle or gland cells. White matter mainly includes the bundles of axons that connect separate brain regions enabling communication, and the myelin sheaths surrounding the axons. Characteristics of white matter (such as axon diameter and myelin thickness) affect the speed of transmission along an axon (Aboitiz et al. 1992). Nerve impulses can propagate along axons without myelin, but myelination allows for faster conduction speeds. Myelin is a lamellar structure that consists mostly of lipids, as well as water and proteins. It creates electrical insulation around the

axon that helps facilitate efficient propagation of the signal. Myelin is found primarily in white matter, while smaller amounts are found in grey matter. Grey matter in the brain contains neuron cell bodies, dendrites, and synapses, but mostly contains glial cells, blood vessels, and extracellular matrix; distant regions of grey matter are able to communicate via white matter tracts.

Myelin is visible in the posterior limb of the internal capsule, corona radiata, and cortical spinal tracts by 36 weeks gestational age (Counsell et al. 2002), though newborns have very little myelin overall. As the myelin sheath is formed by oligodendrocytes, the brain experiences dramatic increases in lipid content while total water content decreases in the first year after birth (Holland et al. 1986, Hayakawa et al. 1991). Concurrent development includes increases in cellular and synaptic density, the formation of dendrites, and total brain volumetric growth. However, synaptic density has been observed to increase until the age of 2, and then synaptic pruning follows it thereafter. This is evident by a decline in synaptic density and a slight decline in neuronal density (Peter R 1979). As myelin develops, it progresses across the brain in several patterns very loosely: posterior to anterior (Yakovlev and Lecours 1967), sensory pathways before motor pathways, and projection pathways before association pathways (Kinney et al. 1988). Myelination dramatically increases during infancy and early childhood (Deoni et al. 2012), and then slower, subtler changes follow.

2.2 MRI background

2.2.1 History

The first published paper that laid the foundation for MRI was written by Isidor I. Rabi in *Physical Review* January 31, 1938 (Rabi et al. 1938). In the Letter to the Editor, Rabi introduced a new method to measure nuclear magnetic moments in beams of nuclei passing through magnetic fields. Nuclear magnetic resonance (NMR) is the spectroscopic study of magnetic properties of the nucleus in an atom, and this paper was the first experimental description of NMR that included a description of the apparatus used and the results obtained from directly measuring magnetic moments. Rabi was awarded the Nobel Prize in Physics 1944 "for his resonance method for recording the magnetic properties of atomic nuclei (Nobelprize.org 2013a)."

Further work by two independent researchers, Felix Bloch and Edward Purcell, demonstrated measurement of NMR in solids and liquids. Bloch and Purcell were jointly awarded the Nobel Prize in Physics 1952 "for their development of new methods of nuclear magnetic precision measurements and discoveries in connection therewith (Nobelprize.org 2013b)."

From the 1940s and onwards, NMR was used as an analytic tool for chemistry and biochemistry work. It was not until the 1970s when it was discovered that signals could be localized to produce images based on the magnetic properties of protons by using linear gradient fields. Paul Lauterbur reported the first MR image in 1973 (Lauterbur 1973), and

he later received the Nobel Prize in Physiology or Medicine 2003 jointly with Sir Peter Mansfield "for their discoveries concerning magnetic resonance imaging (Nobelprize.org 2013c)." The term "nuclear" was dropped from NMR due to negative connotations and public relation concerns, and that is why it is known today as MRI.

2.2.2 Nuclear magnetization

The behaviour of protons under magnetization is essential to understand how MRI obtains signals to reconstruct an image. Microscopic spinning, charged particles (protons and electrons) can be likened to a macroscopic bar magnet. The macroscopic bar is a magnetic dipole containing both north and south poles. The microscopic particles are also magnetic dipoles, and when placed in an external magnetic field, the dipoles will twist to align with it. Protons, neutrons, and electrons have discrete energy states when placed in an external field, either up or down aligned with or opposite to the external field.

2.2.3 Net magnetization

Hydrogen protons, in nuclei of hydrogen atoms, are the focus of most MRI in the human body. There are copious amounts of hydrogen atoms in tissues; within fat and water molecules, hydrogen content is 100 mol/kg in soft tissues and there are 10^{19} hydrogen nuclei in 1 mm^3 of tissue (Hendrick 1994). Without an external force, these positively charged protons are spinning about their axes and randomly oriented (Pooley 2005). The sums of their magnetic dipole vectors cancel each other out and there is no net magnetization. When placed in a strong external magnetic field, B_o, the protons will align

with or against the magnetic field. A small excess of nuclei, just a few dipoles per million hydrogen nuclei (Hendrick 1994), will be aligned with the magnetic field, creating a net magnetization, M_o (Pooley 2005). M_o is the source of the MR signal measured to reconstruct an MR image.

2.2.4 Main Magnetic Field

Placing the hydrogen atoms within a large magnetic field, referred to as a main magnetic field, B_o, produces the net magnetization, M_o. A typical clinical MRI has a main magnetic field with a strength of 1.5 T (Pooley 2005), which is a strong magnetic field since 1.0 T is approximately 20,000 times the Earth's magnetic field (Hendrick 1994).

2.2.5 MR Signal

When an object of interest is placed within the main magnetic field, the object's M_o will be aligned with the magnet in the +z direction, where the z-axis aligns with B_o. It is hard to measure the magnitude of M_o in the +z direction because it is parallel to a very strong magnetic field, B_o (Hendrick 1994), so M_o must be tipped into the transverse (x-y) plane. When M_o is in the transverse plane, it can be detected by a receiver coil, as it induces an electric current inside the coil that can be digitized and recorded for image reconstruction (Pooley 2005).

2.2.6 RF Energy

To tip the M_o into the transverse plane, a radio frequency (RF) pulse transmits energy at hydrogen's resonance frequency. At resonance, the most efficient transfer of energy will

occur. The resonance frequency is dependent on B_o and is also referred to as the Larmor frequency, which is defined as $\omega = \gamma B_o$, where γ is the gyromagnetic ratio. The gyromagnetic ratio of hydrogen is 42.58 MHz/T, so the Larmor frequency of hydrogen is approximately 64 MHz in a 1.5 T magnetic field (Pooley 2005). The magnetic dipole oscillates at the Larmor frequency. A perfect 90° RF pulse will tip the entire M_o into the transverse plane with zero magnetization left in the longitudinal direction.

2.2.7 Bloch equation

The Bloch equation, Equation 1, describes the motion of the magnetization, M, as a function of time dependent on the magnetic dipole's environment, T1 and T2 relaxation times.

$$\frac{d\vec{M}}{dt} = \gamma\vec{M}\times\vec{B} - \frac{M_x\hat{x}+M_y\hat{y}}{T_2} - \frac{M_z-M_o}{T_1}\hat{z} \quad (1)$$

T1 characterizes signal recovery in the longitudinal plane (+z axis), while T2 characterizes signal decay in the transverse plane. When M_o is tipped into the transverse plane, the signal measured in the transverse plane will eventually decay. T2 is a relaxation time that specifies when the signal reaches 37% of its maximum value in the transverse plane. As the signal decays in the transverse plane, the signal will begin to recover in the +z axis. T1 is longer than T2, so the transverse signal will typically decay much before the signal relaxes in the direction of the main magnetic field. T1 is a relaxation rate that specifies when M_o reaches 63% of its original signal in the +z axis before it was tipped into the transverse plane.

2.3 T1-weighted imaging

White matter appears bright and grey matter appears dark in adult T1-weighted MR images; however, this is reversed in neonates. There is a time during rapid development in the first two years of life that the differences will reverse due to myelination (Yoshida et al. 2013). T1 relaxation times are sensitive to myelin precursory proteins and the establishment of myelin sheath, but are also sensitive to changes in axon fibre size, density and coherence; membrane permeability; and large lipids and proteins (Deoni et al. 2012). T1 relaxation rates are dependent on the type of tissue; for example, white matter T1 at 1.5 T is 870 ms while grey matter T1 at 1.5 T is 900 ms (Bushberg 2002). These differences in T1 relaxation rates are the primary source of contrast in T1-weighted images. However, T1-weighted MR images are affected by but not specific to myelin content (Alsop, Dandamudi, and Bakshi 2007). Anatomical images are important for image registration and mapping other measured values to a spatial location in the brain. Anatomical information from the brain has been used to study the brain and tissue volume changes (Lebel et al. 2008). The total human brain volume remains approximately constant from early childhood (5 years of age) to adulthood while individual tissue components of the brain undergo developmental changes (Lebel et al. 2008). Studies have observed a steady increase of white matter volume during development between ages 4 to 21 years (Giedd et al. 1999), 5 to 17 years (Reiss et al. 1996), and 5 to 32 years (Lebel and Beaulieu 2011). Trajectories of linear volume changes in white matter areas have also been documented, such as the corpus callosum (Giedd et al. 1996).

2.4 Diffusion imaging

Diffusion effects on the NMR signal were discovered in the 1950s. Diffusion-weighted imaging exploits these effects to analyze water diffusion within the brain. Barriers such as cell membranes and myelin restrict diffusion; therefore, diffusion measurements throughout the brain are thought to reflect tissue microstructure (Basser, Mattiello, and Lebihan 1994, Beaulieu 2002). Diffusion can be sampled in specific directions using diffusion gradients during image acquisition. The b-value indicates the diffusion weighting, given in Equation 2, that are characterized by timing parameters (δ, Δ), gyromagnetic ratio (γ), and diffusion gradient strength (G, where $\vec{G} = \overrightarrow{G_x} + \overrightarrow{G_y} + \overrightarrow{G_z}$).

$$b = \gamma^2 G^2 \delta^2 (\Delta - \frac{\delta}{3}) \quad (2)$$

DTI is an MR diffusion imaging technique, which requires a minimum of six non-collinear directions ($b > 0$) and a reference scan ($b = 0$) (Basser, Mattiello, and Lebihan 1994). A tensor is calculated to describe the 3D diffusion behaviour. A tensor uses mathematical properties to describe the surface of an ellipsoid by specifying the shape and orientation using matrix mathematics. Diffusion sampled in six non-collinear directions and a reference scan (b = 0) is the minimum requirement to define a tensor. A tensor is often visually represented as an ellipsoid, as seen in Figure 1. An elongated and narrow ellipsoid is highly anisotropic, as diffusion is heavily weighted in one direction (along the elongated axis). A round ellipsoid (spherical) indicates isotropic diffusion. The tensor is calculated on

a voxel-wise basis and can be characterized by eigenvectors $(\overrightarrow{\lambda_1}, \overrightarrow{\lambda_2}, \overrightarrow{\lambda_3})$ and the resulting eigenvalues $(\lambda_1, \lambda_2, \lambda_3)$ where $(|\overrightarrow{\lambda_1}|, |\overrightarrow{\lambda_2}|, |\overrightarrow{\lambda_3}|) = (\lambda_1, \lambda_2, \lambda_3)$. Fractional anisotropy (FA), mean diffusivity (MD), axial diffusivity (AD), and radial diffusivity (RD) can be derived from the eigenvalues by Equations 3 – 6. Primary direction of diffusion is determined by the direction of the first eigenvector; using these directions, color maps of the brain to indicate primary diffusion direction in each voxel can be obtained.

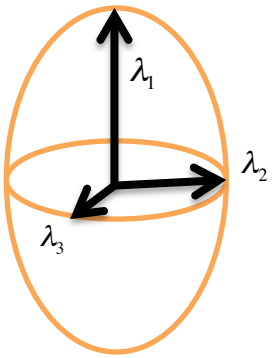

Figure 1. Ellipsoid characterized by 3 eigenvectors.

$$FA = \frac{\sqrt{\frac{3}{2}}\sqrt{(\lambda_1-\hat{\lambda})^2+(\lambda_2-\hat{\lambda})^2+(\lambda_3-\hat{\lambda})^2}}{\sqrt{\lambda_1^2+\lambda_2^2+\lambda_3^2}} \quad (3)$$

$$MD = \frac{\lambda_1+\lambda_2+\lambda_3}{3} \quad (4)$$

$$AD = \lambda_1 \quad (5)$$

$$RD = \frac{\lambda_2+\lambda_3}{3} \quad (6)$$

FA, Equation 3, is a measure that ranges from 0 to 1 and indicates the degree of directionality of diffusion. A value of 0 would be isotropic diffusion, equal in all directions, and represented by a spherical ellipsoid. As FA increases, the ellipsoid becomes elongated and diffusion becomes more anisotropic. MD, Equation 4, is also known as the apparent diffusion coefficient, indicates the average diffusivity in the voxel. AD, Equation 5, is the magnitude of diffusivity along the preferential direction of diffusion, and RD, Equation 6, is the diffusivity perpendicular to this axis. All of these measurements of FA and MD reflect aspects of white matter integrity (Lochner et al. 2012). Generally, more myelin and denser axons will restrict water diffusion in and across axon fibres, especially perpendicular to direction of the axons. The main morphological factor that affects diffusion is axonal membranes, while the presence of myelin modulates the degree of anisotropy (Beaulieu 2002, Beaulieu 1994, Gulani 2001). The increases in white matter FA observed during brain maturation may be correlated with developmental expansion of immature oligodendrocytes during premyelination, proliferation and maturation of glial cell bodies, and myelin maturation around axons. Measures of FA can also be related to axonal packing, relative membrane permeability to water, internal axon structure and tissue water content (Yoshida et al. 2013). DTI does not provide specific quantitative measurements of myelin, but it does provide measures of diffusion that give insight into the microscopic detail of myelin and axonal packing in white and grey matter.

While only one tensor is calculated in each voxel, it reflects the contributions of multiple microstructures such as myelin, axonal components and glial cells. One study that measured diameters of human myelinated axons in cortical white matter via electron microscopy post-mortem found axon diameters ranging from 0.16 μm to 9 μm, with the majority of axons averaging diameters less than 1 μm (Liewald et al. 2014). The resolution of MRI is in the millimetre range, thus many axons and other cellular structures can be captured within a voxel and these axons may align, cross, or kiss each other. DTI measures are aggregate quantities leading to a partial volume effect because microscopic details, such as crossing or kissing fibres, of each axon are lost due to the limited resolution used in MRI. Diffusion from multiple axons is averaged together to represent one tensor in each voxel; only one preferential direction can be determined even if fibres are diffusing in two directions (ex, at a crossing point).

2.5 Magnetization transfer imaging

Magnetization transfer (MT) imaging provides a unique contrast between liquid pools and macromolecule pools. Macromolecules have a broad absorption line shape in comparison to liquids, as seen in Figure 2, causing macromolecules to be 10^6 more times sensitive to an off-resonance RF pulse (Henkelman, Stanisz, and Graham 2001). The macromolecular pool cannot be imaged directly because the T2 values of macromolecules, at less than 1 ms, are much smaller than what can be conventionally captured in MRI. MT imaging is an indirect approach to quantify the presence of macromolecules by applying a preparatory off-resonance pulse. The protons in macromolecules are tipped down, and then these spins

cause part of the liquid pool to be tipped down by an exchange process. The liquid pool is then imaged conventionally after the exchange process; the resulting image is called M_{SAT}, and the signal is reduced proportional to the concentration of macromolecules. It can be compared to a baseline image without the off-resonance pulse preparation resulting in a measure called M_o. A common measure derived from M_{SAT} and M_o is the MT ratio (MTR), which is defined in Equation 7. MTR has been used for white matter-grey matter contrast based on the assumption that contrast arises from myelin-associated lipids, as MTR has been found to be positively correlated with myelin content (Schmierer 2004); however, the off-resonance pulse is not specific to myelin, but is sensitive to other macromolecules as well.

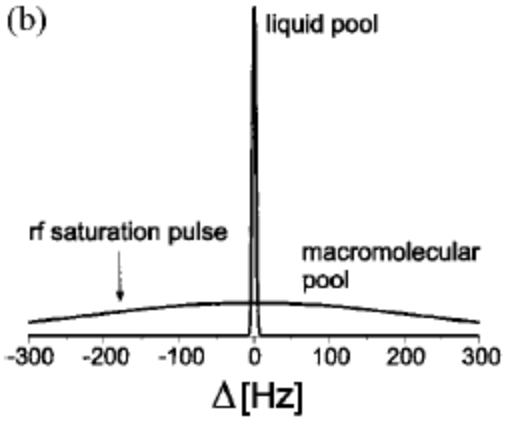

Figure 2. The absorption lines of macromolecular and liquid pools. The macromolecular pool has a broader lineshape; it can be saturated with an off-resonance RF pulse. Reprinted with permission from John Wiley and Sons (Henkelman, Stanisz, and Graham 2001) (Fig 1b). Copyright permissions are in Appendix A.

$$MTR = \frac{M_O - M_{SAT}}{M_O} \quad (7)$$

2.6 Inhomogeneous magnetization transfer imaging

ihMT imaging is a new variant of MT imaging that virtually eliminates signal from unmyelinated tissues and provides a quantitative measure sensitive to motion-restricted lipid chains in membranes that are far more dense in myelinated tissues (Varma 2015). MT imaging applies an off-resonance pulse at an arbitrary +f frequency, while ihMT exploits the inhomogeneity in myelin macromolecules' line shape by applying off-resonance pulses at +f and –f. If macromolecules being imaged have a homogenous line shape, then +f and –f pulses have identical effects on the liquid pool, while inhomogeneous line shapes exhibit differences (Varma 2015). Measurements of ihMT ratio are significantly different than MTR (Varma 2015). ihMT may provide a biomarker specific to myelin, which may be useful to further characterize white matter development.

2.7 Multi-component analyses

A single voxel in a conventional MRI image likely contains multiple micro-anatomical regions. This leads to a partial volume effect – the averaging of multiple components such that each component is not discernible. Solving an equation modeling different components within a single voxel can allow more tissue microstructure information to be resolved. Two techniques that model multiple compartments within individual voxels are NODDI and mcDESPOT.

2.7.1 NODDI

NODDI is an advanced diffusion imaging technique used to capture neurite (dendrites and axons) morphology. DTI has been used to assess underlying biological structures, however, the data collected is non-specific to micro-anatomical regions within voxels. NODDI uses a three-compartment micro-anatomical region model: intra-cellular (ic), extra-cellular (ec), and cerebral spinal fluid (CSF or isotropic) (Zhang et al. 2012). Quantification of neurite density and orientation provides more specific parameters of neuronal tracts than conventional DTI analysis by modelling multiple MRI measurements in each voxel.

The model used in NODDI is given in Equation 8. The measured signal, A, is used to solve for volume fractions (v_x) and normalized signals (A_x) of the intra-cellar (A_{ic}, v_{ic}), extra-cellular (A_{ec}, v_{ec}), and CSF (A_{iso}, v_{iso}) compartments. The neurite orientation is modeled using the Watson distribution that is characterized by κ (where κ > 0, rotationally invariant). A small value indicates large dispersion, likely in grey matter, while a large value indicates small dispersion, likely in white matter. κ is used to calculate an orientation density index (ODI), given in Equation 9, that allows for a more intuitive understanding of dispersion. ODI ranges from 0 to 1, with a higher value indicating higher dispersion. CSF diffusivity and axial intra/extra-cellular diffusivities are fixed in the model.

$$A = (1 - v_{iso})(v_{ic}A_{ic} + (1 - v_{ic})A_{ec}) + v_{iso}A_{\mathrm{iso}} \qquad (8)$$

$$ODI = \frac{2}{\pi}\arctan\left(\frac{1}{\kappa}\right) \quad (9)$$

NODDI was designed as a technique to provide more detail than standard DTI, without requiring intensive imaging. DTI requires at least 1 non-zero b-shell while NODDI requires at least 2 non-zero b-shells. More complex models can be used to estimate axon diameter and orientation dispersion from diffusion-weighted imaging but they require many directions with many b-values, which can take an hour of imaging for one adult subject (Zhang et al. 2011).

2.7.2 mcDESPOT

The mcDESPOT voxel components are broken into 3 components: myelin-bound water, intra/extra cellular water and free water (Deoni, Matthews, and Kolind 2013). The fraction of myelin-bound water can be calculated (myelin water fraction, MWF = myelin water/total water), and serves as an indicator of myelin present in each voxel. MWF mapping has been used in infants and MWF measures correlates strongly with post-mortem trends and other imaging results (Deoni et al. 2011). Similar myelin water imaging techniques have been used in other applications, but not to study development (Borich et al. 2013, Laule et al. 2006, Vargas et al. 2015).

mcDESPOT requires spoiled gradient echo (SPGR) and fully-balanced steady-state free precession (bSSFP) images over a range of flip angles. An IR-SPGR image is additionally required to correct B_1 inhomogeneities (Deoni 2011), where B_1 is the magnetic field that

transmits energy to the net magnization, M_o. bSSFP image acquisition is repeated with incremented phase by 180° to correct for B_o inhomogeneities (Deoni 2011). Multi-angle data from SPGR and bSSFP are used to fit parameters (T1, T2, volume fractions) relating to the 3 pools of water: myelin-bound water (M), intra/extra cellular water (IE) and free water (F). Myelin-bound and intra/cellular water are assumed to be exchanging pools of water, while free water is non-exchanging (Deoni, Matthews, and Kolind 2013) as illustrated in Figure 3.

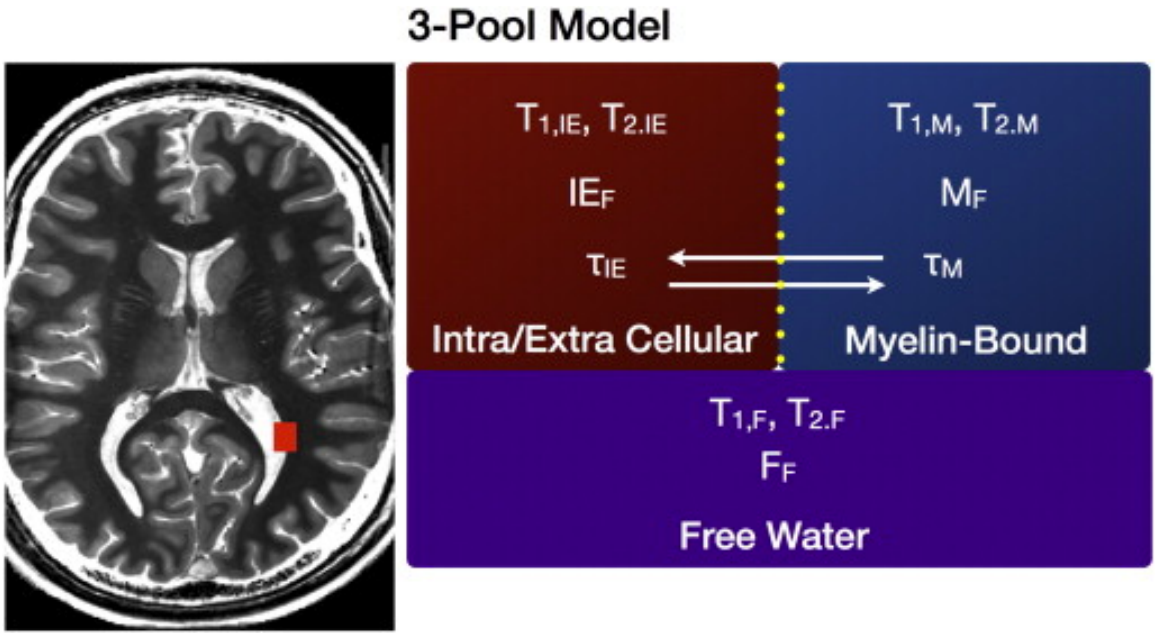

Figure 3. The components of red voxel (on the left) may contain multiple anatomical regions. The 3-pool model (on the right) contains intra/extra cellular, myelin-bound, and free water compartments. Exchange is shown between the intra/extra cellular and myelin-bound water compartments. Figure is reprinted under the Creative Commons Attribution License (CC BY) from (Deoni et al. 2012) (Fig 1).

2.8 Susceptibility-weighted imaging

Susceptibility-weighted imaging (SWI) utilizes MRI phase information resulting in images reflecting differences in magnetic susceptibility of tissues. Magnetic susceptibility is a measure of a material's induced magnetic field in the presence of an external magnetic field. The resulting images represent the convolution of the magnetic susceptibility distribution with the magnetic field generated by magnetic dipoles. Susceptibility contrast is enhanced between paramagnetic and diamagnetic components in the brain. Tissue iron is paramagnetic, while macromolecules, such as those in myelin, are diamagnetic (Zhong et al. 2011). Phase contrast is also dependent on water-macromolecular exchange (WME), which depends on the molecular size of macromolecules and their distribution in tissue (Zhong et al. 2011). Unlike T1-weighted images, phase contrast between white and gray matter does not reverse from birth to adulthood. Gray matter has a greater positive phase than white matter; phase differences of 0.0035 parts per million (ppm) in neonates and 0.01 ppm in adults have been observed, and this increase may be attributed to myelin (Zhong et al. 2011). The phase differences between white matter and gray matter are indicative of myelination; however, they are not specific to it (Lodygensky et al. 2012). Myelination and water-macromolecule exchange concentrations are likely the major contributors to phase contrast between white and gray matter but their effects have not yet been separated (Zhong et al. 2011).

2.9 Quantitative susceptibility mapping

While SWI can provide contrast between white and grey matter, it does not provide quantitative measures of magnetic susceptibility for each tissue. Quantitative susceptibility mapping (QSM) (Liu 2009) is a method to quantify the susceptibility distribution (parts per million) in each voxel by de-convolving the SWI images via a numerical method. Myelin has been found to induce susceptibility anisotropy, which may be helpful to further describe white matter microstructure by determining quantitative susceptibility (Li et al. 2012). QSM can provide a quantitative measure that can be used to help describe white matter development more specifically than SWI by facilitating comparison of regions with a quantitative value or tracking changes within regions.

2.10 Image registration

The analysis of MRI images can use regions-of-interest to compare the same anatomical regions across multiple subjects. Manual delineation of regions-of-interest (ex. the cingulum white matter tract) can be performed on each subject; however, this may be time consuming and dependent on the person performing this task (i.e. a rater). To save time especially for large datasets and to avoid inter-rater and intra-rater variability, an automated approach may be used. Image registration transforms each subject's MRI images to a common space (i.e. common template), so that all the subjects can be compared in that common space. Regions-of-interest (ex. the cingulum white matter tract) may be defined on a template, so measurements pertaining to each region-of-interest is consistent across all subjects. Image transformations may be linear or non-linear. Linear transformation includes translation, rotation, scaling, and shearing. Non-linear transformation accounts for local deformations that cannot be accomplished with only

linear transformation. Intra-subject registration should be performed between MRI scans (ex. between T1-weighted and MT images) because the subject may move in between scans; linear registration is appropriate for subject movement. FSL's FLIRT (Jenkinson and Smith 2001, Jenkinson et al. 2002, Jenkinson et al. 2012) or Advanced Normalization Tools (ANTs) (Avants et al. 2011) are applications that can be used for linear registration. Inter-subject registration should use non-linear applications, such as FSL's FNIRT (Jenkinson et al. 2012) or ANTs.

2.11 Study rationale

The study of healthy development is necessary to understand the deviations that may occur in neurological disorders, including the timing of divergence from normal developing processes and quantifying the pathological differences between healthy and abnormal development. Subtle changes of myelination and axonal calibre occur during development throughout childhood and even into adulthood. However, these characteristics are difficult to capture using conventional MRI techniques because of the lack of resolution and signal specificity to separate the developmental processes. Though neurodevelopment has been studied extensively, with the emergence of newer imaging techniques, a more comprehensive understanding can be achieved though their application. NODDI, ihMT, mcDESPOT, and QSM may help elucidate the microstructural changes within a voxel that will improve microstructural resolution of the developmental changes that we can observe.

Chapter Three: **Childhood and adolescence development using NODDI**

3.1 Introduction

White matter is essential for relaying information between different regions in the brain, and it is made up of axons surrounded by a myelin sheath. The speed of transmission along an axon is affected by the diameter of the axon and the thickness of its myelin sheath (Aboitiz et al. 1992). Grey matter contains mostly neuronal cell bodies, and relies on white matter connectivity to carry out sensory perception, muscle control, and mental actions. Myelination is a process that begins in utero and continues into early adulthood, and normal development of white matter in tandem with grey matter is critical to enable higher order behavioural and cognitive functioning.

Brain development was initially understood via post-mortem studies that demonstrated brain volume increases (Dekaban 1978), cortical growth and pruning (Landing et al. 2002), and myelination (Benes 1989, Yakovlev and Lecours 1967, Brody et al. 1987). Magnetic resonance imaging (MRI) studies of healthy brain development *in vivo* have also been able to characterize brain and tissue volume changes in large datasets. It can also provide detailed tissue microstructural information, such as indicators of myelin content and axonal packing. Various techniques, such as T1-weighted anatomical, diffusion tensor imaging (DTI), and magnetization transfer (MT) imaging have been used to study healthy white matter and grey matter development during childhood and adolescence (Yoshida et al. 2013, Paus et al. 1999, Leppert et al. 2009). *In vivo* data from MRI has shown rapid white matter development during infancy (Dubois et al. 2008, Yoshida et al. 2013) and slower,

subtler changes in adolescence (Lebel and Beaulieu 2011, Deoni et al. 2012) that suggest increases in myelination. Regional patterns of development in white matter can also be detailed. For example, sensory regions develop earlier than frontal association regions (Aboitiz et al. 1992, Dubois et al. 2014), which mature later and slower (Lebel et al. 2008). While these previous reports are suggestive of increased myelination, they are sensitive to multiple processes (e.g., myelination, axonal packing, water content, other anatomical components) and are not specific to myelination.

Myelin water fraction (MWF) imaging provides a measure sensitive to the amount of myelin in each voxel using a multi-component model that results in MWF as myelin-bound water divided by total water content (Deoni, Matthews, and Kolind 2013). MWF mapping has been used in children aged 0 to 5 years (Deoni et al. 2012) showing rapid growth of myelin during infancy (0-2 years), and the resulting spatio-temporal pattern of myelination compared well against post-mortem trends (Deoni et al. 2011, Yakovlev and Lecours 1967, Kinney et al. 1988). DTI is a diffusion imaging technique that describes diffusion in each voxel by sampling diffusion using a minimum of six non-collinear directions. Fractional anisotropy (FA) is a measure of DTI that indicates how anisotropic diffusion is in each voxel. FA has been used as an indicator of white matter development (Lebel and Beaulieu 2011) since diffusion occurs preferentially along axons due to increased myelination and axonal packing.

Neurite orientation dispersion and density imaging (NODDI) is another multi-component model using MR diffusion data that captures neurite (dendrites and axons) morphology (Zhang et al. 2012). NODDI uses a specific three-compartment micro-anatomical region model: intra-cellular, extra-cellular, and cerebral spinal fluid (CSF). The result in output parameters of neurite density index (NDI) and orientation density index (ODI), which provide more insight than DTI into the changing cellular architecture. Newborns scanned at term using NODDI showed a strong negative correlation between ODI and FA, and a positive correlation between NDI and FA in white matter regions-of-interest (ROIs) (Kunz et al. 2014). A longitudinal study of pre-term babies showed that changes in FA in grey matter cortex was driven by changes in ODI while changes in FA in the thalamus was driven by changes in NDI (Eaton-Rosen et al. 2015). Only one previous NODDI study explored maturation (7-63 years) and found that NDI followed a logarithmic growth curve, increasing throughout childhood into adulthood, while ODI followed an exponential curve exhibiting slow growth during childhood and late adolescence before accelerating up during adulthood. However, white matter tracts were studied by categories (association, limbic, callosal, etc.) rather than targeting specific tracts (cingulum, uncinate, forceps major, etc.) (Chang et al. 2015). Neurite density increases suggest myelination, axonal growth or greater axonal density. NODDI can be applied to grey matter regions, and has been used to study grey matter in preterm subjects (Eaton-Rosen et al. 2015). DTI has been applied to grey matter subcortical regions along with white matter regions (Mukherjee et al. 2001, Snook et al. 2005). Imaging techniques more specific to myelin have shown rapid growth of myelin during early infancy and continued changes in white matter into

adulthood that may be due to changes in myelin or axonal packing. Subcortical grey matter has not yet been modelled with NODDI during adolescence to our knowledge. Much more can be added to our understanding in late childhood by investigating subjects focused within this timeframe to analyze morphological developmental changes of neurites in specific white matter and subcortical grey matter regions.

The goal of this study was to use diffusion parameters obtained from NODDI and DTI to study white matter and subcortical grey matter changes during normal adolescent development (8 to 13 years). As brain maturation trajectories can be a sensitive marker of abnormalities (Giedd et al. 2008), the information provided by this research may be useful for early identification of developmental disorders. Advancing knowledge of healthy brain changes in children will aid in characterizing structural brain development from birth to adulthood.

3.2 Methods

3.2.1 Subject demographics

27 healthy participants (12 F/15 M) aged 8-13 years (mean +/- sd: 11.3 +/- 1.9 years) were recruited for this study. Informed written assent was obtained from each subject and his or her parent or guardian provided written consent. Exclusion criteria were known diagnosed developmental and reading disorders, undiagnosed reading disorders, history of neurosurgery, and any contraindications to MRI.

3.2.2 MRI Acquisition

MRI data was collected on a 3T MR system (Discovery 750w; General Electric; Waukesha, WI) using a 32-channel head coil at the Alberta Children's Hospital.

T1-weighted anatomical images were acquired with the following parameters: TI = 600 ms, TR/TE = 8.208/3.156 ms, 0.8 mm^3 isotropic resolution, scan time = 5:38 min:sec.

Diffusion weighted images were acquired with 10 b = 0 s/mm^2 images, and two non-zero b-values each with 30 directions: spin echo EPI, b = 900 and 2000 s/mm^2, TR/TE = 12 s/88 ms, 2.2 mm^3 isotropic resolution, scan time = 14:24 min:sec. The b0 (b = 0 s/mm^2) images were scattered throughout the acquisition, rather than all collected at the beginning, and the order of the directions were optimized to facilitate reconstruction from partial data if necessary. Removal of data was not necessary for this study as all data was of good quality.

3.2.3 Image analysis

Diffusion-weighted images with b=0, 900 s/mm^2 were used to compute the diffusion tensor to obtain FA, MD, RD, and AD maps. Diffusion-weighted images from b=0, 900 and 2000 s/mm^2 were used to fit to the NODDI model, using the NODDI Matlab Toolbox (http://www.nitrc.org/projects/noddi_toolbox). Equation 10 describes the model (Zhang et al. 2012),

$$A = (1 - v_{iso})(v_{ic}A_{ic} + (1 - v_{ic})A_{ec}) + v_{iso}A_{iso}, \quad (10)$$

where the measured diffusion signal, A, is fitted to the 3 compartment volume fraction (v) and signal (A) (ic: intra-cellular, ec: extra-cellular, iso: CSF). Here, NDI (fibre volume fraction) refers to $(1 - v_{iso})v_{ic}$ of Equation 10. ODI (orientation density index) is also obtained from the model fitting, where $0 \leq ODI \leq 1$, and higher values indicate high dispersion.

3.2.4 Registration

Advanced Normalization Tools (ANTs) (Avants et al. 2011) was used to perform intra-subject registration from subjects' diffusion and MTR spaces to T1-weighted space. Linear registration in ANTs was used to normalize each subject's diffusion b0 and MTR images to their respective T1-weighted image.

3.2.5 Regions of interest

T1 and diffusion (b=0, 900 images s/mm^2) data were processed in FreeSurfer (Reuter et al. 2012, Yendiki et al. 2011) to give automatically segmented white matter tracts and grey matter structures. These white and grey matter regions served as volumes-of-interest to obtain regional mean values of NDI, ODI, FA, MD, RD, and AD. White matter regions delineated were the anterior thalamic radiation (ATR), cingulum, cortical spinal tract (CST), forceps major & minor, inferior longitudinal (ILF), superior longitudinal (SLF), and uncinate fasciculi. Grey matter regions identified were the amygdala, caudate, hippocampus, pallidum, putamen, and thalamus. The white matter regions were segmented

in diffusion space, and they were transformed to T1-weighted space. The subcortical grey matter regions were segmented in T1-weighted space. Using the white and grey matter masks in T1-weighted space, means of measures from NODDI (NDI, ODI) and DTI (FA, MD, RD, AD) were extracted for each region.

Linear models using a first-degree polynomial were used to fit each output parameter with respect to age. A linear approximation is appropriate because slow development is expected during late childhood and adolescence, especially during a small window from 8 to 13 years. The significance level was chosen as 0.05, and the false discovery rate method was used to correct for multiple comparisons.

3.2.6 K-means clustering

K-means clustering was performed on the NDI-age slope and ODI mean to group clusters based on similar development profiles using the Hartigan and Wong algorithm in R (Hartigan and Wong 1979). This leads to the observed data points to be partitioned into k number of groups. The goal is to reduce the sum of squares of the points in a cluster to the mean of the cluster. The rate of change of NDI with age (slope) and the mean ODI across subjects were calculated voxel-by-voxel in MNI space. Subjects' NDI and ODI maps were registered to the MNI152 template using ANTs and FSL (Jenkinson and Smith 2001, Jenkinson et al. 2002). Clustering was limited to voxels contained in a white matter and subcortical grey matter mask. White matter was segmented from the MNI template, and subcortical regions from the MNI structural atlas (caudate, putamen, and thalamus) were

added to the white matter from the MNI template to create the mask for k-means clustering.

3.3 Results

3.3.1 Changes with age

All white matter and grey matter (except the caudate) regions showed positive correlations between NDI and age (Figure 4, Table 3). In white matter, the steepest slope was observed in the forceps major ($m = 10.7 \times 10^{-3}$/year, $p<0.001$) followed by the SLF ($m=10.2 \times 10^{-3}$/year, $p<0.001$) and CST ($m=7.80 \times 10^{-3}$/year, $p<0.001$). The shallowest slope was observed in the forceps minor ($m=4.71 \times 10^{-3}$/year, $p=0.029$) and uncinate ($m=4.95 \times 10^{-3}$/year, $p=0.019$). In grey matter, the steepest rate of development was observed in the pallidum ($m=12.4 \times 10^{-3}$ /year, $p<0.001$), while the shallowest rate was observed in the putamen ($m=3.71 \times 10^{-3}$/year, $p=0.002$).

No regions had significant correlations between ODI and age (Figure 5). The cingulum, SLF, and uncinate had the highest values of ODI, while the CST, forceps major, forceps minor, and ILF had the lowest values of ODI. The thalamus showed the lowest values of ODI among grey matter regions.

White matter and grey matter regions showed positive correlations between FA and age, while negative correlations were found between MD and age. Negative correlations were also found between RD and age, as well as AD and age. Linear fits of FA vs. age were

significant in the following regions: ATR, cingulum, CST, ILF, and SLF; and, hippocampus, caudate, putamen, and thalamus (Figure 6, Table 4). Significant correlations between age and MD were found in all white matter regions, as well as the amygdala, hippocampus, pallidum, and putamen. Significant correlations between age and RD were found in the ATR, cingulum, CST, ILF, and SLF, and the amygdala, hippocampus, pallidum, and putamen. No significant correlations were found between age and AD. Plots and tables of the fitting results for MD, RD, and AD can be found in Appendix B.

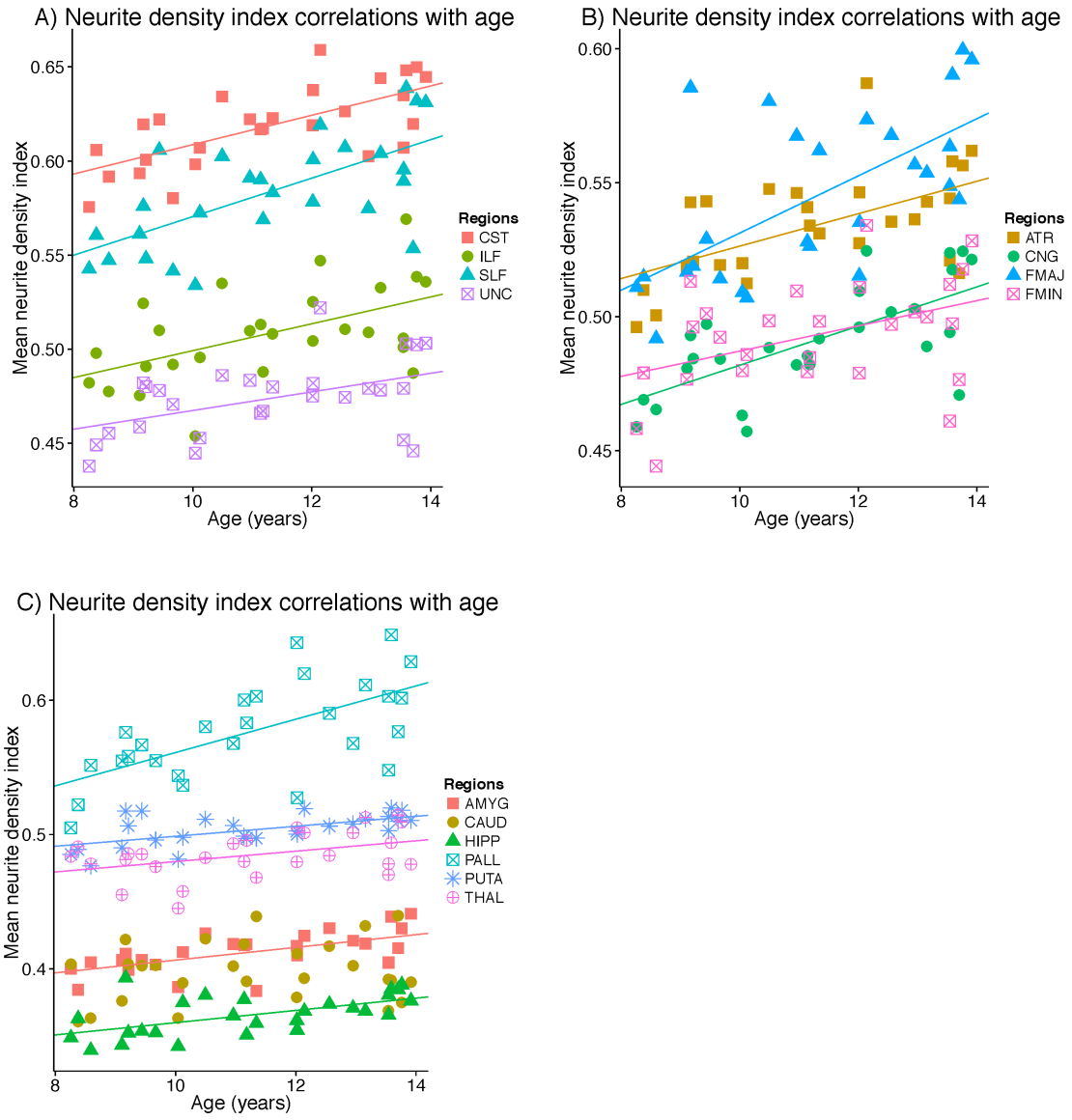

Figure 4. Neurite density index trajectories in white (A, B) and grey (C) matter volumes-of-interest. Significant lines of fit ($p<0.05$) are plotted on the graphs.

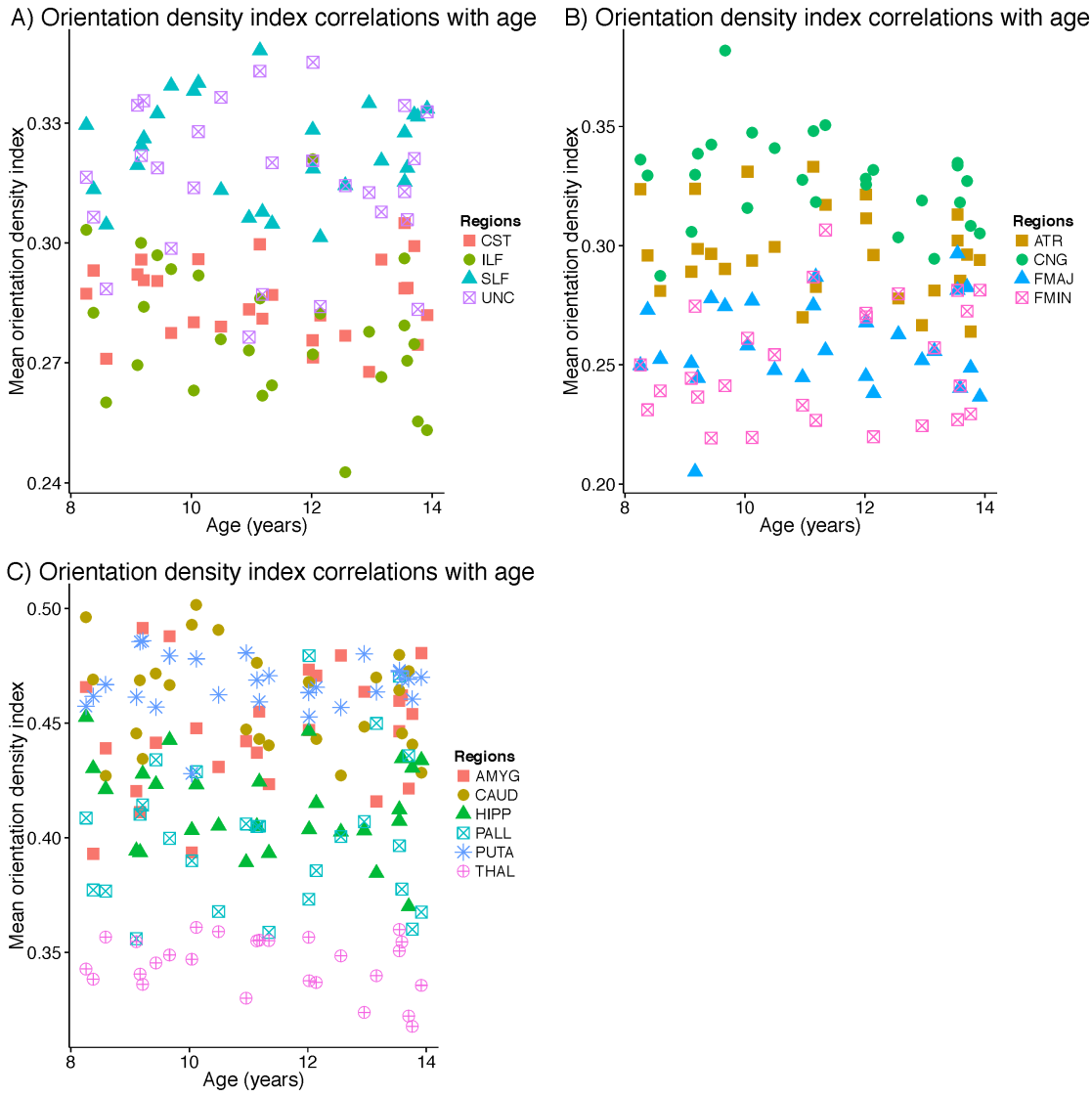

Figure 5. Orientation density index trajectories in white (A, B) and grey (C) matter volumes-of-interest. No regressions were signficiant.

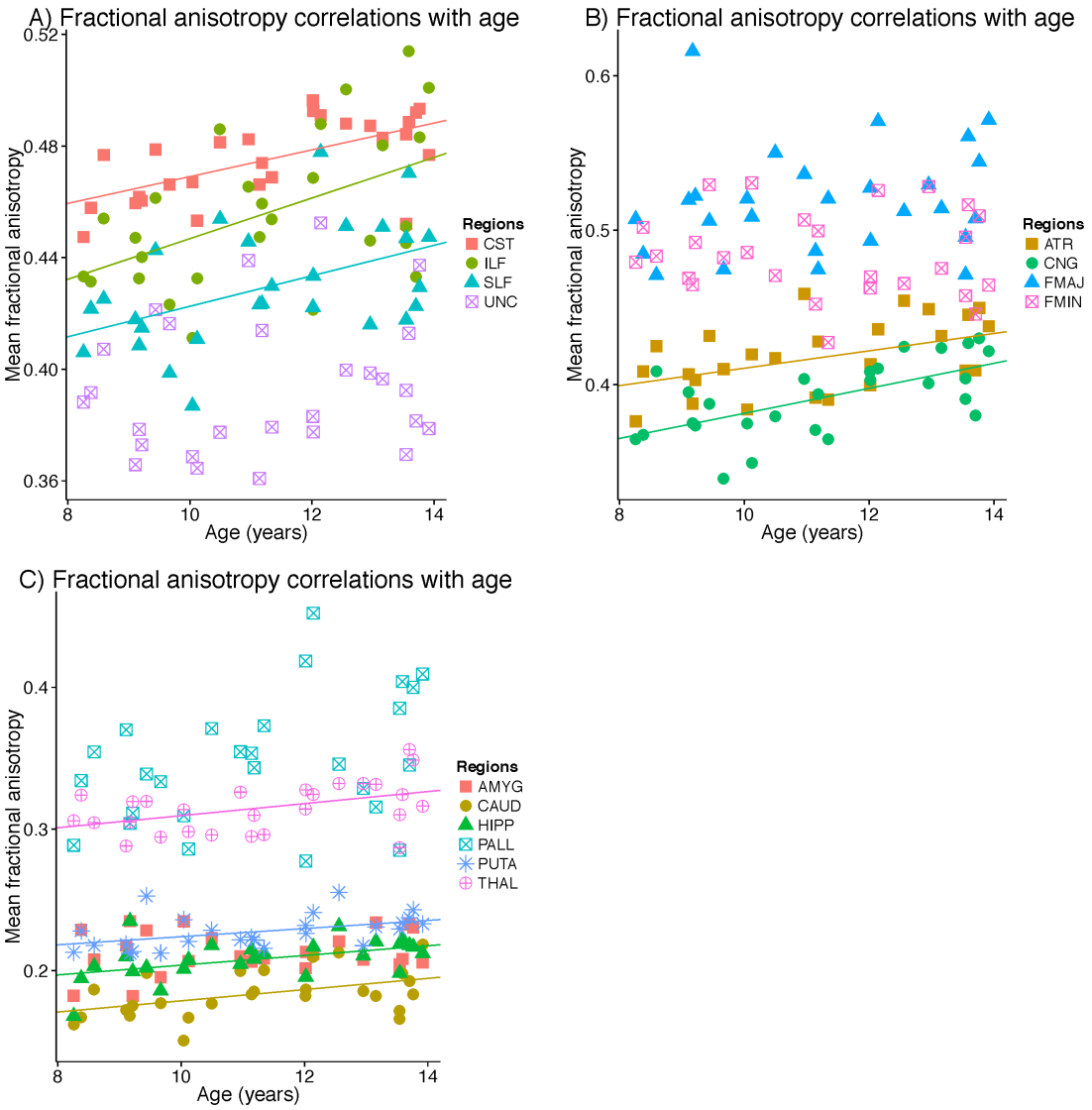

Figure 6. Fractional anisotropy trajectories in white (A, B) and grey (C) matter volumes-of-interest. Additionally, significant lines of fit ($p<0.05$) are plotted.

Table 3. Linear fitting results of NDI (neurite density) vs. age. The p-values were corrected for multiple comparisons using the false discovery rate method.

Region	Slope, m (10^{-3}/year)	Y-intercept, b	R^2	p
ATR	6.05	0.466	0.32	**0.003**
Cingulum	7.31	0.409	0.47	**<0.001**
CST	7.80	0.531	0.47	**<0.001**
Forceps major	10.7	0.425	0.42	**<0.001**
Forceps minor	4.71	0.440	0.18	**0.029**
ILF	7.14	0.428	0.29	**0.005**
SLF	10.2	0.468	0.43	**<0.001**
Uncinate	4.95	0.418	0.21	**0.019**
Amygdala	4.73	0.359	0.36	**0.002**
Caudate	2.22	0.373	0.03	0.353
Hippocampus	4.56	0.315	0.33	**0.003**
Pallidum	12.4	0.437	0.41	**<0.001**
Putamen	3.71	0.462	0.35	**0.002**
Thalamus	3.86	0.441	0.18	**0.029**

Table 4. Linear fitting results of FA (fractional anisotropy) vs. age. The p-values were corrected for multiple comparisons using the false discovery rate method.

Region	Slope, m (10^{-3}/year)	Y-intercept, b	R^2	p
ATR	5.62	0.354	0.22	**0.026**
Cingulum	8.11	0.300	0.39	**0.003**
CST	4.80	0.421	0.40	**0.003**
Forceps major	2.99	0.485	0.03	0.532
Forceps minor	-1.19	0.498	0.01	0.686
ILF	7.28	0.374	0.26	**0.026**
SLF	5.47	0.368	0.24	**0.026**
Uncinate	1.92	0.372	0.02	0.538
Amygdala	0.97	0.202	0.02	0.577
Caudate	3.96	0.139	0.21	**0.026**
Hippocampus	3.43	0.169	0.22	**0.026**
Pallidum	8.83	0.248	0.14	0.078
Putamen	2.87	0.195	0.22	**0.026**
Thalamus	4.26	0.267	0.21	**0.026**

3.3.2 K-means clustering

The sum of squared error (SSE) vs. the number of clusters was used to determine the optimal number of clusters in the k-means clustering analysis. The "elbow" of the curve, where increasing the number of clusters does not seem to result in a substantial change of SSE much further, occurs at k=4 (Figure 7).

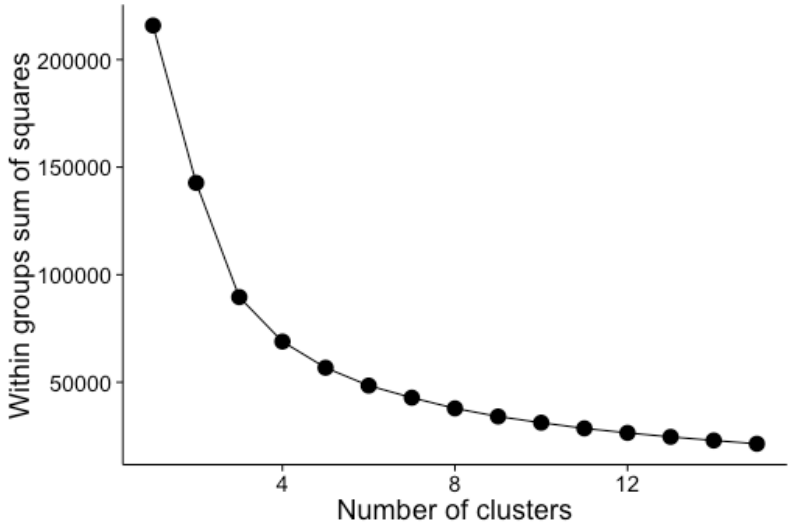

Figure 7. Within groups sum of squared error as a function of number of clusters.

Clusters created from k=4 are shown in Figure 8, and the mean values of NDI-slope and ODI of each cluster are shown in Table 5. A 6-cluster solution was also explored and these results are found in Table 6 and Figure 9. Clustering was also performed on NDI-slope (Table 7, Figure 10) and ODI-mean each on their own (Table 8, Figure 11).

The 4-cluster solution of NDI-slope and ODI-mean consists of clusters primarily containing (in no particular order): (1) the cores of white matter tracts, (2) the first layer of

subcortical white matter, as well as the caudate and putamen, (3) the intermediate layer of white matter, (4) the posterior section of the genu of the corpus callosum and the mid-section of the CST. The 6-cluster solution of NDI-slope and ODI-mean contains (in no particular order): (1) forceps major, (2) corona radiata, forceps minor, (3) thalamus, (4) part of the subcortical white matter, caudate, putamen, (5) genu of the corpus callosum, and (6) SLF. When considering only NDI, the 4-cluster solution contains (in no particular order): (1) the genu of the corpus callosum, (2) the forceps major, (3) the subcortical grey matter and the first layer of subcortical white matter, (4) the intermediate layer and cores of white matter tracts. The 4-cluster solution using only ODI contains (in no particular order): (1) the cores of white matter tracts, (2) the first layer of subcortical white matter, and the caudate and putamen, (3) the second layer of subcortical white matter, and thalamus, and (4) the third layer of subcortical white matter (between the core and second layer of subcortical white matter).

Table 5. Means of NDI-slope and ODI in each cluster from k-means clustering for k=4.

Cluster number	Mean NDI slope (10^{-3}/year)	Mean ODI
1	8.09	0.390
2	-7.45	0.310
3	10.64	0.240
4	3.61	0.521

Table 6. Means of NDI-slope and ODI in each cluster from k-means clustering for k=6.

Cluster number	Mean NDI slope (10^{-3}/year)	Mean ODI
1	16.01	0.221
2	-11.51	0.306
3	4.07	0.548
4	5.86	0.265
5	2.72	0.414
6	11.09	0.405

Table 7. Means of NDI-slope in each cluster from k-means clustering for k=4.

Cluster number	Mean NDI slope (10^{-3}/year)
1	1.46
2	15.3
3	7.76
4	-12.4

Table 8. Means of ODI-mean in each cluster from k-means clustering for k=4.

Cluster number	Mean ODI
1	0.325
2	0.433
3	0.551
4	0.202

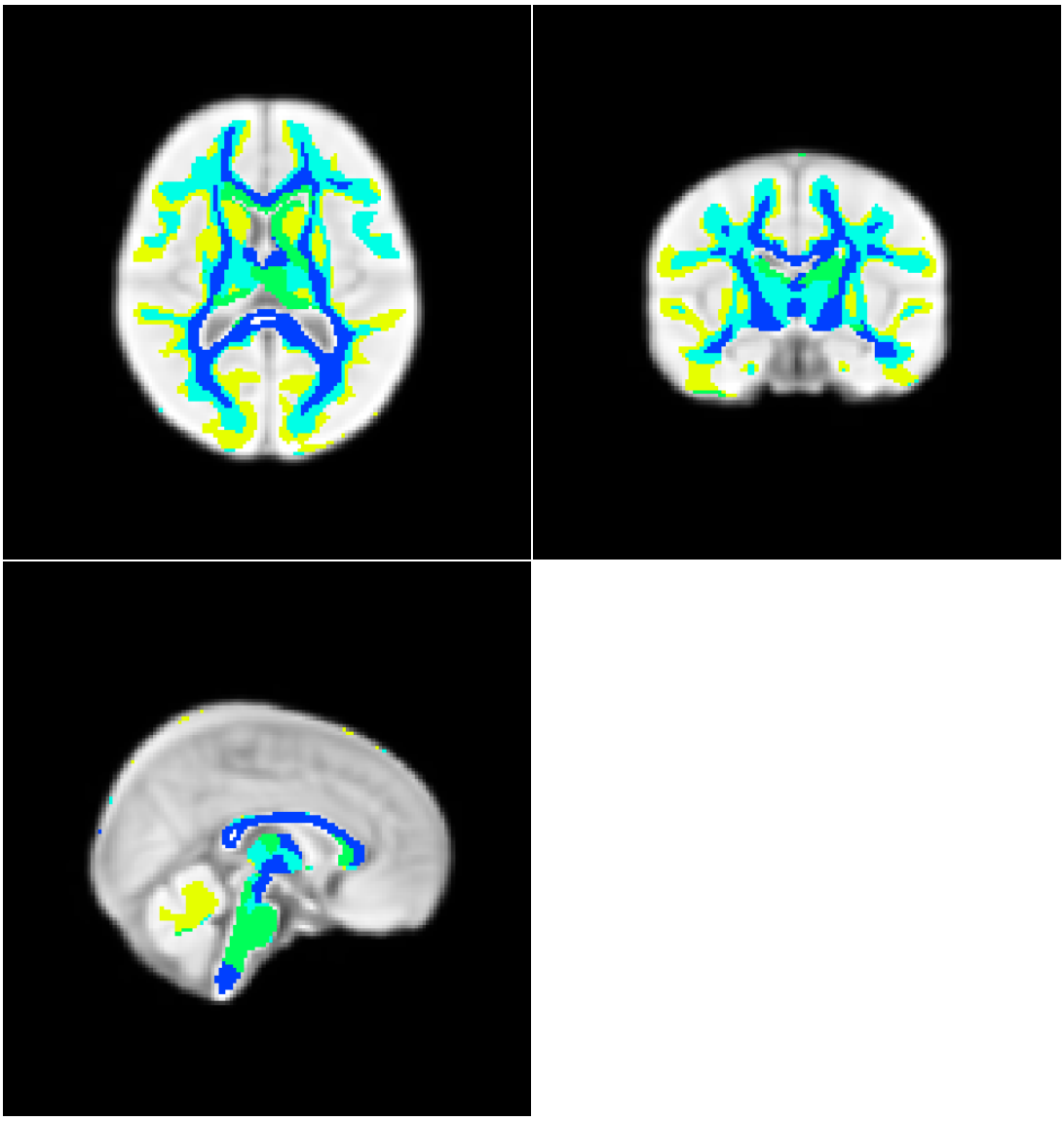

Figure 8. Clusters defined by k-means clustering of NDI and ODI with k=4.

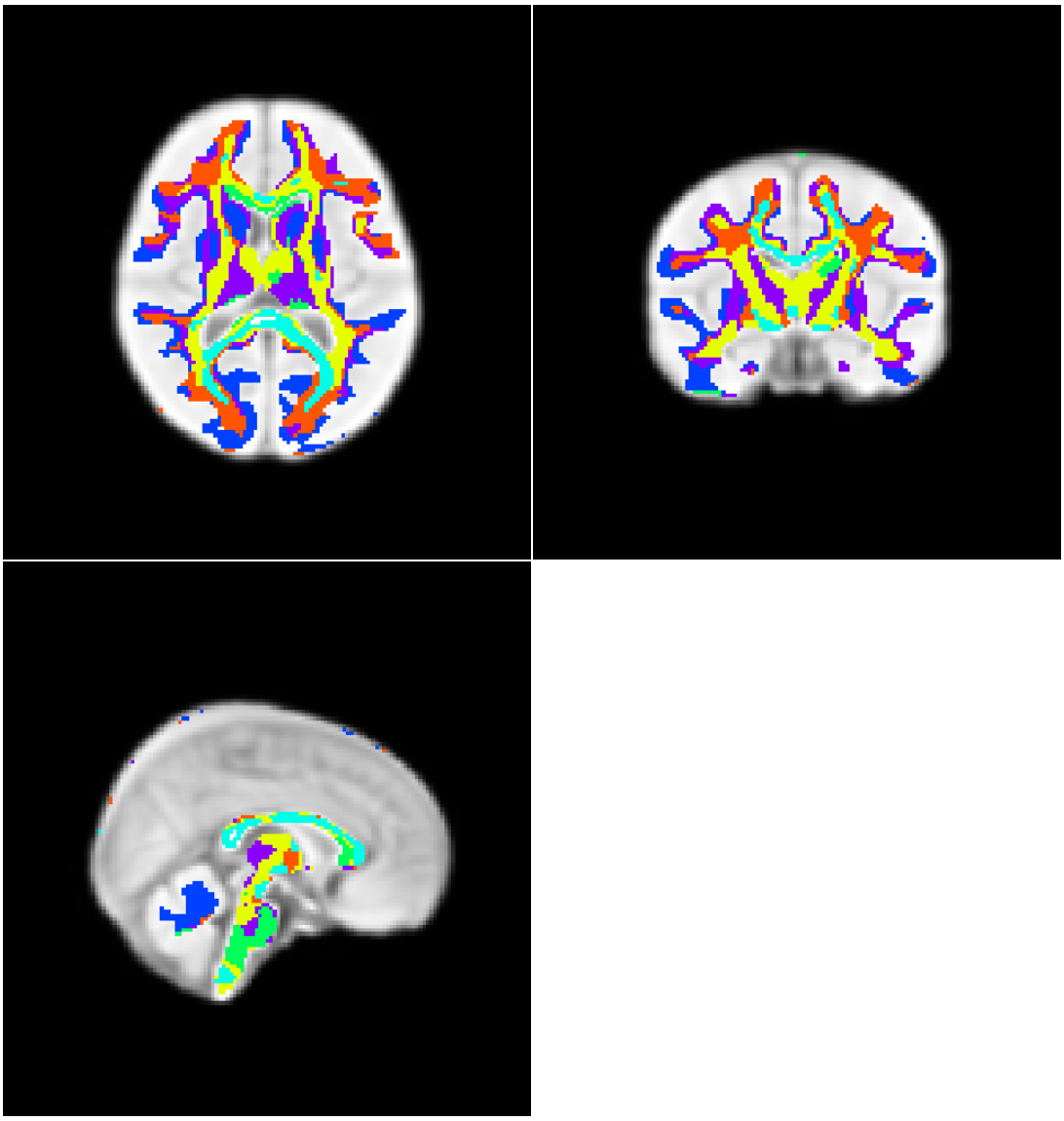

Figure 9. Clusters defined by k-means clustering of NDI and ODI with k=6.

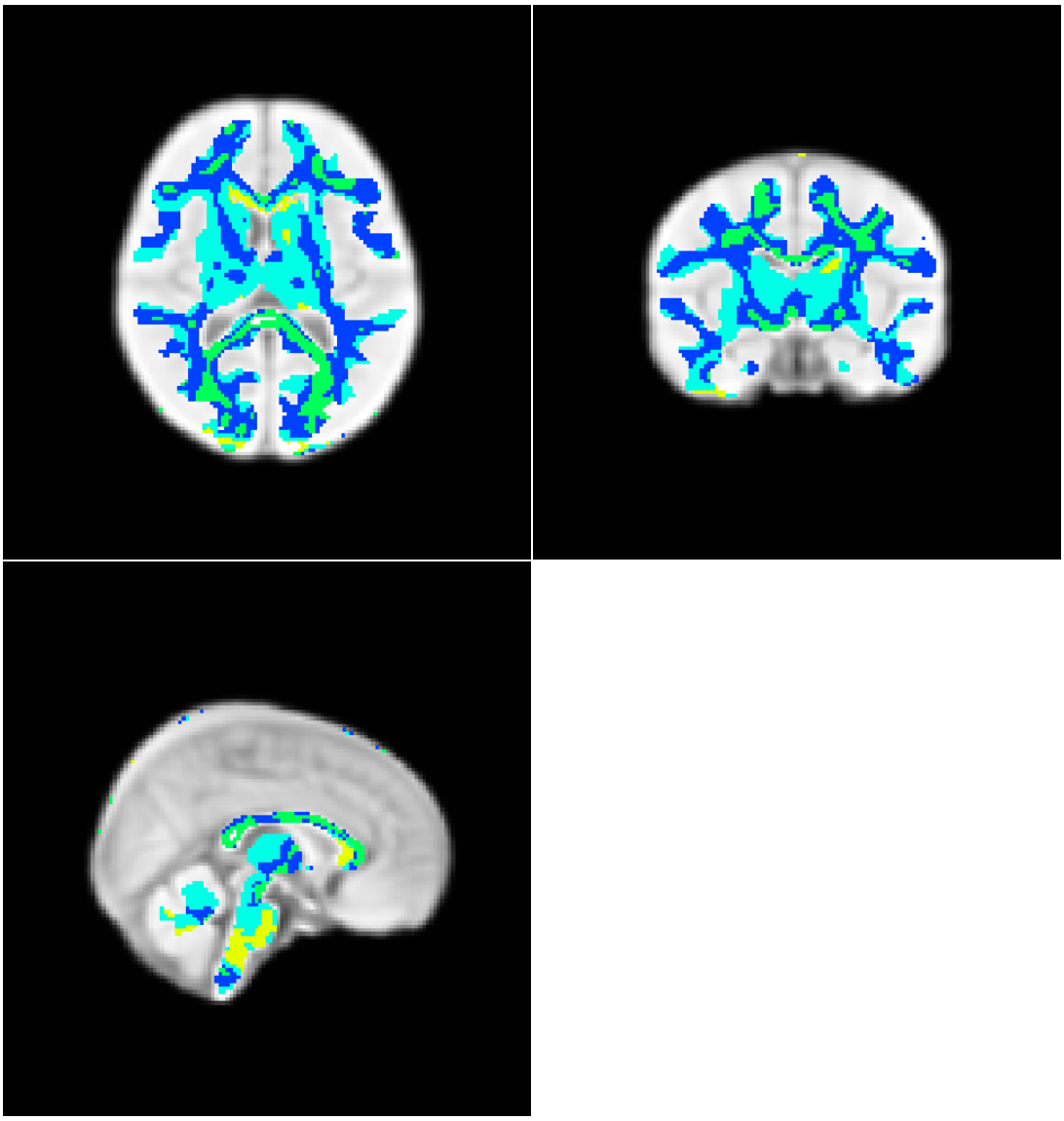

Figure 10. Clusters defined by k-means clustering of only NDI with k=4.

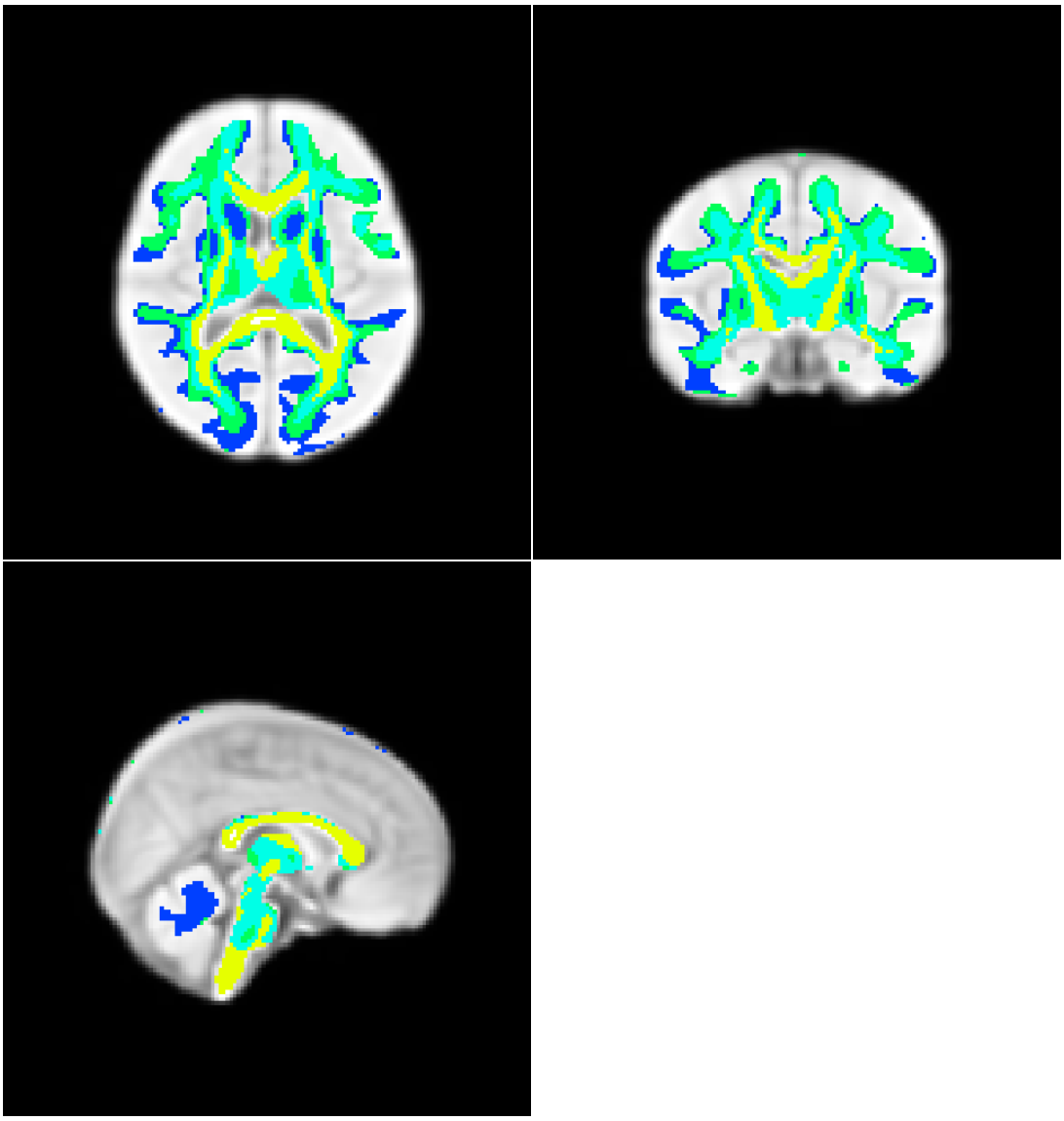

Figure 11. Clusters defined by k-means clustering of only ODI with k=4.

3.4 Discussion

Our results demonstrate a linear increase of neurite density in white matter tracts and subcortical grey matter regions during late childhood; all regions demonstrate stable ODI, suggesting that white matter and grey matter changes during this age are dominated by

increases in myelination or axonal packing, rather than changes in geometry or dispersion of neurons. These results provide further evidence of neurite density and orientation dispersion changes during late childhood by using individual white matter tracts (rather than grouped) and subcortical grey matter regions. The results are consistent with base knowledge provided by another NODDI study from 7 – 63 years, which grouped white matter tracts in categories (Chang et al. 2015), whereas this study used specific segmented white matter tracts and subcortical grey matter. In addition to using pre-determined regions-of-interest to analyze neurite density and orientation dispersion means, areas of similar development were determined using k-means clustering.

The cingulum and uncinate show the lowest values of NDI of all white matter tracts (excluding the forceps minor). Low values of NDI may indicate late or prolonged development in frontal-temporal connections, as has been found in previous DTI studies (Lebel et al. 2012, Lebel et al. 2008). The CST shows the highest values of NDI, which was found in a previous NODDI study (Chang et al. 2015). Greater neurite density is intuitive with higher FA values because a greater number of axons or myelin should cause higher anisotropic diffusion. However, fibre coherence will also affect FA, which can be explained by orientation dispersion. While the CST does have the highest values of NDI, the CST does not have the highest values of FA. The callosal tracts (forceps major and minor) exhibit the highest values of FA, which is consistent with Lebel et al. (Lebel and Beaulieu 2011). The CST here does have low values of ODI, but the forceps major and minor exhibit even lower ODI values. The dense packing of fibres of the forceps major and minor through the corpus

callosum may explain the low ODI values whereas the CST is a projection pathway connecting the brainstem to the primary motor cortex. The CST may have more myelin, larger axons, or higher density of axons than callosal tracts but greater dispersion of axons causes lower FA values. NDI represents the intra-cellular component of each voxel, which is the volume enclosed by the membranes of myelin. NDI increases are likely due to increases in myelin content, the size of axons, or the number of axons within a voxel. These same physiological factors cause FA to increase during development (Beaulieu 2002), however values of FA are driven by a combination of NDI and ODI which is evident in the results of the CST compared to the callosal tracts. NODDI is able to give more insight to results provided with DTI. It appears that white matter tracts are not changing geometrically due to the lack of significant findings in age-related changes of ODI.

K-means clustering indicated similar development profiles across brain regions. The resulting four clusters using NDI-slope and ODI-mean contain primarily the: (1) posterior of the genu of the corpus callosum and mid-section of the CST, (2) the rest of the corpus callosum, corona radiata, IFO, ILF, (3) first layer of subcortical white matter, cores of the caudate, putamen, and thalamus, cerebellum white matter, and (4) the intermediate layer (the next layer down) in white matter, and the SLF. The posterior of the genu of the corpus callosum and mid-section of CST exhibit negative NDI development rates, while the cluster consisting of the corpus callosum, corona radiata, IFO, and, ILF showed the greatest positive NDI changes, followed by the immediate subcortical white matter. For exploratory purposes, k=6 was also evaluated, as the next elbow point on the SSE curve. With six

clusters, the cingulum appeared distinct from the corpus callosum, and the thalamus is distinctive from the caudate and putamen. This is unsurprising, since NODDI parameters are expected to differ between white and grey matter. The fastest developing cluster group appears to contain the corpus callosum and the forceps major tract, which is consistent with the 4-cluster findings and NODDI development fitting results in this study. The cluster containing the first layer of subcortical white matter of the corona radiata and SLF has the next highest rate of change in NDI. As with 4 clusters, the 6-cluster solution showed a cluster of posterior of the genu of the corpus callosum and mid-section of the CST that exhibits negative rates of change in NDI. The 4-cluster and 6-cluster solutions seem to be driven mostly by mean ODI across subjects rather than rates of change in NDI. The 4-cluster solution using only ODI results in the regions where orientation density progresses from the centre to the periphery of white matter tracts. The first layer of subcortical white matter is most dispersed compared to the middle core of white matter tracts. NDI-slope clustering result in a distinct cluster containing the forceps major, and another containing the genu of the corpus callosum. The other 2 clusters are much larger, the first cluster containing subcortical grey matter and part of the first layer of cortical white matter, and the second cluster containing the intermediate layer, core of white matter tracts and part of the first layer of cortical white matter. The combination of NDI-slope and ODI-mean gives different results than individual parameter clustering, evident as NDI-slopes and ODI-means differ from individual clustering results and the forceps major and minor become better defined in their cluster.

The forceps major exhibited higher values and steeper slope of NDI compared to the forceps minor between 8-13 years. The k-means clustering confirmed a developmental distinction between the posterior section of the genu of the corpus callosum and the rest of the corpus callosum, however the core section actually showed negative development. The growth rate of the forceps major is consistent with other studies showing steeper and larger logarithmic NDI growth in the splenium than the genu of the corpus callosum (Chang et al. 2015) as well as posterior-to-anterior myelination development of the corpus callosum (van der Knaap and Valk 1995). The cingulum and uncinate (excluding the forceps minor) have the lowest NDI values, while the uncinate has the shallowest slope, which is consistent with prolonged development in frontal-temporal connections (Lebel et al. 2012) maturing more slowly during childhood and adolescence (Lebel et al. 2008). The cingulum and uncinate are limbic and association tracts, respectively, which is consistent with a study that found association and limbic tracts exhibit lowest values of NDI, highest ODI, and lowest FA compared to callosal and brain-stem projection tracts (Chang et al. 2015). The SLF and CST showed the steepest rates of change of NDI with age, which appears to be consistent with growth trajectories of FA showing steep changes in the left cortical spinal tract and the SLF (Lebel and Beaulieu 2011).

On average, strong correlations (larger R^2 values) with age were found for NDI compared to DTI parameters (FA, MD, RD, AD). This data suggests that NDI is more sensitive to age-related changes. It is expected that NODDI parameters (NDI, ODI) would better represent microstructural changes than DTI because of its multi-component nature that includes

intra-cellular, extra-cellular and CSF compartments allowing further information to be derived in each voxel thereby reducing the partial volume effect. FA and NDI are sensitive to similar underlying physiological changes, such as myelination and axonal packing; so, similar trends are found in both FA and NDI vs. age. FA has been used often in other studies as a marker of development and white matter integrity (Lochner et al. 2012, Lebel and Beaulieu 2011), and its been shown that changes in FA can be driven by ODI or NDI separately (Eaton-Rosen et al. 2015), positive correlations between NDI and FA, and negative correlations between ODI and FA (Kunz et al. 2014). Our results and previous studies suggest that NODDI and DTI complement each other, however still provide different information.

This study could benefit from additional subjects to provide the power to detect significant age-related relationships in all white and grey matter regions. The addition of longitudinal data and expansion of subject age range would provide greater insight in NODDI developmental changes because longitudinal studies allow changes to be detected within individuals allowing for a more accurate picture of development to be determined. The relationships of DTI and NODDI parameters were only approximated as linear over the small age range of 8-13 years, and the relationships may not be truly linear. DTI parameters have been modeled as Poisson curves, however, it was over a much larger age range (5 to 83 years) (Lebel et al. 2012).

This work further helps characterize healthy white and grey matter development during late childhood and adolescence by implementing NODDI in specific white matter tracts and in subcortical grey matter regions. Similar groups of white matter and subcortical grey matter were separated using k-means clustering during late childhood and adolescence. Modelling of morphology characteristics neuritis allows more information to be collected than DTI. Measurements of NDI and ODI showed regional differences in white matter tracts and subcortical grey matter that likely indicate changes in myelination, axonal sizes, and axonal density.

Chapter Four: **Developmental changes between preschool children and adolescents using ihMT**

4.1 Introduction

White matter contains myelin that forms an insulating layer around axons and facilitates efficient neural connections. White matter provides connectivity in the brain, and the speed of transmission along axons is affected by the diameter of the axon and the thickness of the myelin sheath (Aboitiz et al. 1992). Grey matter mostly contains neuronal cell bodies, and enables sensory perception, muscle control and cognitive capabilities. Myelin is prevalent in white matter, and smaller amounts are also found in grey matter.

Post-mortem studies have shown increases of myelination into adulthood (Benes 1989). *In vivo* data from magnetic resonance imaging (MRI) has shown rapid white matter development from infancy (Dubois et al. 2008) into adulthood (Lebel and Beaulieu 2011) using various MRI techniques including anatomical imaging (ie., T1-weighted), diffusion tensor imaging (DTI), myelin water fraction (MWF) imaging, and magnetization transfer (MT) imaging. With these methods, rapid white matter changes have been shown during infancy (Dubois et al. 2008, Deoni et al. 2011) and continued development has been reported during childhood and into early adulthood (Yoshida et al. 2013, Paus et al. 1999, Leppert et al. 2009, Barkovich et al. 1988, Perrin et al. 2009a). Diffusion imaging is used to make inferences about myelination and white matter integrity (Lochner et al. 2012, Lebel and Beaulieu 2011), since myelin affects water diffusion along and across axons (Song et al. 2003). MT ratio (MTR) from MT imaging can also be used to suggest changes in myelin, though, like DTI measures, it is not specific to myelin (Schmierer 2004, Stanisz 2004, Berry

1999). Many studies use DTI or MT to investigate developmental changes in white matter during childhood, demonstrating significant relationships between age and imaging parameters that suggest myelination (Dubois et al. 2008, Yoshida et al. 2013, Perrin et al. 2009b). However, as FA and MTR are sensitive to multiple processes (ie., unable to differentiate the effects of myelination vs. axonal packing), these reports cannot go further than suggesting myelin is increasing. Neurite orientation dispersion and density imaging (NODDI) is a multi-component model that models neurite (dendrites and axons) morphology (Zhang et al. 2012) to gain more understanding than DTI. Neurite density and orientation dispersion has provided greater inside to measures of FA (Eaton-Rosen et al. 2015, Kunz et al. 2014), development in white matter across a wide age span (7 – 63 years) (Chang et al. 2015), and development focused on late childhood (8-13 years) in both white matter tracts and subcortical grey matter regions in Chapter 3. Neurite density increases during late childhood while orientation dispersion remains stable. MWF imaging uses a T2 multi-component model that includes a myelin-bound water component to give MWF, a more specific measure of myelin. MWF imaging has been used in very young children 3 – 60 months (Deoni et al. 2012), showing exponential growth in the first two years of life, followed by slower gradual growth thereafter.

Inhomogeneous magnetization transfer (ihMT) is an MRI technique able to virtually eliminate signal from unmyelinated tissues. While MT probes all macromolecular components (McGowan 1999), ihMT provides a quantitative measure attributed to motion-restricted lipid chains in membranes that are far more dense in myelinated tissues (Varma

2015), and thus may provide a biomarker specific to myelin. ihMT will allow more specific characterization of white matter and grey matter development, though it has not previously been used to study brain maturation. Specific changes in ihMT in white matter tracts and grey matter regions can provide insight to the regional growth patterns of myelination during childhood and adolescence.

The goal of this study was to use MT and ihMT to study white matter and grey matter changes and myelination during normal childhood and adolescent development. ihMT will allow further characterization of white matter and grey matter development during childhood and adolescence because imaging techniques more specific to myelin have not been used during late childhood to our knowledge. Understanding healthy development can help identify critical periods of maturation, and may ultimately assist with identification and treatment of developmental disorders.

4.2 Methods

4.2.1 Subjects

Data was collected from 43 healthy children (19 aged 2-4 years, 8 F/11 M, mean +/- sd was 3.6 +/- 0.5 years; 23 aged 8-13 years 10 F/13 M, mean +/- sd was 11.2 +/- 1.9 years). The data was separated into two cohorts: young cohort 2-5 years and old cohort 8-13 years. The data from the young cohort was taken from a larger subset of data consisting of 85 participants from 2-5 years. All subjects 2-5 years old with good quality ihMT data were included. The original sample of the old children included 26 subjects, however, 3 subjects

were excluded from the study due to poor quality of ihMT data. Quality checking of the data was performed by manually checking the data and deeming poor quality if there was obvious blurring and ghosting in the images due to subject motion. Exclusion criteria were known diagnosed developmental and reading disorders, undiagnosed reading disorders, history of neurosurgery, and any contraindications to MRI.

4.2.2 MRI acquisition

For the comparison between the young and old cohorts, (ih)MT, diffusion, and T1-weighted images were collected from the subjects. Subjects were scanned on a 3T MR system (Discovery 750w; General Electric, Waukesha, WI) using a 32-channel head coil. Two slightly different protocols were used for the two age groups; there are differences in the resolution, repetition time, echo time, and the resulting scan time.

The (ih)MT sequence collected both ihMT and MT data using a whole brain 3D spoiled gradient echo (SPGR) sequence with a 5 ms Fermi pulse with peak B1 of 45 mG and ±5 kHz offset prior to excitation. In the younger children: TR/TE = 10.18ms/2.04ms, 2.4 mm^3 isotropic resolution, total scan time of 5:04 min:sec. In the old children: TR/TE = 10.46ms/2.176ms, 2.2 mm^3 isotropic resolution, scan time of 5:12 min:sec. The protocols were set up separately irrespective of each other.

Diffusion data was acquired using spin echo EPI, 2.2 mm^3 isotropic resolution, 30 directions for each non-zero b-shell; for younger children: b=750 s/mm^2, 5 b=0 s/mm^2,

scan time = 4:03 min:sec; for old children: b=900 s/mm^2, 5 b=0 s/mm^2, scan time 7:12 min:sec. All data was good quality. A higher b-value allows for greater sensitivity to be detected in the diffusion MR data (Jones 1999). Diffusivity decreases with age during development and peaks during adulthood in white matter (Lebel et al. 2012), so a lower b-value is suitable for the younger children.

T1-weighted anatomical images for the young children were acquired with the following parameters: 0.9 mm^3 isotropic resolution, TI = 600 ms, TR/TE = 8.228/3.76 ms, scan time = 4:25 min:sec. T1-weighted anatomical images for the old children were acquired with the following parameters: 0.8 mm^3 isotropic resolution, TR/TE = 8.208/3.156 ms, scan time = 5:38 min:sec. T1-weighted images were used as high resolution references images for intra- and inter-subject registration, and they are necessary to segment grey matter structures using FreeSurfer and required as anatomical priors for probabilistic tractography using FreeSurfer's TRACULA.

4.2.3 Image analysis

(ih)MT data were processed to compute qMT and qihMT maps. Quantification of (ih)MT used inverse subtraction methods and a high tip angle reference scan. With an SPGR sequence in the short TR and low-tip regime, the difference in longitudinal relaxation rates observed with different MT pulse conditions was approximated by $\Delta(R_1^*)$, as shown in Equation 11:

$$\Delta(R_1^*) = \frac{C\alpha^2}{2T_R} S_C \Delta\left(\frac{1}{S^*}\right) \quad (11)$$

In Equation 11, R_1* is the longitudinal relaxation rate during a particular MT state; S* is the measured signal during this state. C is the flip angle scale factor for the high tip angle reference (C = 4), α is the flip angle (α = 8°), and S_c is the measured reference signal. In conventional MT, $\Delta(R_1^*)$ and $\Delta(1/S^*)$ are the rate and inverse signal differences, respectively, when an off-resonant pulse is applied vs. when no pulse is applied. In ihMT, the differences are between conditions with single-frequency off-resonant pulses applied at ±5 kHz, and dual-frequency off-resonant pulses with power split between +5 kHz and -5 kHz. The rate differential in Equation 11 provides a simple, quantitative measure correlated to the concentration of the targeted pool (i.e., all macromolecular content or myelin).

4.2.4 Regions-of-interest

T1-weighted and diffusion data were processed in FreeSurfer (Reuter et al. 2012, Yendiki et al. 2011) to obtain automatically segmented subcortical grey matter structures and white matter tracts. These grey and white matter regions served as volumes-of-interest to obtain mean values of ihMT, DTI, and NODDI output parameters.

Subcortical grey matter regions segmented were the amygdala, caudate, hippocampus, pallidum, putamen, and thalamus (Figure 12).

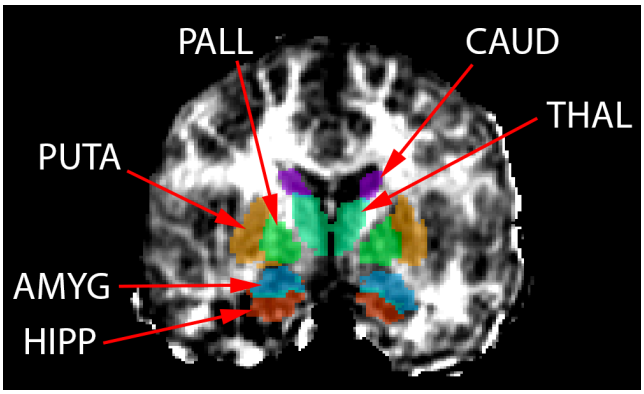

Figure 12. Grey matter regions segmented by FreeSurfer. Amygdala (AMYG), caudate (CAUD), hippocampus (HIPP), pallidum (PALL), putamen (PUTA), thalamus (THAL)

White matter tracts delineated were the anterior thalamic radiation (ATR), cingulum, cortical spinal tract (CST), forceps major & minor, inferior longitudinal (ILF), superior longitudinal (SLF), and uncinate fasciculi (Figure 13).

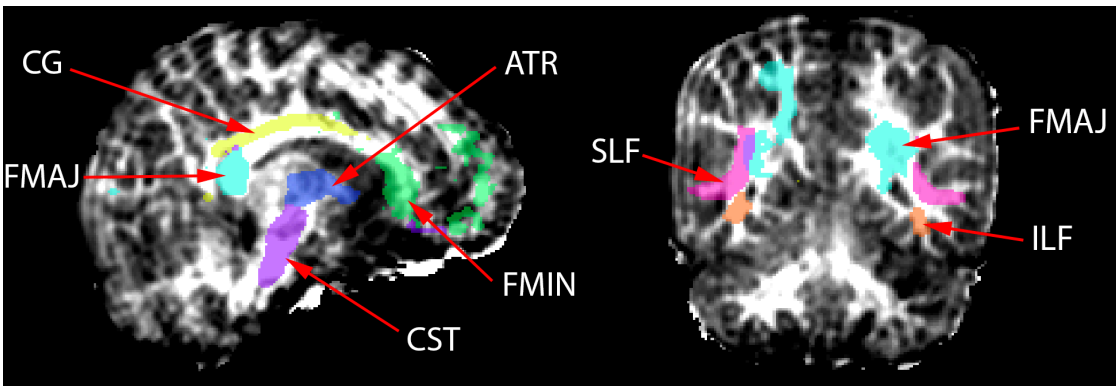

Figure 13. White matter tracts delineated by FreeSurfer. Anterior thalamic radiation (ATR), cingulum (CG), cortical spinal tract (CST), forceps major & minor (FMAJ, FMIN), inferior longitudinal (ILF), superior longitudinal (SLF), and uncinate fasciculi (UNC)

Mean qMT and qihMT were calculated for each region for each subject. The two groups were compared using independent-sample t-tests. False discovery rate was used to correct for multiple comparisons. Differences between groups were characterized by $\Delta q(ih)MT$ (Equation 12).

$$\Delta q(ih)MT = \frac{q(ih)MT_{older} - q(ih)MT_{young}}{q(ih)MT_{young}} \times 100 \quad (12)$$

Linear models using a first-degree polynomial were used to fit qMT and qihMT with respect to age.

4.2.5 Registration

Advanced Normalization Tools (ANTs) (Avants et al. 2011) was used to normalize each subject's diffusion b0 and MTR images to their respective T1-weighted image. Grey matter regions were segmented in T1-weighted space, while white matter tracts were segmented in diffusion space. White matter tracts, as binary masks, were warped to T1-weighted space, as were the qMT and qihMT maps. qMT and qihMT means in each white and grey matter mask were calculated in T1-weighted space.

4.3 Results

Figure 14 shows sample axial images of qMT and qihMT maps from a 9-year-old boy. Signal intensity in the images is related to myelin concentration (qihMT), and all macromolecular contributions (qMT).

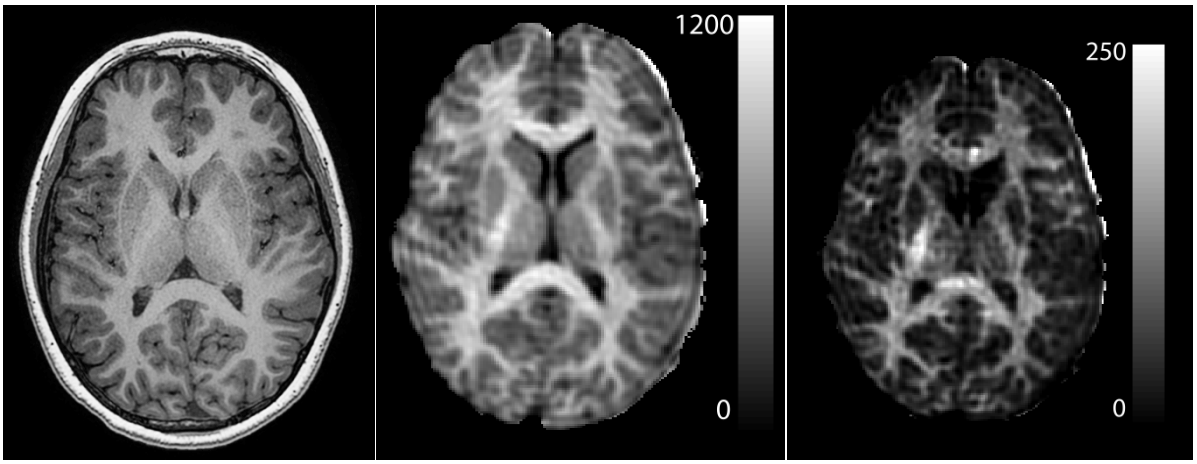

Figure 14. Typical T1-weighted (left), qMT (middle), and qihMT (right) images from a 9-year-old.

Measures of qMT were significantly higher in the old group in the white matter regions of the ATR, cingulum, forceps major, forceps minor, ILF, SLF, and uncinate (Figure 15). Gray matter regions did not exhibit any significant group differences in qMT. Significantly higher values of qihMT in the old group were found in the putamen in grey matter, and in the ATR, cingulum, forceps major, forceps minor, ILF, SLF, and uncinate in white matter (Figure 16). The average difference (Table 9) of qMT (as calculated by Equation 12) across all white matter tracts was 10.7%, and across all grey matter regions was 2.06%. Average group differences of qihMT were 24.8%, and 19.8% for white and grey matter, respectively.

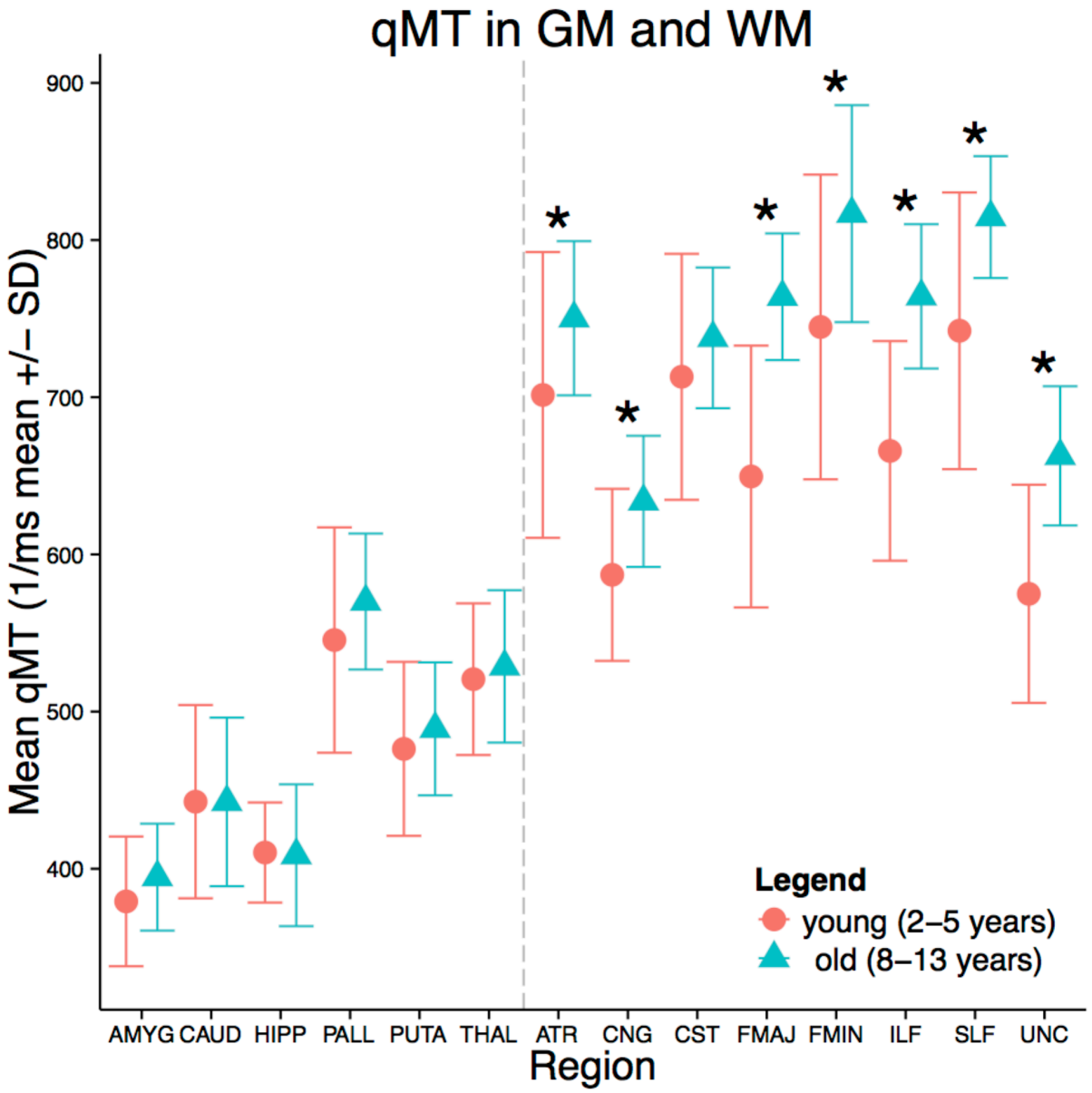

Figure 15. qMT in grey and white matter regions. Asterisks indicate p<0.05 from t-tests.

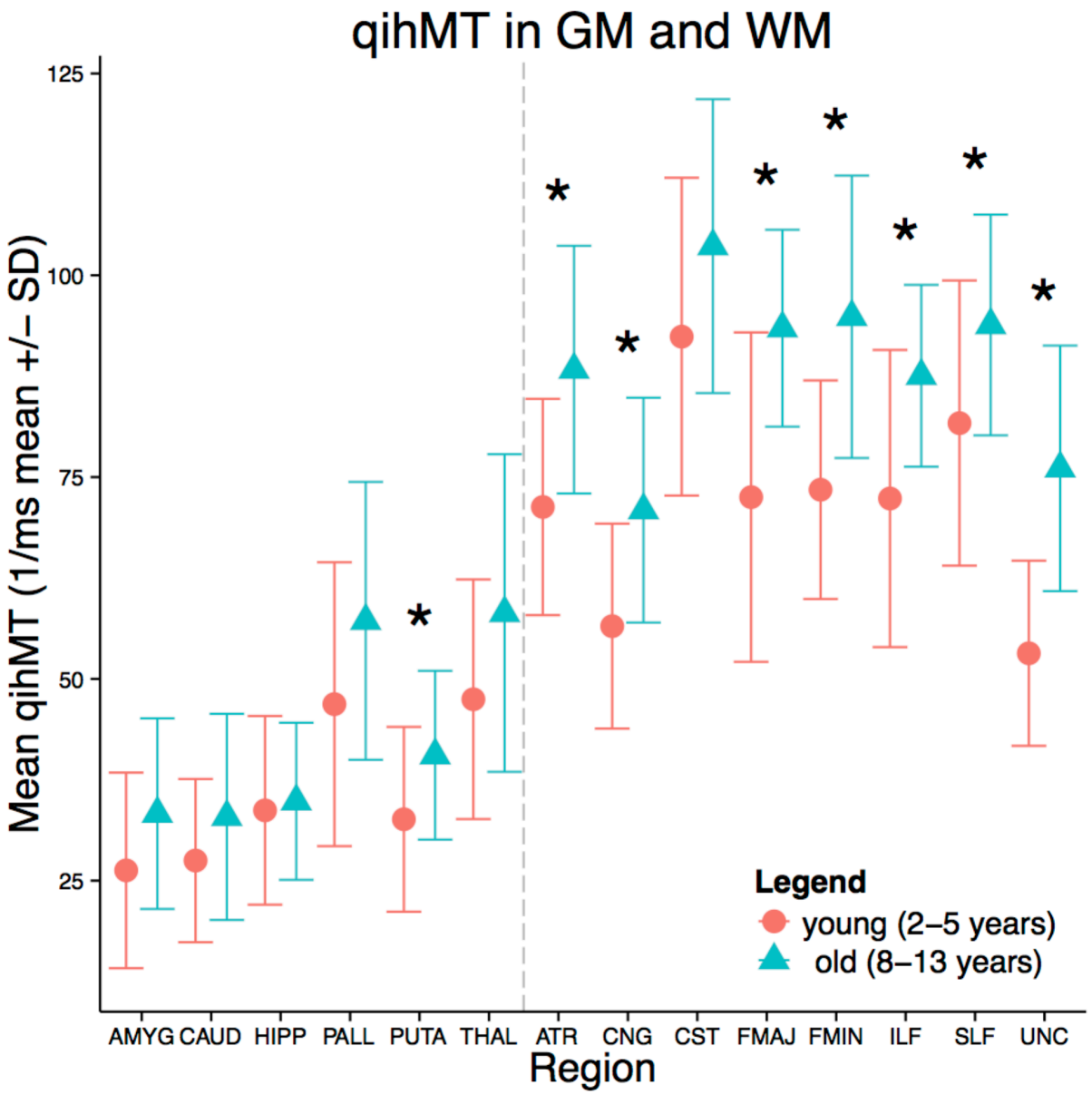

Figure 16. qihMT in grey and white matter regions. Asterisks indicate p<0.05 from t-tests.

Table 9. Percent differences in qMT and qihMT in each grey and white matter region. Asterisks indicate p<0.05 from t-tests. The differences were calculated as the difference divided by the measure in the young cohort (Equation 12).

Region	ΔqMT (%)	$\Delta qihMT$ (%)
Amygdala	4.07	26.8
Caudate	-0.04	19.7
Hippocampus	-0.42	3.32
Pallidum	4.49	22.0
Putamen	2.67	24.3*
Thalamus	1.56	22.5
ATR	6.96*	23.9*
Cingulum	7.96*	25.4*
CST	3.47	12.1
Forceps major	17.6*	28.9*
Forceps minor	9.68*	29.2*
ILF	14.8*	21.0*
SLF	9.74*	14.9*
Uncinate	15.3*	43.1*

4.3.1 Age analysis

No significant correlations were observed between qMT or qihMT and age within each group separately. Plots of the results for qMT and qihMT can be found in Appendix C. To achieve 80% power to detect correlations in the old cohort, the required number of subjects ranges from 53-122, depending on the region and measure.

4.4 Discussion

4.4.1 Group differences

Significant differences between age groups were found in qMT and qihMT, suggesting developmental changes between early and late childhood. qMT and qihMT quantify $\Delta(R_1^*)$ due to the exchange of magnetization from the macromolecular pool. qMT has greater magnitudes because it encompasses all macromolecules, while qihMT is more specific to a restricted pool of macromolecules. Although less myelin is present in grey matter, both white and grey matter changes indicate ongoing myelination between groups. Because qihMT is a measure specifically sensitive to myelin, its changes suggest DTI-observed changes during development are, at least in part, due to myelination.

qihMT provides different contrast than qMT , as evidenced by the CST, which showed the highest qihMT measure of all regions; however, it does not have the highest qMT signal. qihMT should provide similar but different information than qMT because qihMT is sensitive to a restricted portion of macromolecules while qMT is sensitive to all macromolecules. Results of qMT and qihMT in the CST are in agreement with NDI results from Chapter 3, which showed that the CST has the highest NDI values compared to other regions. The CST is concentrated with myelinated axons that connect the brain to the rest of the body, which may contribute to greater values of qihMT. The forceps minor and forceps major exhibited similar differences of qihMT (ΔqihMT_FMIN = 29.2%, ΔqihMT_FMAJ = 28.9%), but did not have similar differences of qMT (ΔqMT_FMIN = 9.7%, ΔqihMT_FMAJ = 17.6%). Changes in myelination may be similar between time points, but

other ongoing development may cause differences in the qMT measure. Differences in qMT may arise from the differences in composition between the genu and splenium of the corpus callosum with thinner axons found in the genu (Aboitiz et al. 1992). The cingulum and uncinate exhibited some of the greater changes in qihMT (ΔqihMT_CNG = 25.4%, ΔqihMT_UNC = 43.1%) suggesting prolonged development in these areas, consistent with other studies (Lebel and Beaulieu 2011, Westlye et al. 2010).

4.4.2 Age analysis

Previous MT studies have revealed mean MTR followed a mono-exponential function with rapid increases in the first 2 years of life before reaching an asymptote from 2 to 15 years (van Buchem et al. 2001) (Engelbrecht et al. 1998), and possibly slight decreases during adolescence (Perrin et al. 2009a). Possible mechanisms underlying these observations include changes in axon density that may affect MTR values in each voxel (ie. lower density could lead to a decline in MTR) (Perrin et al. 2009a) and sexual dimorphism in white matter development of myelin and axonal caliber may override the capability of finding correlations of MTR with age because of sex-differentiated effects. While MTR has been used as a quantitative indicator of demyelination and remyelination in mice (Zaaraoui et al. 2008), qMT and qihMT may not be sensitive enough to capture age-related changes in myelin during childhood development in a short time period or with a small sample size. It is evident that qMT and qihMT is significantly higher in most white matter tracts in the old group; however, relationships with age are not evident within each group. Sensitivity of qihMT to myelin changes during development is unknown; data from the missing time

period of 5 to 8 years may be necessary or changes in qihMT are too subtle for the number of subjects in this study.

4.4.3 Limitations

Quantitative maps of qihMT inherently have less signal-to-noise ratio (SNR) than qMT because qihMT is sensitive to a smaller portion of macromolecules, making it harder to detect differences. Another limitation of the study is the small sample size; up to 122 subjects would be necessary have 80% power of finding a linear relationship between qMT or qihMT and age in the 8-13 years olds, based on the data here.

4.5 Conclusion

qMT and qihMT show regional group differences in white and grey matter regions between early and late childhood. Whereas previous reports using DTI or MTR measures were suggestive of myelination, the specificity of qihMT to myelin provides *in vivo* evidence of myelination occurring across this age range. In conclusion, qMT and qihMT provide unique information about white and grey matter development during childhood that may be used to more specifically understand the physiological processes occurring during this time.

Chapter Five: **Myelin water fraction and g-ratio measurements during brain development**

5.1 Introduction

Myelin forms an insulating layer around axons of neurons, and is necessary to facilitate healthy, efficient connections, especially during brain development. Neural signals propagate along axons that allow for communication within, to, and from the brain. The myelin sheath that forms around axons is a di-electric material that allows for greater conduction speeds of signal along the axon.

The g-ratio is a property of white matter defined as the inner diameter (d) of the myelin sheath divided by the outer diameter (D): $g = d/D$. It can also be calculated using the myelin volume fraction (MVF) and fibre volume fraction (FVF): $g = \sqrt{1 - MVF/FVF}$ (Stikov et al. 2011). The g-ratio provides important information about structures affecting the speed of transmission along the axon (Aboitiz et al. 1992); optimal g-ratios of approximately 0.6 allow for maximum conduction speeds (Rushton 1951). G-ratios have been shown to be higher in patients than in healthy controls; for example, lesions due to multiple sclerosis have shown elevated g-ratios because of demyelination (Stikov et al. 2015).

Myelination begins during gestation, and myelin is visible in the posterior limb of the internal capsule, corona radiata, and coronal spinal tracts as early as 36 weeks of gestation (Counsell et al. 2002). However, there is still little myelin content in the brain at birth, and

most myelination occurs postnatally, along with neuronal growth and a decrease in brain total water content (Holland et al. 1986)

Magnetic resonance imaging (MRI) allows for quantitative *in vivo* assessment of brain white matter maturation, such as changes in myelin water fraction (MWF) and g-ratio. MR diffusion has been used to track brain development based on changes in fractional anisotropy (FA), which may be attributed to myelination, axonal packing or fibre coherence. Multi-component driven equilibrium single pulse observation of T1 and T2 (mcDESPOT) is an MRI technique that can derive myelin water fraction (MWF) maps (Deoni, Matthews, and Kolind 2013). It is a multi-component model that fits the T2 signal to 3 different compartments: myelin water, intra/extra-cellular water, and isotropic water. Neurite orientation dispersion and density imaging (NODDI) uses MR diffusion images to model diffusion in 3 different compartments: intra-cellular water, extra-cellular water and isotropic water (Zhang et al. 2012). NODDI outputs include a neurite density index (NDI) and orientation dispersion index (ODI) to describe neurite (dendrites and axons) morphology. The combination of output parameters from mcDESPOT and NODDI provides MVF (or MWF) and FVF necessary to calculate the g-ratio, as follows:

$$FVF = MWF + (1 - MWF)(1 - v_{iso})(v_{ic})$$

$$g = \sqrt{1 - MWF/FVF}$$

Mean g-ratio values can give insights into how myelination and conduction speeds change over development on a micron-scale, and can contribute to a more detailed understanding of white matter structural development. As brain maturation trajectories can be a sensitive marker of abnormalities (Giedd et al. 2008), the information provided by this research may be useful for identifying altered trajectories in developmental disorders.

5.2 Methods

5.2.1 Subject demographics

mcDESPOT and diffusion data was collected from 13 healthy subjects (4 F, 9 M) aged 8-13 years (mean +/- sd was 11.5 +/- 1.8 years) at the Alberta Children's Hospital (ACH). Exclusion criteria were known diagnosed developmental and reading disorders, undiagnosed reading disorders, history of neurosurgery, and any contraindications to MRI.

Processed mcDESPOT and NODDI data from Brown University was also available for 18 subjects (5 F, 13 M) aged 0-7 years (mean +/- sd was 2.54 +/- 2.52 years). These subjects were included based on birth occurring at 37-42 weeks gestation, no family history of neurological or psychiatric disorders, and no reported incidents of neurological events or disorders. There is no overlap of ages between the data from Brown and the ACH.

5.2.2 MRI acquisition

MRI data was collected at the ACH on the 3T MR system (Discovery 750w; General Electric; Waukesha, WI) using a 32-channel head coil.

The mcDESPOT protocol involved the acquisition of SPGR (spoiled gradient), IR-SPGR (inversion recovery spoiled gradient) and bSSFP (balanced steady state free precession) images. A multi-flip angle SPGR sequence was acquired with TR/TE = minimum + 0.1 ms/min full, 1.7 mm slice thickness, 1.72 x 0.86 mm resolution, scan time = 7:06 min:sec, max flip angle = 18°. The IR-SPGR sequence was acquired with TR/TE = minimum + 0.1 ms/min full, 3.4 mm slice thickness, 2.29 x 0.86 mm resolution, scan time = 0:59 min:sec, flip angle = 5°. Two sets of bSSFP images were acquired, one with a phase of 180° and the other with a phase of 0°; otherwise, each multi-flip angle bSSFP sequence was acquired with TR/TE = minimum + 0.1 ms, 1.7 mm slice thickness, 1.72 x 0.86 mm resolution, scan time = 4:15 min:sec, max flip angle = 60°.

Diffusion weighted images were acquired with spin echo EPI, TR/TE = 12s/88ms, 2.2 mm^3 isotropic resolution, scan time = 14:24 min:sec. 10 volumes were acquired with b = 0 s/mm^2, and two non-zero b-shells were acquired, each with 30 directions: b = 900, 2000 s/mm^2.

MRI data was collected at Brown University on a Siemens Tim Trio scanner with an 8-channel head coil. There are 5 different sets of parameters used for the MRI acquisition depending on the age of the subject. The MRI acquisition parameters are available in Appendix D. Different sets of parameters were developed to use appropriate field-of-view parameters because head sizes rapidly change during early childhood, and lower noise

levels (< 60 dB) were chosen for young infants while noise levels were higher in the older children (< 90 dB) (Deoni et al. 2012).

5.2.3 Image analysis

The SPGR, IR-SPGR, and bSSFP images were first aligned to the SPGR image with the greatest flip angle. The data was processed using a mcDESPOT executable provided by Deoni that fits T1, T2, volume fractions to 3 compartments (myelin-bound, intra/extracellular, and free water), and the exchange between the myelin-bound and intra/extracellular water (Deoni, Matthews, and Kolind 2013). The volume fraction of the myelin-bound water is used as the MWF map.

The diffusion data was used to fit to the NODDI model, using the NODDI Matlab Toolbox (http://www.nitrc.org/projects/noddi_toolbox) and the following equation (Zhang et al. 2012):

$$A = (1 - v_{iso})(v_{ic}A_{ic} + (1 - v_{ic})A_{ec}) + v_{iso}A_{iso},$$

The measured diffusion signal, A, is fitted to the 3 compartments' volume fraction (v) and signal (A) (ic: intra-cellular, ec: extra-cellular, iso: CSF). Here, NDI (fibre volume fraction) refers to $(1 - v_{iso})v_{ic}$ in the model equation. ODI (orientation density index) is obtained from the following equation (Zhang et al. 2012):

$$ODI = \frac{2}{\pi}\tan^{-1}\frac{1}{\kappa}$$

κ characterizes a Watson distribution resulting in $0 \leq ODI \leq 1$, and higher values indicate high dispersion.

Advanced Normalization Tools (ANTs) (Avants et al. 2011) was used to perform non-linear registration from subjects' SPGR-reference images to a study template (Deoni et al. 2012) to analyze MWF and g-ratio in a common space. FSL's FLIRT (Jenkinson and Smith 2001, Jenkinson et al. 2002) was used to initialize the registration. The study template was created from subjects in age groups from 3-144 months by Deoni et al (Deoni et al. 2012). Linear registration in ANTs was used to normalize each subject's diffusion b0 to their respective SPGR-reference image. The MWF and FVF maps were calculated in SPGR-reference space before being registered to the study template.

MNI152 white matter regions were used as volumes of interest. Masks of white matter were obtained from the MNI structural atlas for frontal, occipital, parietal, temporal and cerebellar lobes (Mazziotta et al. 2001). White matter tract masks were obtained from the John Hopkins University DT-MRI white matter atlas for the genu, body and splenium of the corpus callosum, cingulum, corona radiata, internal capsule and optic radiation (Oishi et al. 2009, Mori et al. 2008). The white matter masks were transformed to the study template space.

Mean MWF and g-ratio were extracted in each white matter mask in the study template space. A linear model using a first-degree polynomial was used in each region to fit MWF and g-ratio vs. age ($MWF(age) = A * \ln(\text{age}) + \text{B}$). The natural logarithmic was applied to the age values prior to linear regression. Rapid increases during early childhood of MWF have been characterized by logarithmic curves (Deoni et al. 2012). A linear mixed-effects model was then used to account for the two sites of image acquisition: $MWF(age) \sim \ln(age) + (1|site)$. The difference in the y-intercepts (age = 0) between the sites was used to shift data points from ACH. The data was re-fit with a linear model using the adjusted data, and the resulting coefficients were applied to obtain an adjusted logarithmic curve. The g-ratio data was fit using the same steps.

5.3 Results

Linear models resulted in significant positive correlations of MWF and age in all regions-of-interest (Table 10, Figure 17). Linear models resulted in significant negative correlations of g-ratio and age in all regions-of-interest (Table 11, Figure 18). MWF of the cingulum (A = 0.0444/year, B = 0.0552, $p < 0.001$) increases slower than the other white matter regions, except the occipital lobe (A = 0.0425/year, B = 0.0653, $p < 0.001$), and has the lowest values of MWF throughout the time period. The g-ratio of the cingulum (A = -0.0402/year, B = 0.940, $p < 0.001$) also exhibited highest values compared to the other white matter regions. The greatest rates of change and highest values of MWF were observed in corona radiata (A = 0.0624/year, B = 0.0883, $p < 0.001$) and genu of the corpus callosum (A = 0.0687/year, B = 0.0821, $p < 0.001$). The greatest rates of change and lowest values of the g-ratio were

observed in the optic radiations ($A = -0.0493$/year, $B = 0.906$, $p < 0.001$) and the genu of the corpus callosum ($A = -0.0552$, $B = 0.918$, $p < 0.001$).

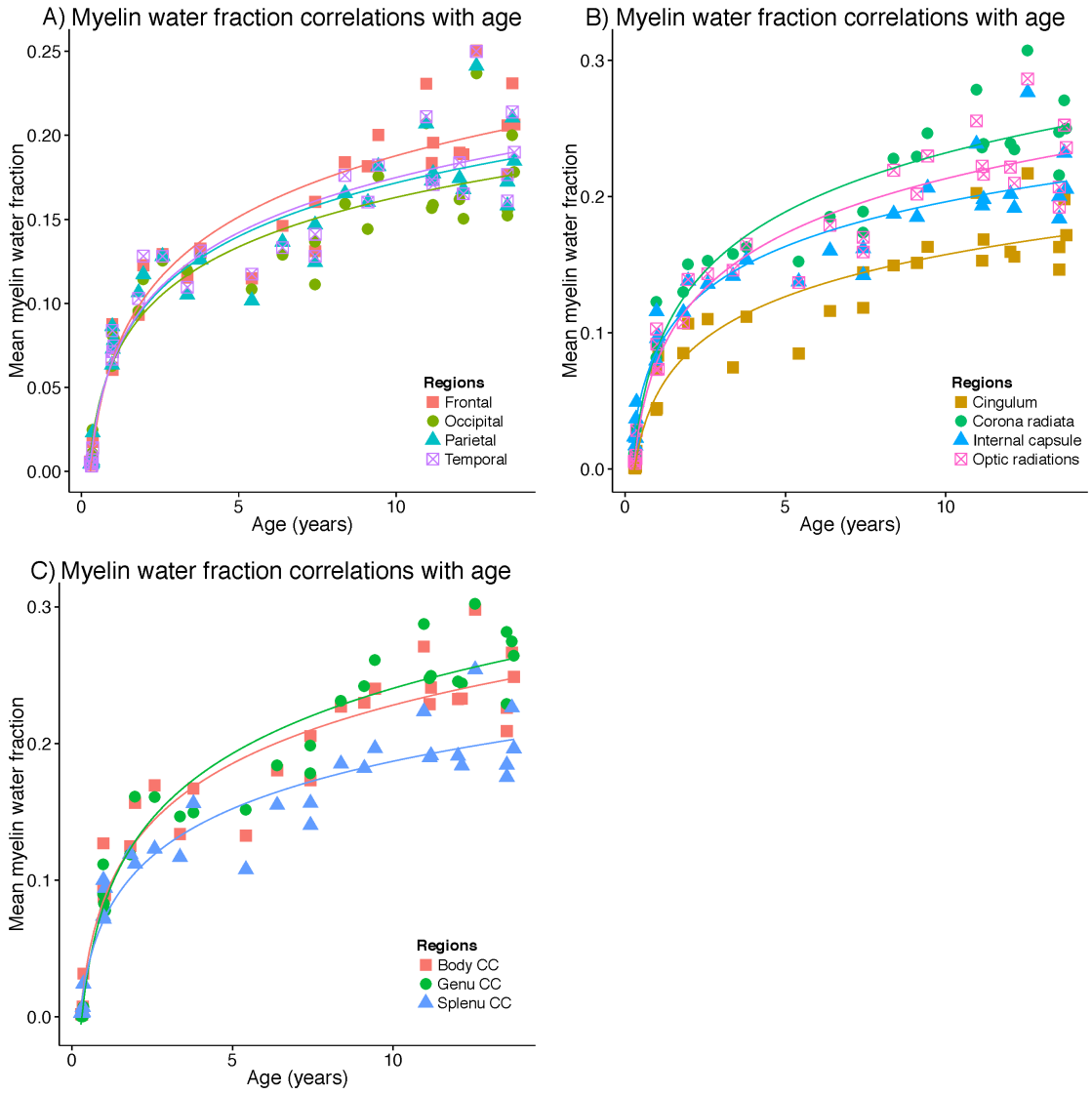

Figure 17. A, B & C: Myelin water fraction trajectories (using parameters from the linear model after adjustment using a mixed-effects model) in white matter volumes-of-interest determined by MNI152 regions. Logarithmic fits are plotted. A: white matter lobes, B: white matter tracts, C: parts of the corpus callosum (CC)

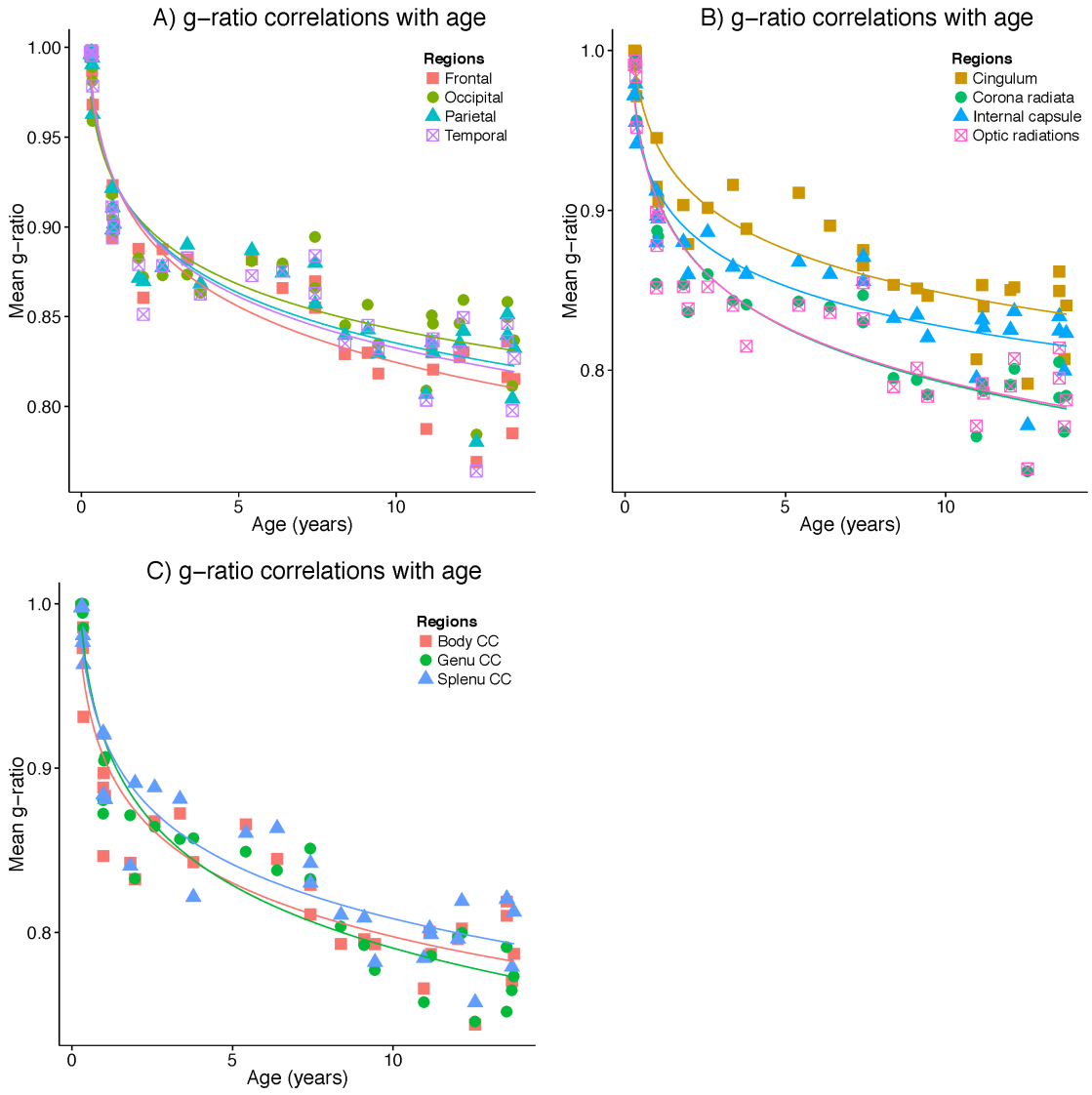

Figure 18. A, B & C: g-ratio trajectories (using parameters from the linear model after adjustment using a mixed-effects model) in white matter volumes-of-interest determined by MNI152 regions. Logarithmic fits are plotted. A: white matter lobes, B: white matter tracts, C: parts of the corpus callosum (CC)

Table 10. R^2 and p values from each MWF linear fit in white matter regions after linearization and adjustment using a mixed-effects model for sites. Fits before the data was adjusted were also significant ($p < 0.001$). CC = corpus callosum

Region	Slope, A ($years^{-1}$)	Y-intercept, B	R^2	p
Frontal	0.0524	0.0671	0.931	<0.001
Occipital	0.0425	0.0653	0.886	<0.001
Parietal	0.0459	0.066	0.909	<0.001
Temporal	0.0473	0.0661	0.910	<0.001
Cingulum	0.0444	0.0552	0.900	<0.001
Corona radiata	0.0624	0.0883	0.940	<0.001
Internal capsule	0.0472	0.0875	0.904	<0.001
Optic radiations	0.0581	0.0795	0.931	<0.001
Body CC	0.0616	0.0861	0.926	<0.001
Genu CC	0.0687	0.0821	0.947	<0.001
Splenu CC	0.0501	0.0716	0.918	<0.001

Table 11. R^2 and p values from each g-ratio linear fit in white matter regions after linearization and adjustment using a mixed-effects model for sites. Fits before the data was adjusted were also significant ($p < 0.001$). CC = corpus callosum

Region	Slope, A ($years^{-1}$)	Y-intercept, B	R^2	p
Frontal	-0.0448	0.928	0.901	<0.001
Occipital	-0.0363	0.926	0.840	<0.001
Parietal	-0.0401	0.928	0.874	<0.001
Temporal	-0.0413	0.928	0.849	<0.001
Cingulum	-0.0402	0.94	0.878	<0.001
Corona radiata	-0.0501	0.907	0.898	<0.001
Internal capsule	-0.037	0.912	0.878	<0.001
Optic radiations	-0.0493	0.906	0.881	<0.001
Body CC	-0.0471	0.906	0.860	<0.001
Genu CC	-0.0552	0.918	0.917	<0.001
Splenu CC	-0.0477	0.918	0.892	<0.001

5.4 Discussion

MWF shows rapid development from 0-2 years of age followed by slower changes from 2-13 years. This agrees well with a previous study in different children (Deoni et al. 2012) aged 0-5 years, but extends this to show continued, albeit slower, development until 13 years. The MWF in our data reaches values of approximately 0.2 at 13 years, which is roughly 80% of adult MWF values (Deoni 2011); continued changes during adolescence is expected, as observed in post-mortem studies (Benes 1989).

The g-ratio is close to 1 at birth because there are only small amounts of myelin. Myelination occurring during infancy and early childhood leads to a rapid decrease in the g-ratio over the first two years of life. Slower decreases in the g-ratio thereafter likely reflect the slower pace of myelination through the rest of childhood. The g-ratio appears to be decreasing during late childhood (8-13 years) to about 0.8, while the g-ratio in white matter has been measured close to 0.7 in a healthy adult brain (35 years of age) (Stikov et al. 2015), consistent with the expected myelin changes beyond 13 years.

Here, the g-ratio mapping gives a mean g-ratio per voxel. G-ratios are not expected to be constant across axons; axon diameters have been observed to have wide variation (Aboitiz et al. 1992), though axons of similar size may cluster together (Lamantia 1990, Aboitiz et al. 1992) making voxel-level calculations a reasonable approximation. Modeling distributions of axonal diameter within a voxel is possible, but it is not clinically feasible nor desirable

for pediatric research because of the long imaging times (Alexander et al. 2010, Assaf 2008, Zhang et al. 2011).

The splenium of the corpus callosum has higher g-ratio values than the genu, and the MWF of the splenium is lower than the genu. The splenium has a larger FVF, which is consistent with histological reports of larger axon diameters in the splenium (Lamantia 1990, Aboitiz et al. 1992). The splenium also has a lower density of axons than the genu (Aboitiz et al. 1992), which may also contribute to a lower MWF and higher g-ratio.

The cingulum and uncinate had the lowest MWF of the white matter tracts, which is consistent with our previous NODDI results (Chapter 3) showing the lowest neurite density in these tracts. Frontal-temporal connections, such as the cingulum and uncinate, exhibit prolonged development (Lebel et al. 2012) and slower maturation compared to other white matter tracts (Lebel et al. 2008). Low values of MWF may indicate slower development in these limbic and association regions, as much of it will come later in adolescence.

All regions of the corpus callosum show a rapid decline in g-ratio during early development. Aside from the corpus callosum, the optic radiations and corona radiata tracts decrease at the highest rates rate after birth and have the lowest g-ratios during adolescence. These tracts are part of the primary visual and sensorimotor pathways, and these pathways may require greater conduction speeds than the cingulum, which is a

limbic tract. Myelination may occur first and more rapidly in the optic radations and corona radiata because they are part of more primary systems than the cingulum.

Future studies with additional subjects and longitudinal data will be able to further clarify the MWF and g-ratio changes during childhood. Overlapping age ranges should be collected from both sites to acquire a more accurate mixed-effects model. Since the y-intercepts are estimated from each group, there may be more error from the 8-13 year group since they are farther from 0 years.

5.5 Conclusion

This work characterizes myelin changes in white matter during childhood and adolescence and shows that logarithmic models are suitable to describe the trajectories of MWF and g-ratio. Rapid changes in MWF and g-ratio occur in the first 2 years of life, and both exhibit subtle changes thereafter varying across white matter regions. MWF and g-ratio give more insight of the development of myelin, which can help understand regional changes in conduction speeds as the brain develops.

Chapter Six: **Future directions and summary**

6.1 Future directions

The work included in this thesis used data from diffusion tensor imaging (DTI), neurite orientation and dispersion density imaging (NODDI), inhomogeneous magnetization transfer (ihMT), and multi-component driven equilibrium single pulse observation of T1 and T2 (mcDESPOT) resulting in measures of fractional anisotropy (FA), diffusivity, neurite density index (NDI), orientation density index (ODI), fibre volume fraction (FVF), quantitative MT (qMT), quantitative ihMT (qihMT), myelin water fraction (MWF), and g-ratio. FA, NDI, and ODI reflect the diffusion of water within and around the membranes of the brain, reflecting (to various degress) myelination, axonal packing, axonal coherence, and water content. qMT and qihMT provide measures of the macromolecular pool, and qihMT is more sensitive to the inhomogeneously broadened lines of the macromolecular pool that reflect the amount of myelin within a voxel. MWF is derived from a 3-component model that attributes a fraction of the T2 signal to the component containing myelin water, and MWF serves as a surrogate marker of myelin content. Here, the g-ratio is derived from MWF using mcDESPOT and FVF using NODDI. The g-ratio relates the axon diameter to the diameter of the axon plus the myelin sheath, and is related to the conduction speed of neural impulses along axons. FA, NDI, ODI, FVF, qMT, qihMT, MWF, and g-ratio all reflect white matter microstructure, and can be applied to areas in the subcortical grey matter, which also contain myelin, neuronal cell bodies, and the terminal endings of neurons. These parameters were used to characterize development in white matter tracts and subcortical grey matter in subjects from 0 to 13 years, with a focus on the late childhood portion. This

work provides an in-depth look at how parameters correlate with age during childhood brain development, providing a comprehensive picture of white and grey matter development using various modeling and imaging techniques. All of the parameters used in this work characterize healthy brain development, and the results may be used to compare differences in a patient population, such as those with learning disabilities. Assessing differences between healthy and patient groups may help facilitate early diagnosis, and using the same measured parameters can help evaluate intervention techniques.

Additional MRI data was collected from the subjects aged 8 to 13 years that was not used in this work, though it can facilitate many other studies. T2*-weighted, resting-state functional MRI (fMRI), arterial spin labeling (ASL) images were also collected from 24 out of the 27 subjects scanned. The other children were not able to remain still for the entire duration of the protocol and thus only provided partial data. The T2*-weighted images can be used for quantitative susceptibility mapping (QSM), which allows quantification of susceptibility measures in the brain. Susceptibility measures the magnetic field induced in a material when placed in an external magnetic field. fMRI measures brain activity using the blood-oxygen-level dependent (BOLD) effect. Activity in the brain causes an influx of blood to the activated areas, and the increase in oxygenated blood increases the T2* signal. No stimulus is provided during resting-state fMRI, but brain activity "at rest" can still provide valuable information. ASL magnetically tags blood to image perfusion throughout the brain, which is quantified as cerebral blood flow (CBF). Susceptibility can help describe magnetic properties of white and grey matter. Data from fMRI and ASL can be used on their

own to investigate changes in brain activity and CBF during development, and it may be combined with structural measures from T1-weighted, NODDI, ihMT, and MWF images to better understand the relationship between functional and structural development.

Longitudinal data will be obtained from subjects 2 years after their first scan, slightly extending our age range to 15 years. The expansion of the age range and the addition of longitudinal data will provide greater insight to the developmental changes occurring during late childhood and adolescence, especially because longitudinal data allows changes to be detected within individuals that will capture a more accurate picture of brain development.

Along with the MRI data that was collected for this study, comprehensive standardized cognitive assessments were administered to each subject. Subtests from WASI-II, WIAT-III, and NEPSY-II that cover areas such as matrix reasoning, reading comprehension, math fluency (addition, subtraction, multiplication), phonological processing, and speeded naming were collected. A full list of the cognitive assessment protocol is given in Table 12.

Table 12. List of sub-tests in WASI-II, WIAT-III, and NEPSI-II that compose the full cognitive assessment.

WASI-II	WIAT-III	NEPSY-II
Block design	Early reading skills	Comprehension of instructions
Vocabulary	Reading comprehension	Narrative memory
Matrix reasoning	Math problem solving	Phonological processing
Similarities	Word reading	Speeded naming
	Pseudoword decoding	
	Numerical operations	
	Math fluency - addition	
	Math fluency - subtraction	
	Math fluency - multiplication	

6.2 QSM preliminary data

6.2.1 Introduction

Although magnetic susceptibility can cause unwanted artifacts in an MR image, it provides useful information about magnetic properties of tissues that can be exploited. Ferromagnetic materials, such as iron, exhibit high susceptibility and react strongly when placed in an external magnetic field. These materials induce a strong magnetic field in the direction of the applied magnetic field, which can be evident by movement of iron filings near a permanent magnet. In the brain, molecules in tissues and blood that contain iron are paramagnetic and still induce magnetic fields but to a much smaller degree. Diamagnetic materials, such as myelin, have an opposite effect, inducing a magnetic field in the opposite direction of the applied magnetic field. Quantifying susceptibility can help characterize contributions from iron depositions in tissue, blood oxygenation (Schweser et al. 2011),

and myelin (Liu et al. 2011). However, susceptibility calculations require solving an ill-posed problem.

In one study including 174 healthy subjects from 7 to 83 years and 7 subjects aged 1 to 5 years with cerebral palsy, susceptibility trajectories in white matter tracts, subcortical grey matter, and cortical grey matter were fitted with a Poisson curve (Li et al. 2014), similar to a previous DTI lifespan study (Lebel et al. 2012). A Poisson curve allows different slopes before and after the peak or minima. The QSM curves show decreasing susceptibility until 26 to 45 years of age when susceptibility begins to increase. These minimums occur slightly later than FA peaks and MD minima, which were 23 – 41 years (Lebel et al. 2012). Susceptibility is anisotropic because it depends on the orientation of tract in reference to the main magnetic field, so the orientation of white matter tracts and position of the subject's head will have an effect on the calculated susceptibility (Li et al. 2014). Fibre orientation can be calculated using the susceptibility tensor (Li et al. 2012), but not all methods account for orientation of the subject. Susceptibility in deep grey matter followed an increasing exponential curve, exhibiting rapid development during childhood and plateauing in adulthood (Li et al. 2014). This agrees with increasing iron deposition in tissues in histology (Hallgren 1958).

Preliminary QSM data was available for 20 subjects in our study, so we sought to use this data to measure magnetic susceptibility during late childhood development in white and

grey matter regions to further help characterize susceptibility changes during healthy brain development by extending QSM analysis to white matter.

6.2.2 Methods

T2*-weighted data was collected from 20 subjects (8 F/12 M, mean +/- sd 11.3 +/- 1.9 years).

T2*-weighted images were acquired with an 8-echo train, TR/TE = 56.5/4.508 ms, slice thickness = 1.9 mm, in-plane resolution = 0.9375 x 0.9375 mm^2, and scan time = 5:14 min:sec.

QSM maps used the T2*-weighted data, which were processed by Dr. Armin Eilaghi at the University of Calgary (Eilaghi et al. 2015). Processing included skull stripping followed by 3D phase unwrapping (Jenkinson 2003). QSM processing utilizes phase information, and thus requires phase unwrapping. Phase is measured from $-\pi$ to $+\pi$, but phase is periodic and not bound between $-\pi$ and $+\pi$ in the real world. This causes phase wraparound that needs a tool for phase unwrapping. The contribution of susceptibility from the background, anywhere outside of the brain, needs to be removed; this was accomplished using a technique called regularization enabled sophisticated harmonic artefact reduction of phase data (RESHARP) (Sun 2014). The induced magnetic field in one voxel can be a combined effect from many other voxels, which requires a deconvolution to determine the

susceptibility from a single voxel. The susceptibility distribution is solved using regularized deconvolution (Li, Wu, and Liu 2011).

T1-weighted and diffusion images (b=0, 900 s/mm^2) from each subject was used to generate white matter and grey matter volumes-of interest using FreeSurfer (Reuter et al. 2012, Yendiki et al. 2011). White matter regions delineated were the anterior thalamic radiation (ATR), cingulum, cortical spinal tract (CST), forceps major & minor, inferior longitudinal (ILF), superior longitudinal (SLF), and uncinate fasciculi. Grey matter regions identified were the amygdala, caudate, hippocampus, pallidum, putamen, and thalamus.

FSL's FLIRT (Jenkinson and Smith 2001, Jenkinson et al. 2002) was used to perform linear registration to align QSM data to each subject's T1-weighted image. Advanced Normalization Tools registration (Avants et al. 2011) was used to perform linear registration to align diffusion images to the T1-weighted space. The first echo from the T2*-weighted data and the b0 image from diffusion were used for the intra-subject registration. Once the QSM map was registered in T1-weighted space, white matter and grey matter masks were used to calculate a QSM (measure of susceptibility) mean in each mask.

Linear models using a first-degree polynomial were used to fit QSM in each white and grey matter volume-of-interest with respect to age. False discovery rate was used to correct for multiple comparisons.

6.2.3 Results

No significant linear relationships between QSM and age were present (Table 13, Figure 19). All white matter regions exhibit negative susceptibility, except the cingulum and SLF. All subcortical grey matter regions exhibit positive susceptibilities, except the amygdala and hippocampus.

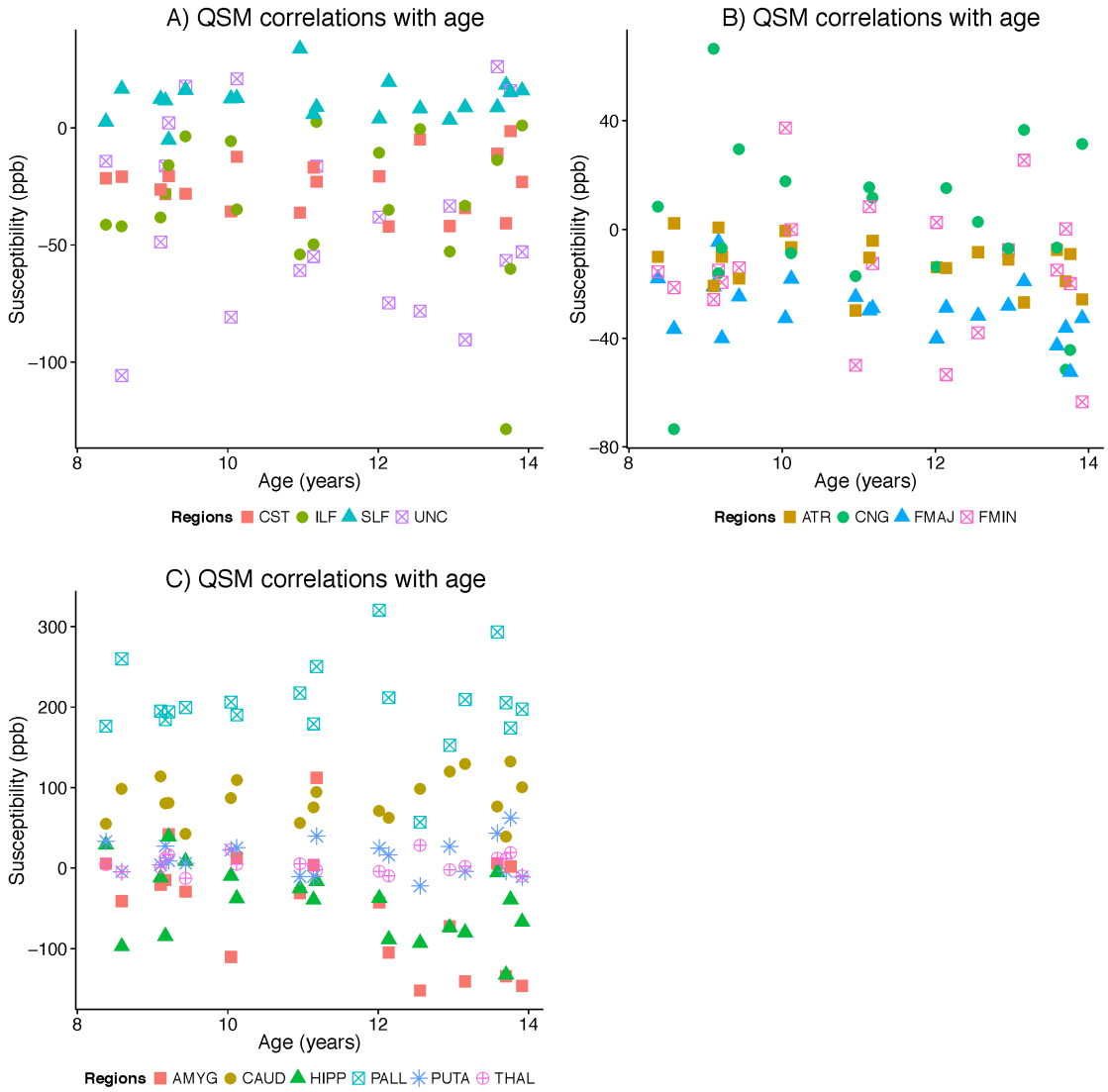

Figure 19. Susceptibility trajectories in white (A, B) and grey (C) matter volumes-of-interest. Significant lines of fit ($p < 0.05$) are plotted on the graphs.

Table 13. Fitting results of linear fits for susceptibility. The p-values were corrected for multiple comparisons using the false discovery rate method.

Region	Slope, m (ppb years^{-1})	Y-intercept, b	R^2	p
ATR	-1.76	7.63	0.14	0.375
Cingulum	-1.32	14.4	0.01	0.956
CST	0.18	-26.5	<0.01	0.956
Forceps major	-2.66	0.39	0.23	0.210
Forceps minor	-1.29	-0.37	0.01	0.956
ILF	-3.03	1.87	0.04	0.956
SLF	0.52	5.68	0.02	0.956
Uncinate	-1.15	-24.1	<0.01	0.956
Amygdala	-16.7	146	0.21	0.210
Caudate	3.20	50.3	0.05	0.956
Hippocampus	-11.1	81.8	0.22	0.210
Pallidum	-0.37	208	<0.01	0.956
Putamen	0.40	9.28	<0.01	0.956
Thalamus	0.43	0.23	0.01	0.956

6.2.4 Discussion

Our results did not demonstrate linear relationships of susceptibility in the white matter tracts or subcortical regions during late childhood. The results do show differences in susceptibilities between regions. Linear decreases would be expected in white matter tracts because susceptibility should decrease as a result of myelination causing the white matter to become more diamagnetic (Argyridis et al. 2013), and has been found in previous results in a QSM study of individuals aged 1 – 83 years (Li et al. 2014).

The orientations of white matter tracts were not accounted for in the analysis. This needs to be further investigated before relative differences between white matter tracts can be

compared. The changes may be approximated as linear because of the small age range studied here, however over a larger age span the relationship may follow nonlinear trajectories. The QSM data would also benefit from increasing the number of subjects to increase the power.

6.3 Thesis summary

This thesis includes 3 studies of white matter and grey matter development through childhood and adolescence. Chapter 3 characterized changes in neurite morphology using NODDI from 8 to 13 years of age. Neurite density index (NDI) and orientation density index (ODI) were the NODDI output parameters used to characterize white matter tracts and subcortical grey matter structures. NDI increases were found in all white matter tracts (ATR, cingulum, cortical spinal tract, fmaj, fmin, ILF, SLF, and uncinate), and in some subcortical grey matter regions (amygdala, hippocampus, palladium, and putamen). Significant linear relationships of ODI vs. age were not found in neither white nor grey matter regions. Chapter 4 focused on ihMT changes between an early childhood group, 2 – 5 years, and a late childhood group, 8 – 13 years. qMT and qihMT are measures sensitive to macromolecules, and qihMT is more sensitive to macromolecules found in the myelin sheath. Increases between cohorts were observed in white matter tracts and subcortical grey matter structures revealing developmental changes that can be captured using ihMT. Chapter 5 used mcDESPOT and NODDI to generate maps of MWF and the g-ratio. MWF begins close to zero at birth, and development causes an increase in MWF following a logarithmic curve and it was found to continually increase from 8 to 13 years of age in

white matter tracts. The g-ratio begins close to 1 because of the lack of myelin at birth, and continually decreases following a logarithmic curve becoming closer to the optimal g-ratio of 0.6 for most efficient speed conduction.

The research presented in these studies provides more insight into brain development in late childhood and adolescence in both white and subcortical grey matter by using advanced imaging and modelling techniques. Brain development is a combination of complex physiological changes that can benefit from various MRI techniques to help explain observed changes. Greater understanding of the underlying microstructural changes during healthy development can ultimately help identify deviations associated with neurological disorders and diseases.

References

Aboitiz, Francisco, Arnold B. Scheibel, Robin S. Fisher, and Eran Zaidel. 1992. "Fiber composition of the human corpus callosum." *Brain Research* 598 (1–2):143-153. doi: http://dx.doi.org/10.1016/0006-8993(92)90178-C.

Alexander, Daniel C., Penny L. Hubbard, Matt G. Hall, Elizabeth A. Moore, Maurice Ptito, Geoff J. M. Parker, and Tim B. Dyrby. 2010. "Orientationally invariant indices of axon diameter and density from diffusion MRI." *NeuroImage* 52 (4):1374-1389. doi: http://dx.doi.org/10.1016/j.neuroimage.2010.05.043.

Alsop, D.C., R Dandamudi, and R Bakshi. 2007. "Inhomogeneous Magnetization Transfer Imaging of Myelin Concentration in Multiple Sclerosis." *Proc. Intl. Soc. Mag. Reson. Med.* 15:2188.

Argyridis, Ioannis, Wei Li, G. Allan Johnson, and Chunlei Liu. 2013. "Quantitative Magnetic Susceptibility of the Developing Mouse Brain Reveals Microstructural Changes in the White Matter." *NeuroImage* 0:134-142. doi: 10.1016/j.neuroimage.2013.11.026.

Assaf, Yaniv and Blumenfeld-Katzir Tamar and Yovel Yossi and Basser Peter J. 2008. "Axcaliber: A method for measuring axon diameter distribution from diffusion MRI." *Magnetic Resonance in Medicine* 59 (6):1347--1354. doi: 10.1002/mrm.21577.

Avants, Brian B., Nicholas J. Tustison, Gang Song, Philip A. Cook, Arno Klein, and James C. Gee. 2011. "A reproducible evaluation of ANTs similarity metric performance in brain image registration." *NeuroImage* 54 (3):2033-2044. doi: http://dx.doi.org/10.1016/j.neuroimage.2010.09.025.

Barkovich, A. J., B. O. Kjos, D. E. Jackson, Jr., and D. Norman. 1988. "Normal maturation of the neonatal and infant brain: MR imaging at 1.5 T." *Radiology* 166 (1 Pt 1):173-80.

Basser, P. J., J. Mattiello, and D. Lebihan. 1994. "Estimation of the Effective Self-Diffusion Tensor from the NMR Spin Echo." *Journal of Magnetic Resonance, Series B* 103 (3):247-254. doi: http://dx.doi.org/10.1006/jmrb.1994.1037.

Beaulieu, Christian. 2002. "The basis of anisotropic water diffusion in the nervous system – a technical review." *NMR in Biomedicine* 15 (7-8):435-455. doi: 10.1002/nbm.782.

Beaulieu, Christian and Allen Peter S. 1994. "Determinants of anisotropic water diffusion in nerves." *Magnetic Resonance in Medicine* 31 (4):394--400. doi: 10.1002/mrm.1910310408.

Benes, F. M. 1989. "Myelination of cortical-hippocampal relays during late adolescence." *Schizophr Bull* 15 (4):585-93.

Berry, Isabelle and Barker Gareth J. and Barkhof Frederik and Campi Adriana and Dousset Vincent and Franconi Jean-Michel and Gass Achim and Schreiber Wolfgang and Miller David H. and Tofts Paul S. 1999. "A multicenter measurement of magnetization transfer ratio in normal white matter." *Journal of Magnetic Resonance Imaging* 9 (3):441--446. doi: 10.1002/(SICI)1522-2586(199903)9:3<441::AID-JMRI12>3.0.CO;2-R.

Borich, M. R., A. L. MacKay, I. M. Vavasour, A. Rauscher, and L. A. Boyd. 2013. "Evaluation of white matter myelin water fraction in chronic stroke." *NeuroImage: Clinical* 2:569-580. doi: http://dx.doi.org/10.1016/j.nicl.2013.04.006.

Brody, Betty Ann, Hannah C. Kinney, Alexander S. Kloman, and Floyd H. Gilles. 1987. "Sequence of Central Nervous System Myelination in Human Infancy. I. An Autopsy Study of Myelination." *Journal of Neuropathology & Experimental Neurology* 46 (3):283-301.

Bushberg, Jerrold T. 2002. *The essential physics of medical imaging*. 2nd ed. Philadelphia: Lippincott Williams & Wilkins.

Chang, Yi Shin, Julia P. Owen, Nicholas J. Pojman, Tony Thieu, Polina Bukshpun, Mari L. J. Wakahiro, Jeffrey I. Berman, Timothy P. L. Roberts, Srikantan S. Nagarajan, Elliott H. Sherr, and Pratik Mukherjee. 2015. "White Matter Changes of Neurite Density and Fiber Orientation Dispersion during Human Brain Maturation." *PLoS ONE* 10 (6):e0123656. doi: 10.1371/journal.pone.0123656.

Counsell, Serena J., Elia F. Maalouf, Alison M. Fletcher, Philip Duggan, Malcolm Battin, Helen J. Lewis, Amy H. Herlihy, A. David Edwards, Graeme M. Bydder, and Mary A. Rutherford. 2002. "MR Imaging Assessment of Myelination in the Very Preterm Brain." *American Journal of Neuroradiology* 23 (5):872-881.

Dekaban, A. S. 1978. "Changes in brain weights during the span of human life: relation of brain weights to body heights and body weights." *Ann Neurol* 4 (4):345-56. doi: 10.1002/ana.410040410.

Deoni, S. C., D. C. Dean, 3rd, J. O'Muircheartaigh, H. Dirks, and B. A. Jerskey. 2012. "Investigating white matter development in infancy and early childhood using myelin water faction and relaxation time mapping." *Neuroimage* 63 (3):1038-53. doi: 10.1016/j.neuroimage.2012.07.037.

Deoni, Sean C. L. 2011. "Correction of main and transmit magnetic field (B0 and B1) inhomogeneity effects in multicomponent-driven equilibrium single-pulse observation of T1 and T2." *Magnetic Resonance in Medicine* 65 (4):1021--1035. doi: 10.1002/mrm.22685.

Deoni, Sean C. L., Lucy Matthews, and Shannon H. Kolind. 2013. "One component? Two components? Three? The effect of including a nonexchanging “free” water component in multicomponent driven equilibrium single pulse observation of T1 and T2." *Magnetic Resonance in Medicine* 70 (1):147-154. doi: 10.1002/mrm.24429.

Deoni, Sean CL, Evelyne Mercure, Anna Blasi, David Gasston, Alex Thomson, Mark Johnson, Steven CR Williams, and Declan GM Murphy. 2011. "Mapping infant brain myelination with magnetic resonance imaging." *The Journal of Neuroscience* 31 (2):784-791.

Dubois, J., G. Dehaene-Lambertz, S. Kulikova, C. Poupon, P. S. Hüppi, and L. Hertz-Pannier. 2014. "The early development of brain white matter: A review of imaging studies in fetuses, newborns and infants." *Neuroscience* 276:48-71. doi: http://dx.doi.org/10.1016/j.neuroscience.2013.12.044.

Dubois, J., G. Dehaene-Lambertz, M. Perrin, J. F. Mangin, Y. Cointepas, E. Duchesnay, D. Le Bihan, and L. Hertz-Pannier. 2008. "Asynchrony of the early maturation of white matter bundles in healthy infants: quantitative landmarks revealed noninvasively by diffusion tensor imaging." *Hum Brain Mapp* 29 (1):14-27.

Eaton-Rosen, Zach, Andrew Melbourne, Eliza Orasanu, M. Jorge Cardoso, Marc Modat, Alan Bainbridge, Giles S. Kendall, Nicola J. Robertson, Neil Marlow, and Sebastien Ourselin. 2015. "Longitudinal measurement of the developing grey matter in preterm subjects using multi-modal MRI." *NeuroImage* 111:580-589. doi: http://dx.doi.org/10.1016/j.neuroimage.2015.02.010.

Eilaghi, Armin, D Adam McLean, Cheryl R McCreary, David Gobbi, M Louis Lauzon, Marina Salluzzi, Eric E Smith, and Richard Frayne. 2015. "Brain Magnetic Susceptibility is Increased with Cognitive Impairment in a Community Population." Proc. Intl. Soc. Mag. Reson. Med. 23, Toronto, ON.

Engelbrecht, V., M. Rassek, S. Preiss, C. Wald, and U. Mödder. 1998. "Age-dependent changes in magnetization transfer contrast of white matter in the pediatric brain." *American Journal of Neuroradiology* 19 (10):1923-1929.

Giedd, J. N., R. K. Lenroot, P. Shaw, F. Lalonde, M. Celano, S. White, J. Tossell, A. Addington, and N. Gogtay. 2008. "Trajectories of anatomic brain development as a phenotype." *Novartis Foundation symposium* 289:101-12; discussion 112-8, 193-5.

Giedd, Jay N., Jonathan Blumenthal, Neal O. Jeffries, F. X. Castellanos, Hong Liu, Alex Zijdenbos, Tomas Paus, Alan C. Evans, and Judith L. Rapoport. 1999. "Brain development during childhood and adolescence: a longitudinal MRI study." *Nat Neurosci* 2 (10):861-863.

Giedd, Jay N., Judith M. Rumsey, F. Xavier Castellanos, Jagath C. Rajapakse, Debra Kaysen, A. Catherine Vaituzis, Yolanda C. Vauss, Susan D. Hamburger, and Judith L. Rapoport. 1996. "A quantitative MRI study of the corpus callosum in children and adolescents." *Developmental Brain Research* 91 (2):274-280. doi: http://dx.doi.org/10.1016/0165-3806(95)00193-X.

Gulani, V. and Webb A. G. and Duncan I. D. and Lauterbur P. C. 2001. "Apparent diffusion tensor measurements in myelin-deficient rat spinal cords." *Magnetic Resonance in Medicine* 45 (2):191--195. doi: 10.1002/1522-2594(200102)45:2<191::AID-MRM1025>3.0.CO;2-9.

Hallgren, B. and Sourander P. 1958. "The Effect of Age on the Non-Haemin Iron in the Human Brain." *Journal of Neurochemistry* 3 (1):41--51. doi: 10.1111/j.1471-4159.1958.tb12607.x.

Hartigan, J. A., and M. A. Wong. 1979. "Algorithm AS 136: A K-Means Clustering Algorithm." *Journal of the Royal Statistical Society. Series C (Applied Statistics)* 28 (1):100-108. doi: 10.2307/2346830.

Hayakawa, Katsumi, Yukuo Konishi, Masanori Kuriyama, Kaoru Konishi, and Tuyoshi Matsuda. 1991. "Normal brain maturation in MRI." *European Journal of Radiology* 12 (3):208-215. doi: http://dx.doi.org/10.1016/0720-048X(91)90074-6.

Hendrick, R. E. 1994. "The AAPM/RSNA physics tutorial for residents. Basic physics of MR imaging: an introduction." *RadioGraphics* 14 (4):829-846. doi: doi:10.1148/radiographics.14.4.7938771.

Henkelman, R. M., G. J. Stanisz, and S. J. Graham. 2001. "Magnetization transfer in MRI: a review." *NMR in Biomedicine* 14 (2):57-64. doi: 10.1002/nbm.683.

Holland, B. A., D. K. Haas, D. Norman, M. Brant-Zawadzki, and T. H. Newton. 1986. "MRI of normal brain maturation." *American Journal of Neuroradiology* 7 (2):201-208.

Jenkinson, Mark. 2003. "Fast, automated, N-dimensional phase-unwrapping algorithm." *Magnetic Resonance in Medicine* 49 (1):193--197. doi: 10.1002/mrm.10354.

Jenkinson, Mark, Peter Bannister, Michael Brady, and Stephen Smith. 2002. "Improved Optimization for the Robust and Accurate Linear Registration and Motion Correction of Brain Images." *NeuroImage* 17 (2):825-841. doi: http://dx.doi.org/10.1006/nimg.2002.1132.

Jenkinson, Mark, Christian F. Beckmann, Timothy E. J. Behrens, Mark W. Woolrich, and Stephen M. Smith. 2012. "FSL." *NeuroImage* 62 (2):782-790. doi: http://dx.doi.org/10.1016/j.neuroimage.2011.09.015.

Jenkinson, Mark, and Stephen Smith. 2001. "A global optimisation method for robust affine registration of brain images." *Medical Image Analysis* 5 (2):143-156. doi: http://dx.doi.org/10.1016/S1361-8415(01)00036-6.

Jones, D. K. and Horsfield M. A. and Simmons A. 1999. "Optimal strategies for measuring diffusion in anisotropic systems by magnetic resonance imaging." *Magnetic Resonance in Medicine* 42 (3):515--525. doi: 10.1002/(SICI)1522-2594(199909)42:3<515::AID-MRM14>3.0.CO;2-Q.

Julian, Laura, Dana Serafin, Leigh Charvet, Joseph Ackerson, Ralph Benedict, Ellen Braaten, Tanya Brown, Ellen O'Donnell, Joy Parrish, Thomas Preston, Michael Zaccariello, Anita Belman, Tanuja Chitnis, Mark Gorman, Jayne Ness, Marc Patterson, Moses Rodriguez, Emmanuelle Waubant, Bianca Weinstock-Guttman, Ann Yeh, Lauren B. Krupp, and M. S. Centers of Excellence for the Network of Pediatric. 2013. "Cognitive Impairment Occurs in Children and Adolescents With Multiple Sclerosis: Results From a United States Network." *Journal of Child Neurology* 28 (1):102-107.

Kinney, Hannah, Betty Ann brody, Alexander Kloman, and Floyd Gilles. 1988. "Sequence of Central Nervous System Myelination in Human Infancy. II. Patterns of Myelination in Autopsied Infants." *J Neuropathol Exp Neurol* 47 (3):217-234.

Kunz, Nicolas, Hui Zhang, Lana Vasung, Kieran R. O'Brien, Yaniv Assaf, François Lazeyras, Daniel C. Alexander, and Petra S. Hüppi. 2014. "Assessing white matter microstructure of the newborn with multi-shell diffusion MRI and biophysical compartment models." *NeuroImage* 96:288-299. doi: http://dx.doi.org/10.1016/j.neuroimage.2014.03.057.

Lamantia, A. S. and Rakic P. 1990. "Cytological and quantitative characteristics of four cerebral commissures in the rhesus monkey." *The Journal of Comparative Neurology* 291 (4):520--537. doi: 10.1002/cne.902910404.

Landing, B. H., W. R. Shankle, J. Hara, J. Brannock, and J. H. Fallon. 2002. "The development of structure and function in the postnatal human cerebral cortex from birth to 72 months: changes in thickness of layers II and III co-relate to the onset of new age-specific behaviors." *Pediatric pathology & molecular medicine* 21 (3):321-42. doi: 10.1080/02770930290056541.

Laule, C., E. Leung, D. Kb Li, A. L. Traboulsee, D. W. Paty, A. L. MacKay, and G. Rw Moore. 2006. "Myelin water imaging in multiple sclerosis: quantitative correlations with histopathology." *Multiple Sclerosis* 12 (6):747-753.

Lauterbur, P. C. 1973. "Image Formation by Induced Local Interactions: Examples Employing Nuclear Magnetic Resonance." *Nature* 242 (5394):190-191.

Lebel, C., and C. Beaulieu. 2011. "Longitudinal development of human brain wiring continues from childhood into adulthood." *J Neurosci* 31 (30):10937-47. doi: 31/30/10937 [pii]
10.1523/JNEUROSCI.5302-10.2011.

Lebel, C., M. Gee, R. Camicioli, M. Wieler, W. Martin, and C. Beaulieu. 2012. "Diffusion tensor imaging of white matter tract evolution over the lifespan." *Neuroimage* 60 (1):340-52. doi: 10.1016/j.neuroimage.2011.11.094.

Lebel, C., L. Walker, A. Leemans, L. Phillips, and C. Beaulieu. 2008. "Microstructural maturation of the human brain from childhood to adulthood." *Neuroimage* 40 (3):1044-55.

Leppert, I. R., C. R. Almli, R. C. McKinstry, R. V. Mulkern, C. Pierpaoli, M. J. Rivkin, and G. B. Pike. 2009. "T(2) relaxometry of normal pediatric brain development." *Journal of magnetic resonance imaging : JMRI* 29 (2):258-67. doi: 10.1002/jmri.21646.

Li, Wei, Bing Wu, Alexandru V. Avram, and Chunlei Liu. 2012. "Magnetic susceptibility anisotropy of human brain in vivo and its molecular underpinnings." *NeuroImage* 59 (3):2088-2097. doi: http://dx.doi.org/10.1016/j.neuroimage.2011.10.038.

Li, Wei, Bing Wu, Anastasia Batrachenko, Vivian Bancroft-Wu, Rajendra A. Morey, Vandana Shashi, Christian Langkammer, Michael D. De Bellis, Stefan Ropele, Allen W. Song, and Chunlei Liu. 2014. "Differential Developmental Trajectories of Magnetic Susceptibility in Human Brain Gray and White Matter Over the Lifespan." *Human brain mapping* 35 (6):2698-2713. doi: 10.1002/hbm.22360.

Li, Wei, Bing Wu, and Chunlei Liu. 2011. "Quantitative Susceptibility Mapping of Human Brain Reflects Spatial Variation in Tissue Composition." *NeuroImage* 55 (4):1645-1656. doi: 10.1016/j.neuroimage.2010.11.088.

Liewald, Daniel, Robert Miller, Nikos Logothetis, Hans-Joachim Wagner, and Almut Schüz. 2014. "Distribution of axon diameters in cortical white matter: an electron-microscopic study on three human brains and a macaque." *Biological Cybernetics* 108 (5):541-557. doi: 10.1007/s00422-014-0626-2.

Liu, Chunlei, Wei Li, G. Allan Johnson, and Bing Wu. 2011. "High-Field (9.4 T) MRI of Brain Dysmyelination by Quantitative Mapping of Magnetic Susceptibility." *NeuroImage* 56 (3):930-938. doi: 10.1016/j.neuroimage.2011.02.024.

Liu, Tian and Spincemaille Pascal and de Rochefort Ludovic and Kressler Bryan and Wang Yi. 2009. "Calculation of susceptibility through multiple orientation sampling (COSMOS): A method for conditioning the inverse problem from measured magnetic field map to susceptibility source image in MRI." *Magnetic Resonance in Medicine* 61 (1):196--204. doi: 10.1002/mrm.21828.

Lochner, Christine, Jean-Paul Fouché, Stefan du Plessis, Bruce Spottiswoode, Soraya Seedat, MMed, Naomi Fineberg, Samuel R. Chamberlain, and Dan J. Stein. 2012. "Evidence for fractional anisotropy and mean diffusivity white matter abnormalities in the internal capsule and cingulum in patients with obsessive–compulsive disorder." *Journal of Psychiatry & Neuroscience : JPN* 37 (3):193-199. doi: 10.1503/jpn.110059.

Lodygensky, G. A., J. P. Marques, R. Maddage, E. Perroud, S. V. Sizonenko, P. S. Huppi, and R. Gruetter. 2012. "In vivo assessment of myelination by phase imaging at high magnetic field." *Neuroimage* 59 (3):1979-87. doi: 10.1016/j.neuroimage.2011.09.057.

Mazziotta, J., A. Toga, A. Evans, P. Fox, J. Lancaster, K. Zilles, R. Woods, T. Paus, G. Simpson, B. Pike, C. Holmes, L. Collins, P. Thompson, D. MacDonald, M. Iacoboni, T. Schormann, K. Amunts, N. Palomero-Gallagher, S. Geyer, L. Parsons, K. Narr, N. Kabani, G. Le Goualher, D. Boomsma, T. Cannon, R. Kawashima, and B. Mazoyer. 2001. "A probabilistic atlas and reference system for the human brain: International Consortium for Brain Mapping (ICBM)." *Philosophical Transactions of the Royal Society of London. Series B* 356 (1412):1293-1322. doi: 10.1098/rstb.2001.0915.

McGowan, J. C. 1999. "The physical basis of magnetization transfer imaging." *Neurology* 53 (5 Suppl 3):S3-7.

Mori, Susumu, Kenichi Oishi, Hangyi Jiang, Li Jiang, Xin Li, Kazi Akhter, Kegang Hua, Andreia V. Faria, Asif Mahmood, Roger Woods, Arthur Toga, Bruce Pike, Pedro Rosa Neto, Alan Evans, Jiangyang Zhang, Hao Huang, Michael I. Miller, Peter van Zijl, and John Mazziotta. 2008. "Stereotaxic White Matter Atlas Based on Diffusion Tensor Imaging in an ICBM Template." *NeuroImage* 40 (2):570-582. doi: 10.1016/j.neuroimage.2007.12.035.

Mukherjee, Pratik, Jeffrey H. Miller, Joshua S. Shimony, Thomas E. Conturo, Benjamin C. P. Lee, C. Robert Almli, and Robert C. McKinstry. 2001. "Normal Brain Maturation during Childhood: Developmental Trends Characterized with Diffusion-Tensor MR Imaging." *Radiology* 221 (2):349-358. doi: 10.1148/radiol.2212001702.

Nobelprize.org. 2013a. "The Nobel Prize in Physics 1944." Nobel Media AB Accessed 10 Dec 2013. http://www.nobelprize.org/nobel_prizes/physics/laureates/1944/.

Nobelprize.org. 2013b. "The Nobel Prize in Physics 1952." Nobel Media AB Accessed 10 Dec 2013. http://www.nobelprize.org/nobel_prizes/physics/laureates/1952/.

Nobelprize.org. 2013c. "The Nobel Prize in Physiology or Medicine 2003." Nobel Media AB Accessed 10 Dec 2013. http://www.nobelprize.org/nobel_prizes/medicine/laureates/2003/.

Oishi, Kenichi, Andreia Faria, Hangyi Jiang, Xin Li, Kazi Akhter, Jiangyang Zhang, John T. Hsu, Michael I. Miller, Peter C. M. van Zijl, Marilyn Albert, Constantine G. Lyketsos, Roger Woods, Arthur W. Toga, G. Bruce Pike, Pedro Rosa-Neto, Alan Evans, John Mazziotta, and Susumu Mori. 2009. "Atlas-based whole brain white matter analysis using large deformation diffeomorphic metric mapping: Application to normal elderly and Alzheimer's disease participants." *NeuroImage* 46 (2):486-499.

Paus, T., A. Zijdenbos, K. Worsley, D. L. Collins, J. Blumenthal, J. N. Giedd, J. L. Rapoport, and A. C. Evans. 1999. "Structural maturation of neural pathways in children and adolescents: in vivo study." *Science* 283 (5409):1908-11.

Perrin, J. S., G. Leonard, M. Perron, G. B. Pike, A. Pitiot, L. Richer, S. Veillette, Z. Pausova, and T. Paus. 2009a. "Sex differences in the growth of white matter during adolescence." *Neuroimage* 45 (4):1055-66. doi: S1053-8119(09)00062-7 [pii]
10.1016/j.neuroimage.2009.01.023.

Perrin, J. S., G. Leonard, M. Perron, G. B. Pike, A. Pitiot, L. Richer, S. Veillette, Z. Pausova, and T. Paus. 2009b. "Sex differences in the growth of white matter during adolescence." *NeuroImage* 45 (4):1055-1066. doi: http://dx.doi.org/10.1016/j.neuroimage.2009.01.023.

Peter R, Huttenlocher. 1979. "Synaptic density in human frontal cortex — Developmental changes and effects of aging." *Brain Research* 163 (2):195-205. doi: http://dx.doi.org/10.1016/0006-8993(79)90349-4.

Pooley, Robert A. 2005. "Fundamental Physics of MR Imaging1." *Radiographics* 25 (4):1087-1099. doi: 10.1148/rg.254055027.

Rabi, I. I., J. R. Zacharias, S. Millman, and P. Kusch. 1938. "A New Method of Measuring Nuclear Magnetic Moment." *Physical Review* 53 (4):318-318.

Reiss, Allan L., Michael T. Abrams, Harvey S. Singer, Judith L. Ross, and Martha B. Denckla. 1996. "Brain development, gender and IQ in children." *Brain* 119 (5):1763-1774.

Reuter, Martin, Nicholas J. Schmansky, H. Diana Rosas, and Bruce Fischl. 2012. "Within-subject template estimation for unbiased longitudinal image analysis." *NeuroImage* 61 (4):1402-1418. doi: http://dx.doi.org/10.1016/j.neuroimage.2012.02.084.

Rushton, W. A. H. 1951. "A theory of the effects of fibre size in medullated nerve." *The Journal of Physiology* 115 (1):101--122. doi: 10.1113/jphysiol.1951.sp004655.

Schmierer, Klaus and Scaravilli Francesco and Altmann Daniel R. and Barker Gareth J. and Miller David H. 2004. "Magnetization transfer ratio and myelin in postmortem multiple sclerosis brain." *Annals of Neurology* 56 (3):407--415. doi: 10.1002/ana.20202.

Schweser, Ferdinand, Andreas Deistung, Berengar Wendel Lehr, and Jürgen Rainer Reichenbach. 2011. "Quantitative imaging of intrinsic magnetic tissue properties using MRI signal phase: An approach to in vivo brain iron metabolism?" *NeuroImage* 54 (4):2789-2807. doi: http://dx.doi.org/10.1016/j.neuroimage.2010.10.070.

Snook, Lindsay, Lori-Anne Paulson, Dawne Roy, Linda Phillips, and Christian Beaulieu. 2005. "Diffusion tensor imaging of neurodevelopment in children and young adults." *NeuroImage* 26 (4):1164-1173. doi: http://dx.doi.org/10.1016/j.neuroimage.2005.03.016.

Song, S. K., S. W. Sun, W. K. Ju, S. J. Lin, A. H. Cross, and A. H. Neufeld. 2003. "Diffusion tensor imaging detects and differentiates axon and myelin degeneration in mouse optic nerve after retinal ischemia." *Neuroimage* 20 (3):1714-22. doi: S1053811903004403 [pii].

Stanisz, Greg J. and Webb Stephanie and Munro Catherine A. and Pun Teresa and Midha Rajiv. 2004. "MR properties of excised neural tissue following experimentally induced inflammation." *Magnetic Resonance in Medicine* 51 (3):473--479. doi: 10.1002/mrm.20008.

Stikov, Nikola, Jennifer S. W. Campbell, Thomas Stroh, Mariette Lavelée, Stephen Frey, Jennifer Novek, Stephen Nuara, Ming-Kai Ho, Barry J. Bedell, Robert F. Dougherty, Ilana R. Leppert, Mathieu Boudreau, Sridar Narayanan, Tanguy Duval, Julien Cohen-Adad, Paul-Alexandre Picard, Alicja Gasecka, Daniel Côté, and G. Bruce Pike. 2015. "In vivo histology of the myelin g-ratio with magnetic resonance imaging." *NeuroImage* 118:397-405. doi: http://dx.doi.org/10.1016/j.neuroimage.2015.05.023.

Stikov, Nikola, Lee M. Perry, Aviv Mezer, Elena Rykhlevskaia, Brian A. Wandell, John M. Pauly, and Robert F. Dougherty. 2011. "Bound pool fractions complement diffusion measures to describe white matter micro and macrostructure." *NeuroImage* 54 (2):1112-1121. doi: http://dx.doi.org/10.1016/j.neuroimage.2010.08.068.

Sun, Hongfu and Wilman Alan H. 2014. "Background field removal using spherical mean value filtering and Tikhonov regularization." *Magnetic Resonance in Medicine* 71 (3):1151--1157. doi: 10.1002/mrm.24765.

van Buchem, Mark A., Stefan C. A. Steens, Henri A. Vrooman, Aeilko H. Zwinderman, Joseph C. McGowan, Margarethe Rassek, and Volkher Engelbrecht. 2001. "Global Estimation of Myelination in the Developing Brain on the Basis of Magnetization Transfer Imaging: A Preliminary Study." *American Journal of Neuroradiology* 22 (4):762-766.

van der Knaap, M.S., and J. Valk. 1995. *Magnetic resonance of myelin, myelination, and myelin disorders*: Springer.

Vargas, Wendy S., Elizabeth Monohan, Sneha Pandya, Ashish Raj, Timothy Vartanian, Thanh D. Nguyen, Sandra M. Hurtado Rúa, and Susan A. Gauthier. 2015. "Measuring longitudinal myelin water fraction in new multiple sclerosis lesions." *NeuroImage: Clinical* 9:369-375. doi: http://dx.doi.org/10.1016/j.nicl.2015.09.003.

Varma, Gopal and Duhamel Guillaume and de Bazelaire Cedric and Alsop David C. 2015. "Magnetization transfer from inhomogeneously broadened lines: A potential marker for myelin." *Magnetic Resonance in Medicine* 73 (2):614--622. doi: 10.1002/mrm.25174.

Westlye, Lars T., Kristine B. Walhovd, Anders M. Dale, Atle Bjørnerud, Paulina Due-Tønnessen, Andreas Engvig, Håkon Grydeland, Christian K. Tamnes, Ylva Østby, and Anders M. Fjell. 2010. "Life-Span Changes of the Human Brain White Matter: Diffusion Tensor Imaging (DTI) and Volumetry." *Cerebral Cortex* 20 (9):2055-2068.

Yakovlev, P.I., and A.-R. Lecours. 1967. "The myelogenetic cycles of regional maturation of the brain." In *Regional development of the brain early in life.*, edited by A. Minkowski, 3-70. Boston, Massachusets: Blackwell Scientific Publications Inc.

Yendiki, Anastasia, Patricia Panneck, Priti Srinivasan, Allison Stevens, Lilla Zöllei, Jean Augustinack, Ruopeng Wang, David Salat, Stefan Ehrlich, Tim Behrens, Saad Jbabdi, Randy Gollub, and Bruce Fischl. 2011. "Automated Probabilistic Reconstruction of White-Matter Pathways in Health and Disease Using an Atlas of the Underlying Anatomy." *Frontiers in Neuroinformatics* 5:23. doi: 10.3389/fninf.2011.00023.

Yoshida, S., K. Oishi, A. V. Faria, and S. Mori. 2013. "Diffusion tensor imaging of normal brain development." *Pediatr Radiol* 43 (1):15-27. doi: 10.1007/s00247-012-2496-x.

Zaaraoui, Wafaa, Mathilde Deloire, Michel Merle, Céline Girard, Gérard Raffard, Marc Biran, Matilde Inglese, KlausG Petry, Oded Gonen, Bruno Brochet, Jean-Michel Franconi, and Vincent Dousset. 2008. "Monitoring demyelination and remyelination by magnetization transfer imaging in the mouse brain at 9.4 T." *Magnetic Resonance Materials in Physics, Biology and Medicine* 21 (5):357-362. doi: 10.1007/s10334-008-0141-3.

Zhang, Hui, Penny L. Hubbard, Geoff J. M. Parker, and Daniel C. Alexander. 2011. "Axon diameter mapping in the presence of orientation dispersion with diffusion MRI." *NeuroImage* 56 (3):1301-1315. doi: http://dx.doi.org/10.1016/j.neuroimage.2011.01.084.

Zhang, Hui, Torben Schneider, Claudia A. Wheeler-Kingshott, and Daniel C. Alexander. 2012. "NODDI: Practical in vivo neurite orientation dispersion and density imaging of the human brain." *NeuroImage* 61 (4):1000-1016. doi: http://dx.doi.org/10.1016/j.neuroimage.2012.03.072.

Zhong, K., T. Ernst, S. Buchthal, O. Speck, L. Anderson, and L. Chang. 2011. "Phase contrast imaging in neonates." *Neuroimage* 55 (3):1068-72. doi: 10.1016/j.neuroimage.2010.11.086.

APPENDIX A: COPYRIGHT PERMISSIONS

JOHN WILEY AND SONS LICENSE TERMS AND CONDITIONS

Dec 27, 2015

This Agreement between Alyssa Mah ("You") and John Wiley and Sons ("John Wiley and Sons") consists of your license details and the terms and conditions provided by John Wiley and Sons and Copyright Clearance Center.

License Number	3777210228026
License date	Dec 27, 2015
Licensed Content Publisher	John Wiley and Sons
Licensed Content Publication	NMR in Biomedicine
Licensed Content Title	Magnetization transfer in MRI: a review
Licensed Content Author	R. M. Henkelman,G. J. Stanisz,S. J. Graham
Licensed Content Date	Apr 19, 2001
Pages	8
Type of Use	Dissertation/Thesis
Requestor type	University/Academic
Format	Print and electronic
Portion	Figure/table
Number of figures/tables	1
Original Wiley figure/table number(s)	Figure 1(b)
Will you be translating?	No
Title of your thesis / dissertation	Brain development during childhood and adolescence
Expected completion date	Dec 2015
Expected size (number of pages)	100
Requestor Location	Alyssa Mah University of Calgary 2500 University Dr NW None Calgary, AB T2N 1N4 Canada Attn: Alyssa Mah
Billing Type	Invoice
Billing Address	Alyssa Mah University of Calgary 2500 University Dr NW None Calgary, AB T2N 1N4 Canada Attn: Alyssa Mah
Total	**0.00 USD**
Terms and Conditions	

TERMS AND CONDITIONS

This copyrighted material is owned by or exclusively licensed to John Wiley & Sons, Inc. or one of its group companies (each a"Wiley Company") or handled on behalf of a society with which a Wiley Company has exclusive publishing rights in relation to a particular work (collectively "WILEY"). By clicking "accept" in connection with completing this licensing transaction, you agree that the following terms and conditions apply to this transaction (along with the billing and payment terms and conditions established by the Copyright Clearance Center Inc., ("CCC's Billing and Payment terms and conditions"), at the time that you opened your RightsLink account (these are available at any time at http://myaccount.copyright.com).

Terms and Conditions

- The materials you have requested permission to reproduce or reuse (the "Wiley Materials") are protected by copyright.

- You are hereby granted a personal, non-exclusive, non-sub licensable (on a stand-alone basis), non-transferable, worldwide, limited license to reproduce the Wiley Materials for the purpose specified in the licensing process. This license, **and any CONTENT (PDF or image file) purchased as part of your order,** is for a one-time use only and limited to any maximum distribution number specified in the license. The first instance of republication or reuse granted by this license must be completed within two years of the date of the grant of this license (although copies prepared before the end date may be distributed thereafter). The Wiley Materials shall not be used in any other manner or for any other purpose, beyond what is granted in the license. Permission is granted subject to an appropriate acknowledgement given to the author, title of the material/book/journal and the publisher. You shall also duplicate the copyright notice that appears in the Wiley publication in your use of the Wiley Material. Permission is also granted on the understanding that nowhere in the text is a previously published source acknowledged for all or part of this Wiley Material. Any third party content is expressly excluded from this permission.

- With respect to the Wiley Materials, all rights are reserved. Except as expressly granted by the terms of the license, no part of the Wiley Materials may be copied, modified, adapted (except for minor reformatting required by the new Publication), translated, reproduced, transferred or distributed, in any form or by any means, and no derivative works may be made based on the Wiley Materials without the prior permission of the respective copyright owner.**For STM Signatory Publishers clearing permission under the terms of the STM Permissions Guidelines only, the terms of the license are extended to include subsequent editions and for editions in other languages, provided such editions are for the work as a whole in situ and does not involve the separate exploitation of the permitted figures or extracts,** You may not alter, remove or suppress in any manner any copyright, trademark or other notices displayed by the Wiley Materials. You may not license, rent, sell, loan, lease, pledge, offer as security, transfer or assign the Wiley Materials on a stand-alone basis, or any of the rights granted to you hereunder to any other person.

- The Wiley Materials and all of the intellectual property rights therein shall at all times remain the exclusive property of John Wiley & Sons Inc, the Wiley Companies, or their respective licensors, and your interest therein is only that of having possession of and the right to reproduce the Wiley Materials pursuant to Section 2 herein during the continuance of this Agreement. You agree that you own no right, title or interest in or to the Wiley Materials or any of the intellectual property rights therein. You shall have no rights hereunder other than the license as provided for above in Section 2. No right, license or interest to any trademark, trade name, service mark or other branding ("Marks") of WILEY or its licensors is granted hereunder, and you agree that you shall not assert any such right, license or interest with respect thereto

- NEITHER WILEY NOR ITS LICENSORS MAKES ANY WARRANTY OR REPRESENTATION OF ANY KIND TO YOU OR ANY THIRD PARTY, EXPRESS, IMPLIED OR STATUTORY, WITH RESPECT TO THE MATERIALS OR THE ACCURACY OF ANY INFORMATION CONTAINED IN THE MATERIALS, INCLUDING, WITHOUT LIMITATION, ANY IMPLIED WARRANTY OF MERCHANTABILITY, ACCURACY, SATISFACTORY QUALITY, FITNESS FOR A PARTICULAR PURPOSE, USABILITY, INTEGRATION OR NON-INFRINGEMENT AND ALL SUCH WARRANTIES ARE HEREBY EXCLUDED BY WILEY AND ITS LICENSORS AND WAIVED BY YOU.

- WILEY shall have the right to terminate this Agreement immediately upon breach of this Agreement by you.

- You shall indemnify, defend and hold harmless WILEY, its Licensors and their respective directors, officers, agents and employees, from and against any actual or threatened claims, demands, causes of action or proceedings arising

from any breach of this Agreement by you.

- IN NO EVENT SHALL WILEY OR ITS LICENSORS BE LIABLE TO YOU OR ANY OTHER PARTY OR ANY OTHER PERSON OR ENTITY FOR ANY SPECIAL, CONSEQUENTIAL, INCIDENTAL, INDIRECT, EXEMPLARY OR PUNITIVE DAMAGES, HOWEVER CAUSED, ARISING OUT OF OR IN CONNECTION WITH THE DOWNLOADING, PROVISIONING, VIEWING OR USE OF THE MATERIALS REGARDLESS OF THE FORM OF ACTION, WHETHER FOR BREACH OF CONTRACT, BREACH OF WARRANTY, TORT, NEGLIGENCE, INFRINGEMENT OR OTHERWISE (INCLUDING, WITHOUT LIMITATION, DAMAGES BASED ON LOSS OF PROFITS, DATA, FILES, USE, BUSINESS OPPORTUNITY OR CLAIMS OF THIRD PARTIES), AND WHETHER OR NOT THE PARTY HAS BEEN ADVISED OF THE POSSIBILITY OF SUCH DAMAGES. THIS LIMITATION SHALL APPLY NOTWITHSTANDING ANY FAILURE OF ESSENTIAL PURPOSE OF ANY LIMITED REMEDY PROVIDED HEREIN.

- Should any provision of this Agreement be held by a court of competent jurisdiction to be illegal, invalid, or unenforceable, that provision shall be deemed amended to achieve as nearly as possible the same economic effect as the original provision, and the legality, validity and enforceability of the remaining provisions of this Agreement shall not be affected or impaired thereby.

- The failure of either party to enforce any term or condition of this Agreement shall not constitute a waiver of either party's right to enforce each and every term and condition of this Agreement. No breach under this agreement shall be deemed waived or excused by either party unless such waiver or consent is in writing signed by the party granting such waiver or consent. The waiver by or consent of a party to a breach of any provision of this Agreement shall not operate or be construed as a waiver of or consent to any other or subsequent breach by such other party.

- This Agreement may not be assigned (including by operation of law or otherwise) by you without WILEY's prior written consent.

- Any fee required for this permission shall be non-refundable after thirty (30) days from receipt by the CCC.

- These terms and conditions together with CCC's Billing and Payment terms and conditions (which are incorporated herein) form the entire agreement between you and WILEY concerning this licensing transaction and (in the absence of fraud) supersedes all prior agreements and representations of the parties, oral or written. This Agreement may not be amended except in writing signed by both parties. This Agreement shall be binding upon and inure to the benefit of the parties' successors, legal representatives, and authorized assigns.

- In the event of any conflict between your obligations established by these terms and conditions and those established by CCC's Billing and Payment terms and conditions, these terms and conditions shall prevail.

- WILEY expressly reserves all rights not specifically granted in the combination of (i) the license details provided by you and accepted in the course of this licensing transaction, (ii) these terms and conditions and (iii) CCC's Billing and Payment terms and conditions.

- This Agreement will be void if the Type of Use, Format, Circulation, or Requestor Type was misrepresented during the licensing process.

- This Agreement shall be governed by and construed in accordance with the laws of the State of New York, USA, without regards to such state's conflict of law rules. Any legal action, suit or proceeding arising out of or relating to these Terms and Conditions or the breach thereof shall be instituted in a court of competent jurisdiction in New York County in the State of New York in the United States of America and each party hereby consents and submits to the personal jurisdiction of such court, waives any objection to venue in such court and consents to service of process by registered or certified mail, return receipt requested, at the last known address of such party.

WILEY OPEN ACCESS TERMS AND CONDITIONS

Wiley Publishes Open Access Articles in fully Open Access Journals and in Subscription journals offering Online Open. Although most of the fully Open Access journals publish open access articles under the terms of the Creative Commons Attribution (CC BY) License only, the subscription journals and a few of the Open Access Journals offer a choice of Creative

Commons Licenses. The license type is clearly identified on the article.

The Creative Commons Attribution License

The Creative Commons Attribution License (CC-BY) allows users to copy, distribute and transmit an article, adapt the article and make commercial use of the article. The CC-BY license permits commercial and non-

Creative Commons Attribution Non-Commercial License

The Creative Commons Attribution Non-Commercial (CC-BY-NC)License permits use, distribution and reproduction in any medium, provided the original work is properly cited and is not used for commercial purposes.(see below)

Creative Commons Attribution-Non-Commercial-NoDerivs License

The Creative Commons Attribution Non-Commercial-NoDerivs License (CC-BY-NC-ND) permits use, distribution and reproduction in any medium, provided the original work is properly cited, is not used for commercial purposes and no modifications or adaptations are made. (see below)

Use by commercial "for-profit" organizations

Use of Wiley Open Access articles for commercial, promotional, or marketing purposes requires further explicit permission from Wiley and will be subject to a fee.

Further details can be found on Wiley Online Library http://olabout.wiley.com/WileyCDA/Section/id-410895.html

Other Terms and Conditions:

v1.10 Last updated September 2015

Questions? customercare@copyright.com or +1-855-239-3415 (toll free in the US) or +1-978-646-2777.

APPENDIX B: RESULTS FROM MD, AD AND RD

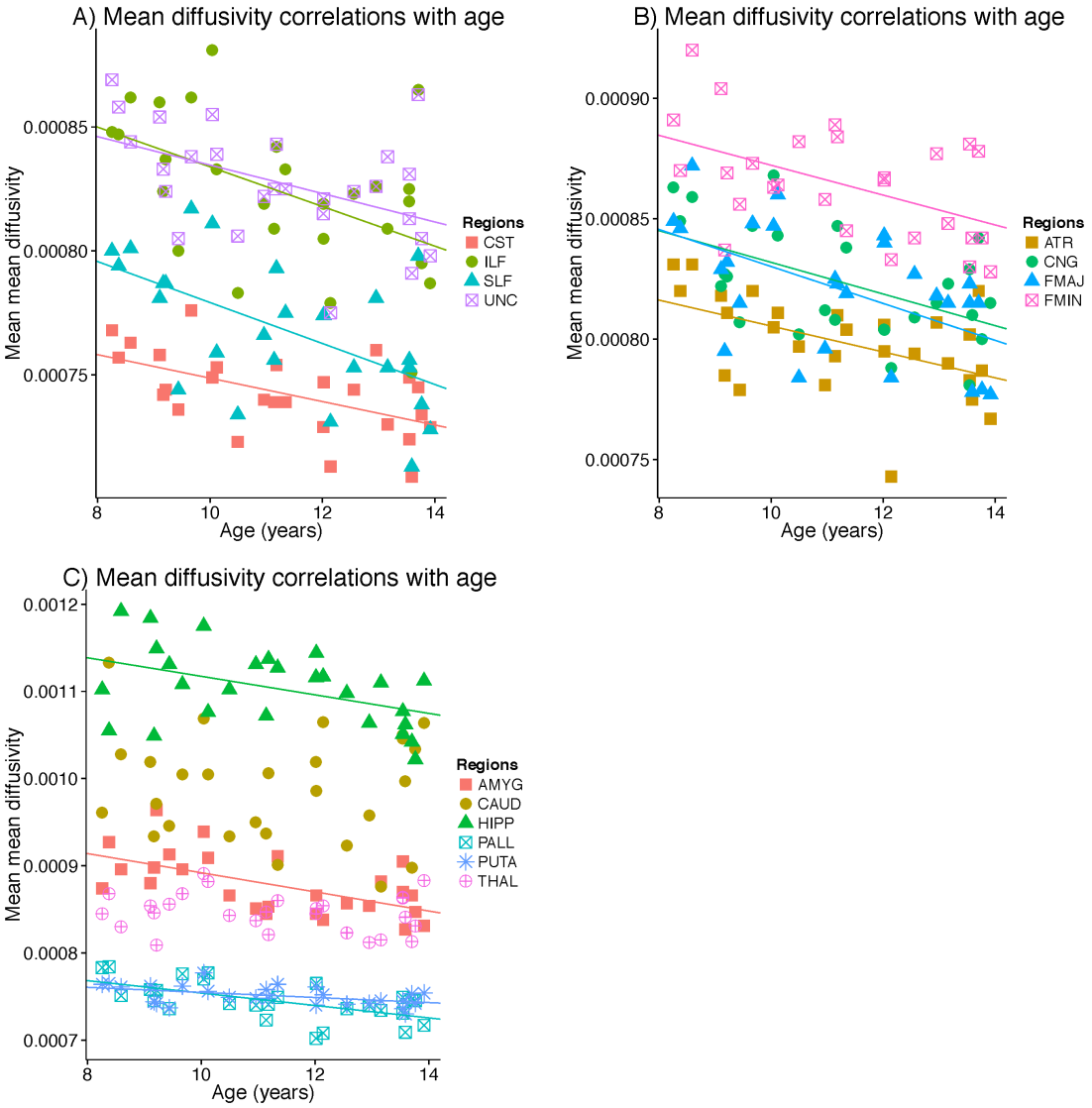

Figure 20. Mean diffusivity trajectories in white (A, B) and grey (C) matter volumes-of-interest. Significant lines of fit ($p<0.05$) are plotted on the graphs.

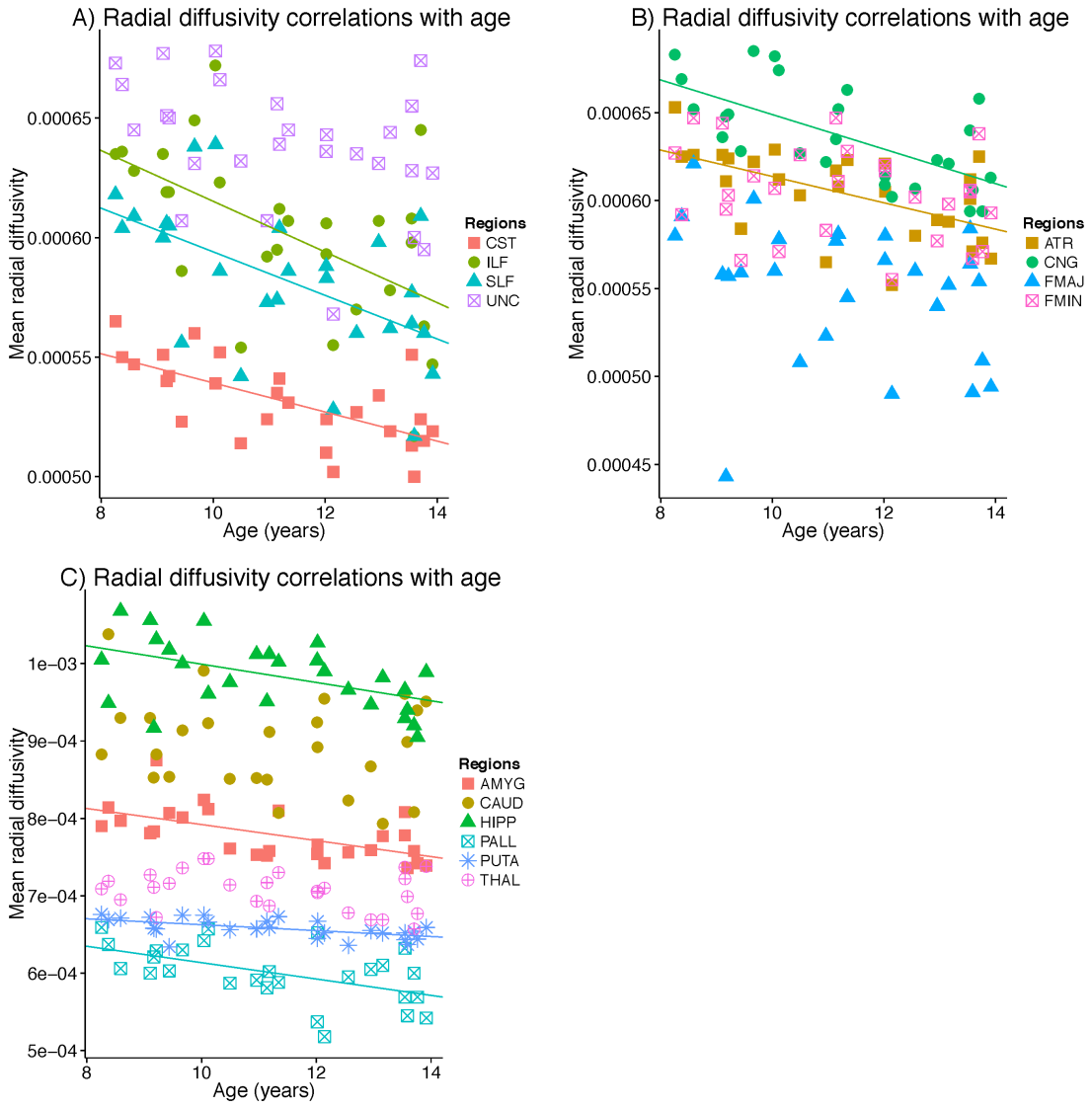

Figure 21. Radial diffusivity trajectories in white (A, B) and grey (C) matter volumes-of-interest. Significant lines of fit ($p<0.05$) are plotted on the graphs.

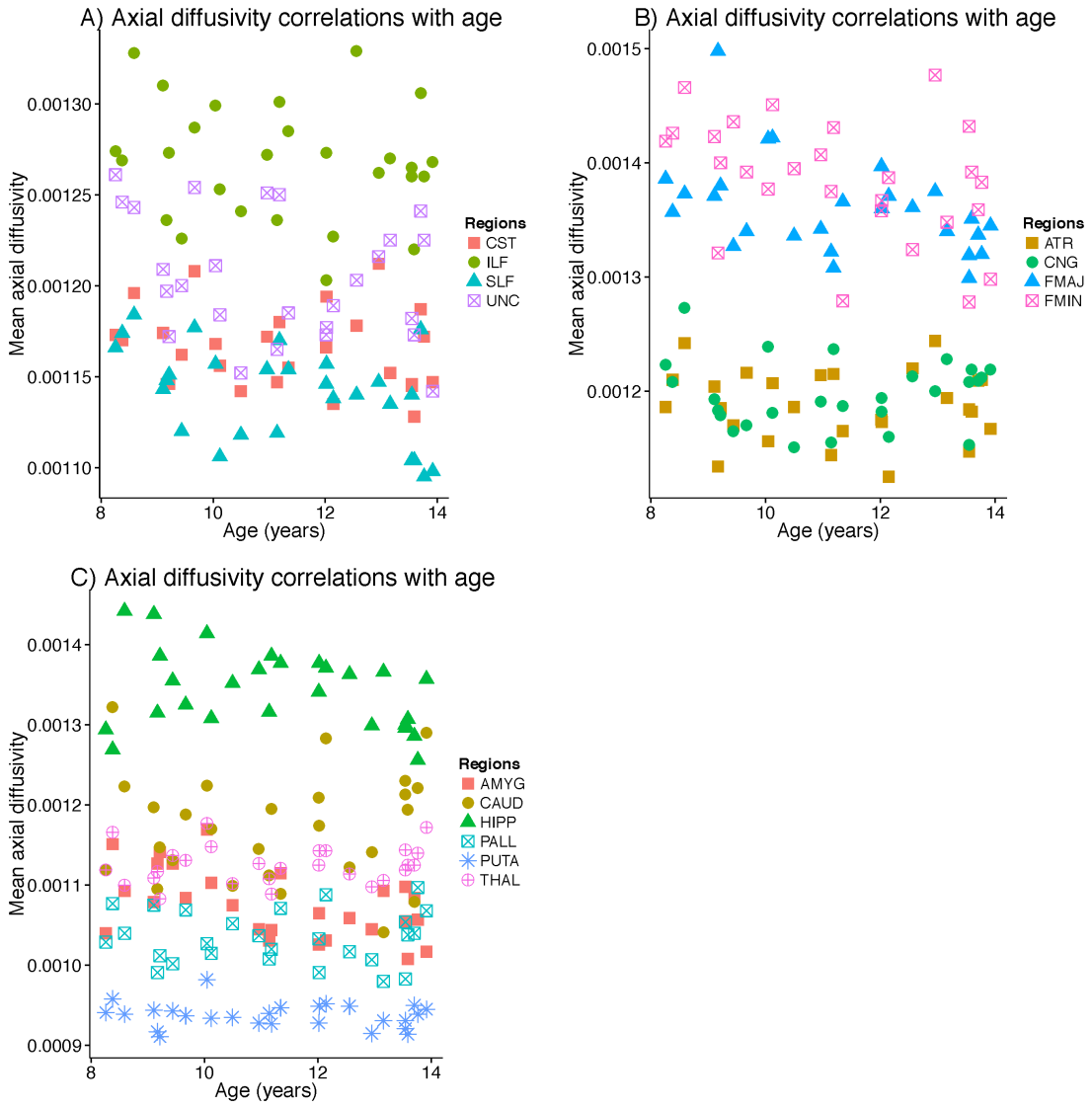

Figure 22. Axial diffusivity trajectories in white (A, B) and grey (C) matter volumes-of-interest. Significant lines of fit ($p<0.05$) are plotted on the graphs.

Table 14. Linear fitting results of MD (mean diffusivity) vs. age. The p-values were corrected for multiple comparisons using the false discovery rate method.

Region	Slope, m (10^{-6}/year)	Y-intercept, b (10^{-6})	R^2	p
ATR	-5.37	859	0.25	**0.012**
Cingulum	-6.57	898	0.29	**0.008**
CST	-4.73	796	0.31	**0.008**
Forceps major	-7.67	907	0.31	**0.008**
Forceps minor	-6.20	934	0.25	**0.012**
ILF	-8.00	914	0.25	**0.012**
SLF	-8.27	862	0.33	**0.008**
Uncinate	-5.74	892	0.23	**0.014**
Amygdala	-11.0	1000	0.36	**0.007**
Caudate	-2.67	1020	0.01	0.686
Hippocampus	-10.6	1220	0.20	**0.021**
Pallidum	-7.12	825	0.37	**0.007**
Putamen	-2.92	784	0.25	**0.012**
Thalamus	-2.04	869	0.03	0.423

Table 15. Linear fitting results of RD (radial diffusivity) vs. age. The p-values were corrected for multiple comparisons using the false discovery rate method.

Region	Slope, m (10^{-6}/year)	Y-intercept, b (10^{-6})	R^2	p
ATR	-7.49	689	0.33	**0.005**
Cingulum	-9.82	747	0.44	**0.001**
CST	-6.09	600	0.44	**0.001**
Forceps major	-6.51	624	0.09	0.153
Forceps minor	-3.58	644	0.07	0.206
ILF	-10.6	721	0.32	**0.005**
SLF	-9.12	685	0.31	**0.005**
Uncinate	-5.64	703	0.16	0.057
Amygdala	-10.4	896	0.36	**0.004**
Caudate	-4.27	946	0.02	0.504
Hippocampus	-11.8	1120	0.26	**0.011**
Pallidum	-10.6	719	0.29	**0.007**
Putamen	-3.82	701	0.33	**0.005**
Thalamus	-3.81	750	0.08	0.179

Table 16. Linear fitting results of AD (axial diffusivity) vs. age. The p-values were corrected for multiple comparisons using the false discovery rate method.

Region	Slope, m (10^{-6}/year)	Y-intercept, b (10^{-6})	R^2	p
ATR	-1.21	1200	<0.01	0.907
Cingulum	0.09	1200	<0.01	0.981
CST	-2.02	1190	0.03	0.691
Forceps major	-9.77	1470	0.20	0.094
Forceps minor	-11.5	1510	0.17	0.121
ILF	-2.61	1300	0.02	0.691
SLF	-6.66	1220	0.24	0.073
Uncinate	-5.99	1270	0.11	0.247
Amygdala	-11.9	1210	0.28	0.068
Caudate	0.51	1170	<0.01	0.981
Hippocampus	-8.18	1440	0.10	0.252
Pallidum	-0.09	1040	<0.01	0.981
Putamen	-1.28	952	0.02	0.691
Thalamus	1.41	1110	0.01	0.811

APPENDIX C: RESULTS FROM QMT AND QIHMT

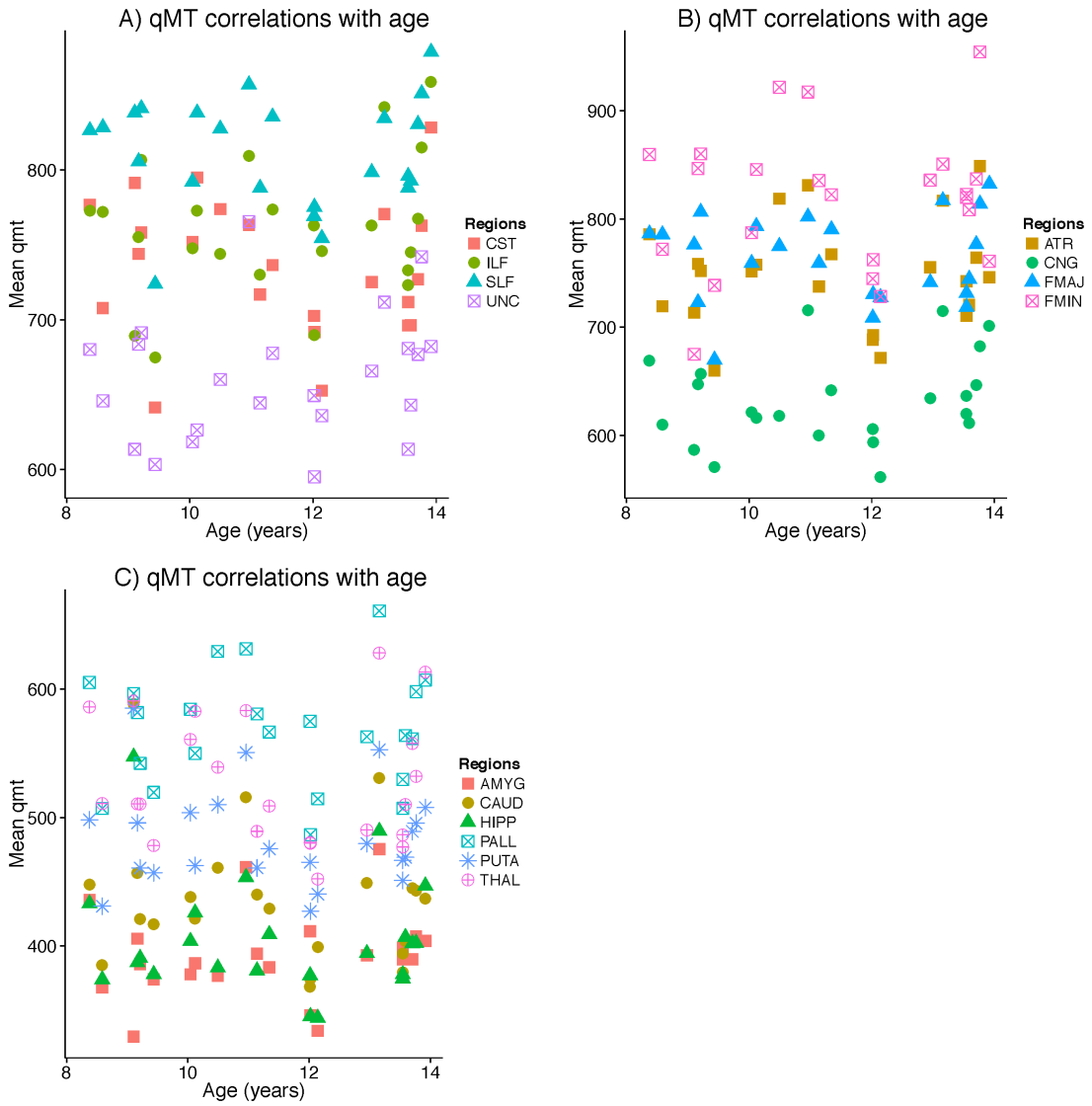

Figure 23. Mean qMT trajectories in white (A, B) and grey (C) matter volumes-of-interest.

No regressions were significant.

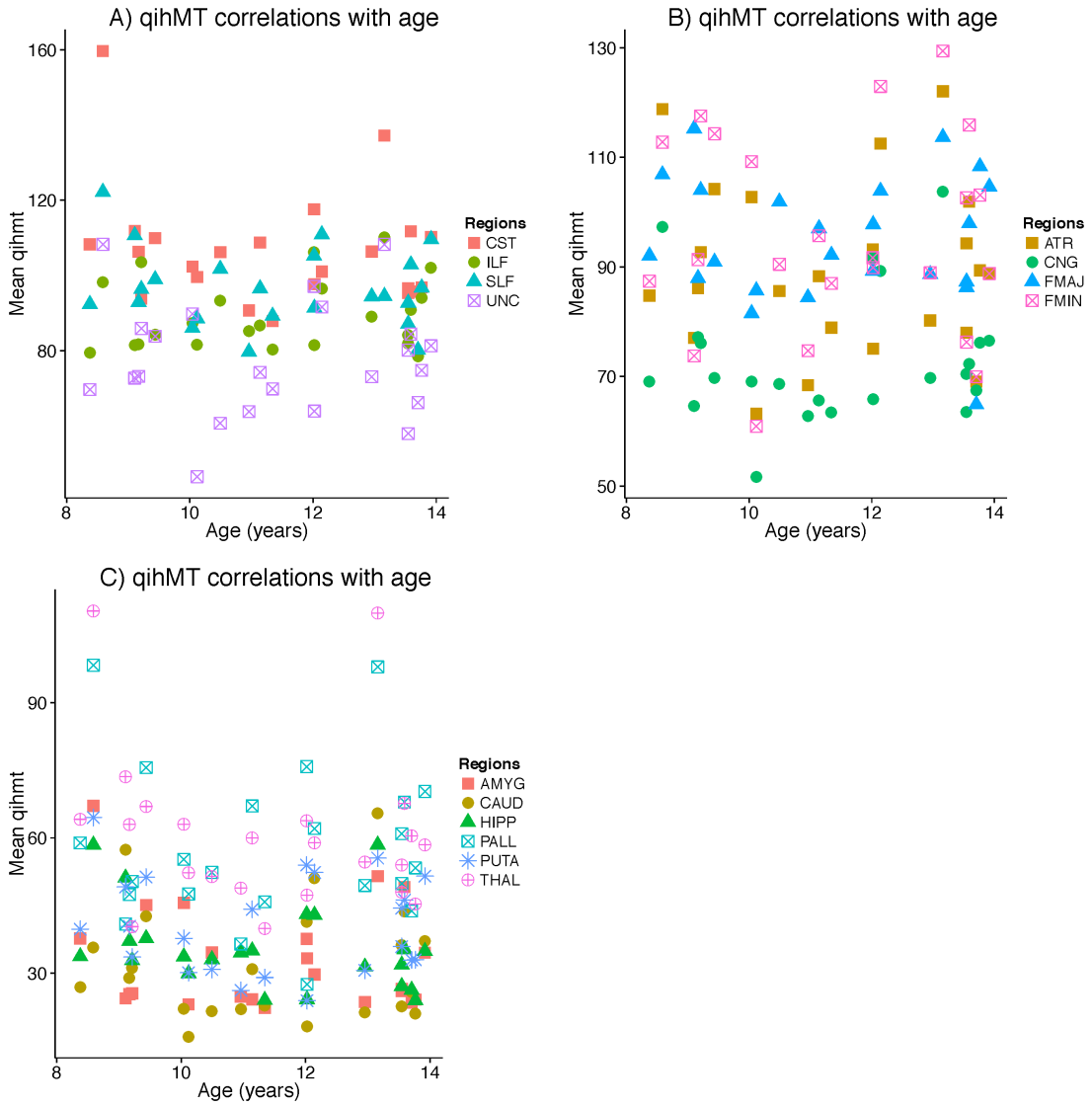

Figure 24. Mean qihMT trajectories in white (A, B) and grey (C) matter volumes-of-interest. No regressions were significant.

APPENDIX D: BROWN MRI ACQUISITION PARAMETERS

The MRI scan parameters for the Brown subjects were extracted from Appendix A of Deoni et al. (Deoni et al. 2012) under the Creative Commons Attribution License (CC BY).

Extract begins:

3 to 9 months of age

14 cm × 14 cm × 13 cm Sagittal Field of View (FOV) with an 80 × 80 × 72 acquisition matrix.

SPGR: echo time (TE)/repetition time (TR) = 5.8 ms/12 ms; flip angles = {2, 3, 4, 5, 7, 9, 11, 14} degrees; receiver bandwidth (BW) = 350 Hz/voxel; 6/8 partial k-space in the phase and slice-encode directions.

IR-SPGR: matched to SPGR with inversion times of 600 ms and 950 ms; half the resolution in the slice direction. 6/8 partial k-space acquisition in the phase-encode direction.

bSSFP: TE/TR = 5 ms/10 ms; flip angles = {9, 14, 20, 27, 34, 41, 56, 70} degrees; receiver bandwidth (BW) = 350 Hz/voxel; 6/8 partial k-space in the phase and slice–encode directions. Two sets of bSSFP data are acquired with phase-cycling increments of 0 and 180°.

Total acquisition time = 18:22.

Unprotected dB at front of scanner bore: 54 dB.

9 to 16 months of age

17 cm × 17 cm × 14.4 cm Sagittal Field of View (FOV) with an 96 × 96 × 80 acquisition matrix.

SPGR: TE/TR = 5.9 ms/12 ms; flip angles = {2, 3, 4, 5, 7, 9, 11, 14} degrees;
BW = 350 Hz/voxel; 5/8 partial k-space in the phase and slice–encode directions.

IR-SPGR: matched to SPGR with inversion times of 600 ms and 900 ms; half the resolution in the slice direction. 6/8 partial k-space acquisition in the phase-encode direction.

bSSFP: TE/TR = 5.1 ms/10.2 ms; flip angles = {9, 14, 20, 27, 34, 41, 56, 70} degrees;
BW = 350 Hz/voxel; 5/8 partial k-space in the phase and slice-encode directions. Two sets of bSSFP data are acquired with phase-cycling increments of 0 and 180°.

Total acquisition time = 18:42.

Unprotected dB at front of scanner bore: 62 dB.

16 to 28 months of age

18 cm × 18 cm × 15 cm Sagittal Field of View (FOV) with an 100 × 100 × 88 acquisition matrix.

SPGR: TE/TR = 5.4 ms/12 ms; flip angles = {2, 3, 4, 5, 7, 9, 11, 14} degrees;
BW = 350 Hz/voxel; 5/8 partial k-space in the phase and slice-encode directions.

IR-SPGR: matched to SPGR with inversion times of 500 ms and 850 ms; half the resolution in the slice direction. 6/8 partial k-space acquisition in the phase-encode direction.

bSSFP: TE/TR = 5 ms/10 ms; flip angles = {9, 14, 20, 27, 34, 41, 56, 70} degrees;
BW = 350 Hz/voxel; 5/8 partial k-space in the phase and slice-encode directions. Two sets of bSSFP data are acquired with phase-cycling increments of 0 and 180°.

Total acquisition time = 21:38.

Unprotected dB at front of scanner bore: 69 dB.

28 to 48 months of age

20 cm × 20 cm × 15 cm Sagittal Field of View (FOV) with an 112 × 112 × 88 acquisition matrix.

SPGR: TE/TR = 5.2 ms/11 ms; flip angles = {2, 3, 4, 5, 7, 9, 12, 16} degrees;
BW = 350 Hz/voxel; 5/8 partial k-space in the phase and slice-encode directions.

IR-SPGR: matched to SPGR with inversion times of 500 ms and 800 ms; half the resolution in the slice direction. 6/8 partial k-space acquisition in the phase-encode direction.

bSSFP: TE/TR = 4.4 ms/9.8 ms; flip angles = {9, 14, 20, 27, 34, 41, 56, 70} degrees;
BW = 350 Hz voxel; 5/8 partial k-space in the phase and slice-encode directions. Two sets of bSSFP data are acquired with phase-cycling increments of 0 and 180°.

Total acquisition time = 24:20.

Unprotected dB at front of scanner bore: 74 dB.

48 + months of age

20 cm × 20 cm × 16.5 cm Sagittal Field of View (FOV) with an 112 × 112 × 92 acquisition matrix.

SPGR: TE/TR = 4.8 ms/10 ms; flip angles = {3, 4, 5, 6, 7, 9, 13, 18} degrees;
BW = 350 Hz/voxel; 6/8 partial k-space in the phase and slice-encode directions.

IR-SPGR: matched to SPGR with inversion times of 450 ms and 750 ms; half the resolution in the slice direction. 6/8 partial k-space acquisition in the phase-encode direction.

bSSFP: TE/TR = 5 ms/10 ms; flip angles = {9, 14, 20, 27, 34, 41, 56, 70} degrees; receiver bandwidth (BW) = 350 Hz/voxel; 6/8 partial k-space in the phase and slice-encode directions. Two sets of bSSFP data are acquired with phase-cycling increments of 0 and 180°.

Total acquisition time = 22:45.

Unprotected dB at front of scanner bore: 82 dB.

Extract ends.